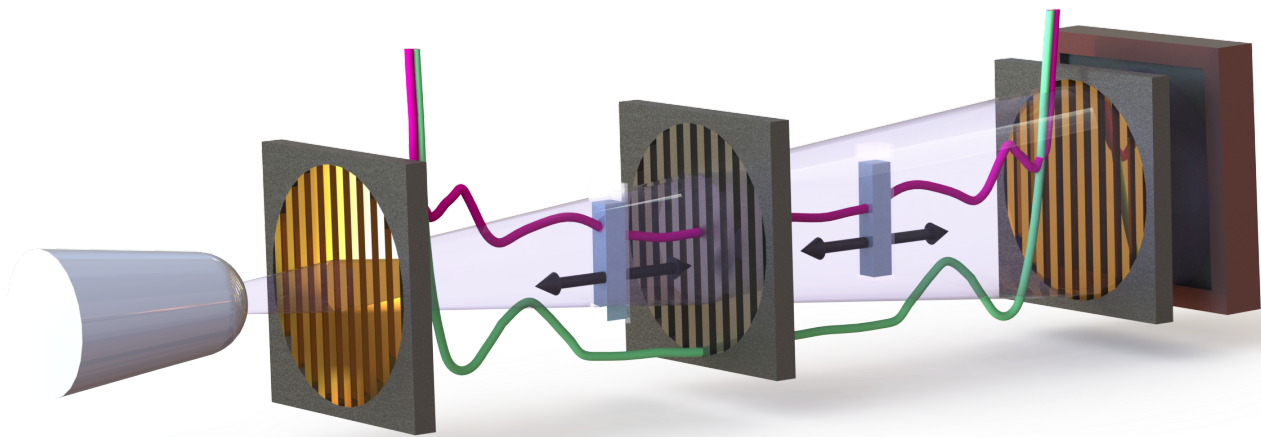


Grating-based X-ray Dark-Field Imaging:



Theory and Applications in Materials Research

Friedrich Prade

Dissertation

Supervisor: Prof. Dr. Franz Pfeiffer

TECHNISCHE UNIVERSITÄT MÜNCHEN
Physik Department
Lehrstuhl für Biomedizinische Physik

Grating-based X-ray Dark-Field Imaging: Theory and Applications in Materials Research

Friedrich Prade

Vollständiger Abdruck der von der Fakultät für Physik der Technischen Universität München zur Erlangung des akademischen Grades eines

Doktors der Naturwissenschaften (Dr. rer. nat.)

genehmigten Dissertation.

Vorsitzender: Prof. Dr. Michael Knap

Prüfer der Dissertation: 1. Prof. Dr. Franz Pfeiffer

2. Prof. Dr. Axel Haase

Die Dissertation wurde am 03.01.2017 bei der Technischen Universität München eingereicht und durch die Fakultät für Physik am 03.03.2017 angenommen.

Abstract

Attenuation-based X-ray imaging is often applied in biomedical, medical and materials research, as well as in non-destructive testing because it reveals information on the sample's internal structure. In recent years, grating-based X-ray imaging has developed into a method which can further increase the benefit of X-ray imaging in those research fields. It utilizes wave properties of X-rays in order to obtain two additional contrast modes. X-ray refraction is the origin of the differential phase contrast, while scattered X-rays generate the so-called dark-field contrast. Especially the dark-field signal is of great interest to researchers because it provides quantitative information on microscopic features without the necessity to spatially resolve those features.

In the first part of this thesis, a theoretical model is developed which relates the dark-field signal to a real-space correlation function representing the sample's microstructure. General basics of small-angle scattering are elaborated and the resulting implications for grating-based X-ray imaging are explained. Based on this theoretical framework, an experimental approach is developed allowing to measure correlation functions. According to this approach, diluted and dense solutions of monodisperse microspheres are studied and respective models are fitted to the experimental data. Conclusions on the sphere's diameters and particle short-range ordering within dense sphere solutions are drawn based on the experimental data confirming the theoretical predictions. The presented results emphasize that quantitative information on the form- and structure factor of microstructural features ranging from the nano- to micrometer scale can be obtained by dark-field measurements using laboratory X-ray equipment.

In the second part of this thesis, potential applications of dark-field imaging in materials research and non-destructive testing are presented. Microstructural developments caused by the hydration of cement-based materials are studied. Furthermore, water transport processes in temperature treated mortar and biofilm-hybrid mortar samples are investigated based on the dark-field signal. Showing the full potential of X-ray dark-field imaging, a method for time-resolved dark-field computed tomography is developed and a sample combining both effects, i.e. hydration and water transport, is studied. The time-evolution of both processes is spatially resolved as shown by our measurements. Finally, grating-based X-ray dark-field imaging is applied in order to study fiber orientation in fiber reinforced materials. Here, the grating's unidirectional sensitivity for scattered X-rays is exploited. The fiber orientation in various samples is analyzed with X-ray vector radiography, which is an extension to grating-based dark-field imaging. The extracted fiber orientation is in good agreement with micro-tomography data emphasizing the advantages of grating-based dark-field imaging when compared to conventional X-ray imaging.

Zusammenfassung

In vielen Forschungsfeldern wie der biomedizinischen und medizinischen Forschung, den Materialwissenschaften und der zerstörungsfreien Prüfung wird konventionelle Röntgenbildgebung genutzt, um die innere Struktur von Probekörpern zu untersuchen. Die gitterbasierte Röntgenbildgebung ist eine Weiterentwicklung, welche den Nutzen der Röntgenbildgebung für die Forschung weiter verbessern kann. Basierend auf den Welleneigenschaften von Röntgenstrahlen, liefert diese Technik zusätzliche Informationen. Eine Brechung der Röntgenstrahlen durch das Objekt liefert differenzielle Phasenkontrastbilder, wohingegen gestreute Röntgenstrahlen den sogenannten Dunkelfeldkontrast erzeugen. Das Dunkelfeldsignal enthält quantifizierbare Informationen über die Mikrostruktur des untersuchten Objektes und ist damit von besonderem Interesse für die Forschung.

Im ersten Teil dieser Arbeit wird ein theoretisches Modell entwickelt, welches das Dunkelfeldsignal in Beziehung zu Korrelationsfunktionen setzt, welche die Mikrostruktur des Objektes beschreiben. Zunächst werden die allgemeinen Grundlagen der Kleinwinkelstreuung wiederholt, um daraus die physikalische Entstehung des Dunkelfeldsignals zu entwickeln. Zur Überprüfung dieser theoretischen Überlegungen wird zudem eine experimentelle Methode zum Messen von Korrelationsfunktionen entwickelt und getestet. Verdünnte und hochkonzentrierte Dispersionen von sphärischen Mikropartikeln werden untersucht und mit Hilfe entsprechender Modelle ausgewertet. Aus den Messdaten können die Durchmesser der Mikropartikel bestimmt sowie eine Nahordnung der Mikropartikel in den hochkonzentrierten Dispersionen beobachtet werden. Das Dunkelfeldsignal erlaubt es folglich zwei wichtige Mikrostrukturparameter aus der Kleinwinkelstreuung, den Form- und Strukturfaktor, zu bestimmen.

Im zweiten Teil der Arbeit werden potentielle Anwendungen der Dunkelfeldbildgebung in den Materialwissenschaften und der zerstörungsfreien Prüfung behandelt. Mikrostrukturelle Veränderungen während des Aushärtens zementbasierter Materialien sowie Wassertransportprozesse in temperaturbehandeltem Mörtel und Biofilm-Hybrid-Mörtel werden untersucht. Des Weiteren wird eine Methode zur zeitaufgelösten Dunkelfeldtomographie entwickelt, um mit dieser Aushärtungs und Wassertransportprozesse in einer Zementprobe zu untersuchen. Der zeitliche Verlauf beider Prozesse kann mit Hilfe der entwickelten Methode räumlich aufgelöst dargestellt werden. Eine weitere potentielle Anwendung findet die Dunkelfeldbildgebung in der Untersuchung der Faserorientierungen in faserverstärkten Materialien. Mit Hilfe der Röntgenvektorradiographie, einer Erweiterung der gitterbasierten Bildgebung, wird die Faserorientierung in verschiedenen Probekörpern untersucht. Die gewonnenen Ergebnisse stimmen qualitativ mit Mikrotomografiedaten überein und verdeutlichen somit die Vorteile der gitterbasierten gegenüber der konventionellen Röntgenbildgebung.

Contents

1. Introduction, motivation and outline	1
1.1. Introduction	1
1.2. Motivation for this work	5
1.3. Outline	6
2. Theory	9
2.1. X-ray physics	9
2.2. Grating-based X-ray imaging	18
3. Details about the experimental system	31
3.1. X-ray tube and detector	31
3.2. X-ray gratings and the Talbot-Lau interferometer	34
3.3. Optimization of the system	35
4. Quantitative X-ray dark-field imaging	37
4.1. Small-angle X-ray scattering	38
4.2. Implications of SAXS theory for the dark-field signal	46
4.3. Experimental validation	52
4.4. Summary and discussion	62
5. Application of X-ray dark-field imaging in cement and concrete research	65
5.1. Introduction to cement-based building materials	66
5.2. Measurements on water transport in porous materials with dark-field imaging	68
5.3. Time evolution of the dark-field signal of fresh cement paste	74
5.4. Influence of temperature on the dark-field signal of fresh cement paste . . .	82
5.5. Influence of limestone grains on the dark-field signal of fresh cement paste .	85
5.6. Time-resolved dark-field tomography on fresh cement paste containing li- mestone grains	90
5.7. Summary and discussion	100
6. Fiber orientation characterization in fiber reinforced materials with X-ray dark-field imaging	101
6.1. Introduction to fiber reinforced materials	101
6.2. Measurements on short fiber reinforced polymer components with X-ray vector radiography	103

6.3. Summary and discussion	114
7. Summary and outlook	117
7.1. Summary	117
7.2. Outlook	118
A. Detailed derivation of equations from chapter 4	120
A.1. Calculations for equation 4.24	120
A.2. Impact of a polychromatic X-ray spectrum on equation 4.27	122
B. Additional figures for chapters 4 and 5	124
List of Tables	127
List of Figures	128
Abbreviations	130
Bibliography	132
Publications and conference contributions	142
Acknowledgments	144

1. Introduction, motivation and outline

In this chapter a motivation for the presented work is given followed by a brief structural outline of the content of this thesis.

1.1. Introduction

X-ray imaging and scattering

Investigating an object's internal structure non-destructively is of utmost interest in materials and biomedical research as well as in medical research, diagnostics and non-destructive testing (NDT). X-rays are therefore often applied as a research method in these fields due to their capability to penetrate matter without being fully extinguished. This characteristic of X-rays was first observed by W. C. Röntgen in 1895 while experimenting with accelerated electrons [1]. Not only did Röntgen observe X-rays for the first time, he also acquired the very first X-ray image by illuminating a human hand with X-rays and capturing the attenuated beam with a photographic plate. From there on, two-dimensional X-ray imaging, also known as radiography, developed into a valuable tool for medical doctors and scientists in many other research disciplines. X-ray radiography images show an overlay, i.e. a projection, of all the object's internal features which is disadvantageous when studying complex structures. While A. M. Cormack developed a theoretical method to overcome this problem, computed tomography (CT) was experimentally realized by G. N. Hounsfield in 1969 [2, 3]. In contrast to X-ray radiography, it provides three dimensional information about the sample's internal structure. It is based on X-ray radiography images acquired from many different projection angles. Today, medical CT devices provide X-ray images with a resolution of several hundreds of micrometers in terms of the image's pixel size. While micro-tomography (μ CT) systems reduce the image's pixel size down to a few micrometers [4–6], nano-tomography currently provides the smallest pixel size for laboratory-based X-ray imaging devices reaching down to a few hundred nanometers [7]. However, high resolution imaging requires a small object size in most cases and therefore its usage in some research areas is limited. With the emergence of large-scale synchrotron facilities, spatial resolution of X-ray images was further improved. Several methods have been developed in order to reach a pixel size of tenths of nanometers making use of sophisticated X-ray optics in X-ray microscopy or

1. INTRODUCTION, MOTIVATION AND OUTLINE

X-ray diffraction in coherent diffraction imaging techniques [8, 9]. Some of these methods do not rely on X-ray attenuation in order to generate image contrast between different materials. They rather rely on the wave nature of X-rays which also exhibit a phase shift when propagating through matter.

While Röntgen had initially failed to detect wave characteristics for X-rays, such as refraction, P. Knipping and M. Laue experimentally confirmed that X-rays indeed behave like electromagnetic waves [10]. They illuminated a copper(II) sulfate crystal with X-rays and concluded that the observed interference pattern originates from X-rays scattered by the electrons of the crystal. Furthermore, they obtained insight into the atomic structure based on this interference pattern. Nowadays, X-ray scattering is readily applied in order to study the atomic or molecular structure of a sample on the Ångström (10^{-10} m) length scale [11]. Other scattering-based methods, such as small-angle and ultra-small-angle X-ray scattering (SAXS and USAXS), provide structural information on a length scale reaching from several nanometers up to several hundreds of nanometers. They are often applied to obtain structural information on macromolecules or ordered systems [12].

However, high resolution imaging and scattering methods are limited regarding the sample's geometrical dimensions. Measuring large objects, with a size of several centimeters, usually leads to impractical long measurement times for high resolution imaging and scattering methods. If the object's size does not allow high resolution or scattering measurements due to experimental limitations, the object is usually broken up in several smaller pieces. This of course contradicts the use of X-rays as a non-destructive tool and strongly limits their range of application. A method that provides information about microstructural features within large objects (several centimeters) is therefore very appealing. This is schematically emphasized in figure 1.1. Here, the accessible length scale, at which structural information is obtained, is compared to the sample's suitable geometrical dimensions for several X-ray imaging and scattering methods.

Grating-based X-ray imaging

In this context, grating-based X-ray imaging is a promising method as it combines scattering information with a large field of view and because it is easily realizable with laboratory X-ray equipment as well. Grating-based X-ray imaging was primarily developed alongside other techniques in order to utilize the phase shift of X-rays, which they exhibit when propagating through matter, as an additional image contrast besides the standard attenuation contrast. The usage of some X-ray phase contrast imaging techniques is, however, restricted to synchrotron sources due to their requirements for beam coherence or a high X-ray flux. This is the case for crystal interferometry and analyzer-based imaging which both utilize crystals as beam optics in order to extract the phase information [13–16]. Propagation-based imaging, in contrast, is applicable with laboratory X-ray sources, however, with the limitation to a small field of view due to its requirement for high image

resolution [17]. This method relies on the free space propagation of X-rays and is experimentally easy to realize as it requires no additional optics. Grating-based X-ray imaging is also applicable with laboratory X-ray equipment. It was initially developed at synchrotron X-ray sources because it is based on X-ray interference and therefore requires a partially coherent X-ray beam [18–20]. Microstructured gratings are used in grating-based imaging to produce a distinct interference pattern. According to the Talbot-effect, a wavefront which illuminates a periodic structure, such as a grating, periodically repeats itself at certain distances behind the grating. This effect was first studied by H. F. Talbot in 1836 with visible light and later observed for X-rays [21, 22].

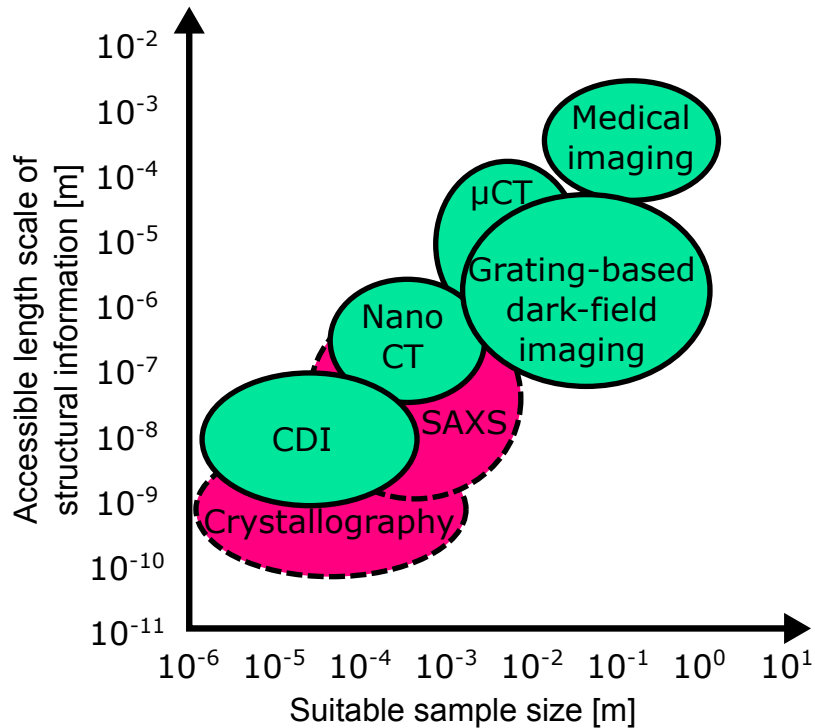


Figure 1.1.: This figure illustrates the accessible length scale of structural information in comparison to the sample’s suitable size for several X-ray techniques. The y-axis indicates the accessible length scale at which structural information is obtained for different X-ray techniques. The x-axis indicates the suitable sample size which can be scanned with each technique. Imaging techniques are colored in green while scattering techniques are shown by pink ellipses with dashed contours. In the case of X-ray imaging, the suitable sample size for each technique decreases with increasing spatial resolution. Grating-based dark-field imaging allows to study microstructural features in large objects as it combines the accessible length scale of structural information of μ CT and nano-tomography with a large field of view comparable to medical imaging.

Conventional X-ray detectors cannot resolve the interference pattern because their pixel

1. INTRODUCTION, MOTIVATION AND OUTLINE

size is usually too large. Therefore, a second grating, which acts as an absorber grating and is called analyzer grating, is placed right in front of the detector. The addition of another absorption grating in front of the X-ray source nowadays enable grating-based X-ray imaging with laboratory X-ray sources [23]. This three grating configuration resembles a Talbot-Lau interferometer.

When a sample is placed behind or in front of the phase grating, X-ray get refracted and the interference pattern is distorted accordingly. These distortions are translated into differential phase contrast (DPC) images. Further studies revealed that a third contrast channel is accessible in addition to the DPC and the attenuation contrast. It was shown that the visibility of the interference pattern provides information about the small-angle X-ray scattering (SAXS) properties of the sample [24]. Images created based on this scattering signal are often referred to as dark-field images due to similarities to visible light dark-field microscopy. It was shown in several studies that quantitative structural parameters can be extracted from on the scattering-based dark-field contrast with grating-based X-ray imaging [25–27]. Because scattering data carries quantitative structural information on a length scale of several hundreds of nanometers up to several micrometers dark-field imaging also provides access to this length scale.

Another grating-based X-ray imaging technique has been recently developed making use of three phase gratings and the phase Moiré effect [28]. Polychromatic far-field interferometry, as it is called, proved to be more sensitive to phase variations when compared to Talbot-Lau interferometry [29]. However, due to stringent grating requirements the technique currently remains limited to a small field of view and low X-ray energies up to 30 keV [29]. Talbot-Lau interferometers, in contrast, have been shown to work at up to 120 keV with a large field of view [30].

The potential of grating-based X-ray imaging to combine structural information on the micrometer length scale with a large field of view has been exploited in several studies. Microstructural changes in diseased lungs of living mice were successfully diagnosed by grating-based X-ray dark-field imaging [31]. Furthermore, the microstructure of bones was studied based on this method [32]. But besides biomedical research and medical diagnostics, X-ray dark-field imaging also carries potential for applications in materials research and NDT. For example, cementitious materials and fiber reinforced materials were recently studied by grating-based X-ray imaging [33–35].

X-ray imaging in materials research

Attenuation based X-ray imaging is commonly applied in materials research and NDT for material's characterization and the detection of defects and flaws [36]. Fiber orientation and fiber content in fiber reinforced composite materials are usually evaluated by μ CT [37, 38]. Here, the fiber diameter is about 5 – 10 μ m for carbon fibers and 10 – 20 μ m for

glass fibers. In order to resolve such fibers with μ CT systems, samples have to be smaller than 1 cm in size. More complex materials, such as cement are studied at synchrotron sources with high resolution X-ray microscopy to obtain structural and chemical information on the nanometer length scale [39, 40]. However, in both cases microstructural information is obtained for small sample volumes only. Therefore, the assessment of microstructural information in objects of practically relevant size remains challenging with both laboratory and synchrotron-based X-ray imaging methods.

Grating-based X-ray imaging is therefore a promising tool for materials research and NDT because it bridges the gap between suitable object size and small feature detectability. It has therefore drawn some attention in materials research and NDT in recent years. For example, water transport processes in porous materials such as mortar were successfully studied based on dark-field radiography [33]. Compared to attenuation-based imaging methods, the dark-field signal provides stronger contrast for water-saturated pores while it does not require to spatially resolve single pores. Further studies revealed micro cracks in mineral aggregates and other materials by utilizing the improved contrast of the dark-field signal for unresolvable microstructures [34, 41].

Besides the basic image contrast generated by unresolvable scattering structures in dark-field images, X-ray dark-field imaging further provides information on the orientation of microstructural features. A Talbot-Lau interferometer is most sensitive to X-rays which are scattered perpendicular to the grating lamellae. This characteristic enables the assessment of orientation information. Studies on fiber orientation characterization in fiber reinforced materials were successfully conducted based on this property [35, 42].

In addition to the qualitative use of the dark-field signal as a basic contrast channel in X-ray imaging, quantitative dark-field imaging is also possible. Theoretical approaches towards quantitative dark-field imaging were developed [25–27] and experimentally verified in synchrotron experiments [25, 26]. Here, the diameter of spherical microparticles was determined based on the dark-field signal.

1.2. Motivation for this work

The outlined application examples and the possibility to extract quantitative structural information from the dark-field signal suggest the potential of grating-based X-ray imaging for materials research and NDT. To further emphasize this, the presented work elaborates on the theoretical basics of the dark-field signal and its relation to SAXS. An experimental approach is derived from the theoretical considerations which enables quantitative measurements not only with synchrotron sources but also with conventional X-ray tubes. Based on this approach, an experimental verification of the theoretical findings is provided.

1. INTRODUCTION, MOTIVATION AND OUTLINE

In addition, experimental applications for grating-based X-ray dark-field in materials research and NDT are presented and discussed. Time-resolved dark-field radiography and tomography methods are developed and applied in order to study the setting and hardening as well as water transport processes in cement-based materials. Furthermore, fiber orientation in short fiber reinforced polymers is studied and qualitatively compared to μ CT measurements.

The purpose of this work is to emphasize the potential of grating-based X-ray imaging for materials research and NDT, to develop experimental methods for possible applications and to outline its advantages when compared to conventional X-ray imaging. The central messages of this work are summarized as follows:

- Originating from X-ray scattering, the dark-field signal is sensitive to microstructural features which are too small to be directly spatially resolved by the imaging system
- The dark-field signal provides quantitative microstructural parameters
- It allows to investigate objects of several centimeters in size
- The temporal evolution of slow microstructural processes can be studied in two- as well as three dimensions
- Dark-field based fiber orientation characterization is feasible and faster compared to μ CT measurements

1.3. Outline

In the following, a brief outline of this thesis is given.

Chapter 2

Here, we describe the fundamentals of X-ray physics and imaging, which are necessary for further understanding. Furthermore, the basic working principle of an X-ray Talbot-Lau interferometer and its usage for imaging are explained. We illustrate how images are extracted and explain the relevant data processing algorithms.

Chapter 3

In this chapter, the experimental setup, which was developed and used for most of the experiments presented in this work, is described. Important parameters on the interferometer, X-ray source and detector are stated. A brief section covering the optimization of this setup is also provided in this chapter.

Chapter 4

Starting with the principles of SAXS, we develop a theoretical approach for quantitative grating-based dark-field imaging in this chapter. An experimental approach for quantitative measurements is derived based on the theoretical consideration. Experimental results are presented in order to validate the theoretical findings.

Chapter 5

As the first application example of grating-based X-ray dark-field imaging, studies on water transport processes in porous materials are studied. Further on, hydration reactions during setting and hardening of cement paste are investigated by time-resolved dark-field radiography. The impact of mineral aggregates on the observed effects is studied as a next step. The chapter is concluded by a time-resolved X-ray dark-field tomography study on a fresh cement sample.

Chapter 6

A study on fiber orientation in short fiber reinforced polymers (SFRPs) based on X-ray vector radiography (XVR), an extension to grating-based X-ray dark-field imaging, is presented in this chapter. Various sample geometries, sizes and different fiber materials are studied and qualitatively compared to μ CT results.

Chapter 7

Finally, the theoretical and experimental results presented in this work are summarized before the work is concluded with an outlook on future applications and advances in grating-based X-ray dark-field imaging.

2. Theory

In this chapter, we outline theoretical fundamentals of X-ray physics and X-ray imaging that are important for further understanding. Furthermore, we elaborate on the basic working principle of an X-ray Talbot-Lau interferometer and its use for imaging. Three different contrast channels, i.e. the attenuation, differential phase and dark-field contrast are introduced. More theoretical details are presented in the books "*Elements of Modern X-ray Physics*" by J. Als-Nielsen and D. McMorrow and "*An Introduction to Synchrotron Radiation*" by P. Wilmott as well as the PhD Thesis of M. Bech [43–45].

2.1. X-ray physics

X-rays were already presumed to be electromagnetic waves when they were first discovered by W. C. Röntgen. However, first evidence was obtained not until M. Laue observed X-ray diffraction by a crystal. From there on, the classical description of X-rays as electromagnetic waves was established. Besides the wave nature of X-rays, the work of A. Compton suggested that X-rays can also be treated by a quantum mechanical particle model [46]. In this picture the radiation field of X-rays is quantized into photons which travel at the speed of light and serve as the carriers of electromagnetic force. For now we elaborate further on the classical description of X-rays as electromagnetic waves.

The energy spectrum of X-rays stretches from the soft X-ray regime with several kiloelectron volt (keV) up to the hard X-ray regime with some megaelectron Volt (MeV). This translates to wavelengths ranging from 0.01 Å (10^{-10} m) for high energies up to 10 nanometers for low energies. The simplest case of an electromagnetic wave is a monochromatic plane wave. For reasons of simplicity we restrict further considerations to this scenario for the remainder of this chapter. Furthermore, we only consider the electric field component due to its analogy to the magnetic field component. The amplitude Ψ of a monochromatic plane wave at position z and time t , which has a wavelength λ and travels in vacuum in z -direction, is described by the following equation:

$$\Psi(z, t) = \Psi_0 e^{i(kz - \omega t)} \quad . \quad (2.1)$$

Here, Ψ_0 corresponds to the wave's maximal amplitude, $k = 2\pi/\lambda$ represents the wavevector in z -direction and $\omega = 2\pi c/\lambda$ is the angular velocity with the speed of light c . The exponential term in equation 2.1 is also referred to as the phase of the wave. X-rays

2. THEORY

are transverse waves, meaning that the electric field vector is always perpendicular to the propagation direction indicated by the wavevector k . If this electric field vector is oriented along the same axis at each point in time, we speak of linearly polarized X-rays. In contrast to that, the electric field vector rotates around the wavevector k in the case of circular polarization.

2.1.1. Coherence and X-ray sources

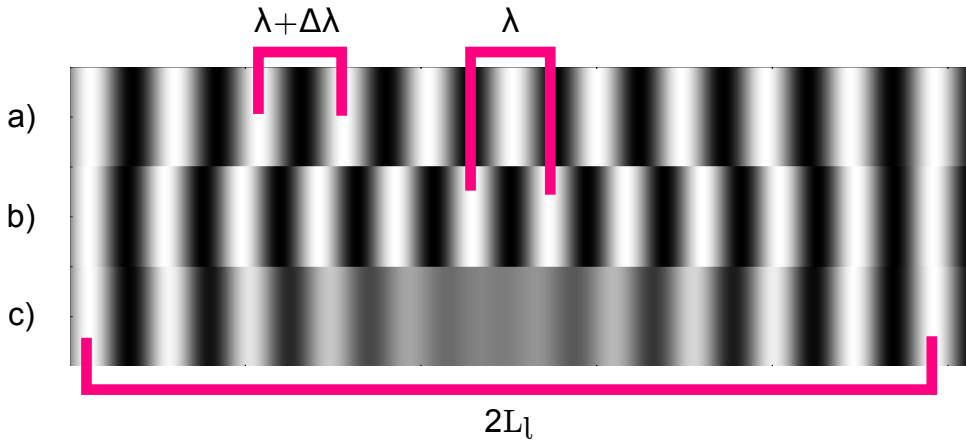


Figure 2.1.: This figure shows a schematic representation of the longitudinal coherence length L_l . Two plane waves with wavelengths $\lambda + \Delta\lambda$ (a) and λ (b) propagate along the same direction. Their superposition (c) shows that the phase relation between the two waves is lost, before it is recovered after twice the longitudinal coherence length L_l . This figure was adapted from reference [44].

Like any electromagnetic wave, X-rays show interference under certain conditions. The ability of waves to interfere is described by the term coherence. In a simple scenario, coherence describes the phase relation of two plane waves which either propagate in the same direction but have different wavelengths, or which propagate in different directions but have the same wavelength. The first case is termed temporal or longitudinal coherence, while the second case is referred to as spatial or transverse coherence. A monochromatic plane wave, therefore, is perfectly coherent in space and time. When two plane waves of different wavelength λ and $\lambda + \Delta\lambda$, which are initially in phase, propagate in the same direction their phase term relation changes. This behavior is described by the longitudinal coherence length L_l and such a scenario is illustrated in figure 2.1. It is defined as the longitudinal distance, i.e. distance along the propagation direction, where the two wave's phase terms differ by π . It is calculated by following equation [43, 44]:

$$L_l = \frac{\lambda^2}{2\Delta\lambda} \quad . \quad (2.2)$$

Here, the wavelength of one wave is given by λ , while $\Delta\lambda$ represents the wavelength difference of the two waves.

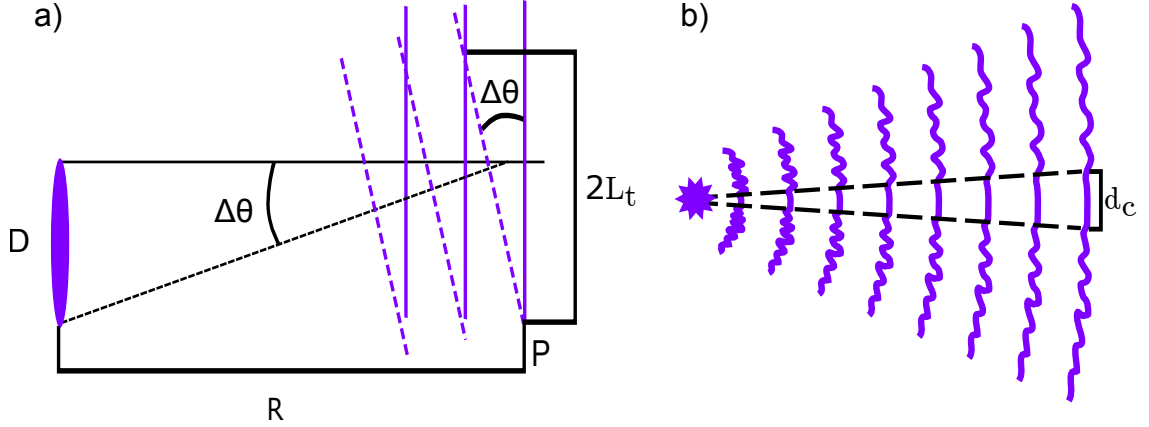


Figure 2.2.: This figure shows a schematic representation of the transverse coherence length L_t . **a)** A geometric illustration of the transverse coherence length L_t is shown. Each point of a source of size D emits X-rays propagating in different directions. The two wavefronts (solid and dashed purple lines) are in phase at point P , while they are out of phase when moving perpendicular to the propagation direction. After a distance of $2L_t$ they are in phase again. **b)** An intuitive illustration of the transverse coherence length is shown. A source emits a divergent and rough wavefront. This roughness indicates the weak phase term correlation perpendicular to the propagation direction of the wavefront. As the wave propagates in space, its roughness smooths out and the transverse distance d_c with strong phase correlation increases [47, 48]. This is illustrated by the black dashed lines. Image a) was adapted from reference [43] and image b) from reference [47].

The transverse coherence length for two waves propagating in different directions is also defined by the phase term difference of π . This scenario is illustrated on the left side of figure 2.2. Two waves coming from different spots of an extended source propagate in different directions and are in phase at point P at a distance R from the source of size D . The transverse coherence length L_t is defined by the distance perpendicular to the propagation direction for which the wave's phase terms differ by π . It is calculated as follows [43, 44]:

$$L_t = \frac{\lambda R}{2D} \quad . \quad (2.3)$$

These considerations illustrate, that X-ray beams with broad energy spectrum and a large source spot size suffer from low coherence. This is generally the case for conventional X-ray tubes. Therefore, interference effects are usually not observed when working with such tubes.

2. THEORY

In conventional X-ray tubes, electrons hit the anode at energies of several keV and are decelerated due to the interaction with the target material. Due to the deceleration, they emit X-rays in all directions with energies as high as the initial acceleration energy of the electrons. The resulting spectrum is referred to as the Bremsstrahlungsspektrum. The use of rotating or liquid anode materials represent further technical realizations of this principle [49].

In contrast to that, large-scale synchrotron facilities utilize the interaction of accelerated electrons with magnetic fields in order to generate X-rays. Here, electrons emit X-rays while changing their direction in bending magnets or being periodically stimulated in a so-called undulator [44]. As a result of the relativistic electron energies, synchrotron radiation is more intense, has a narrower energy spectrum and is less divergent when compared to conventional X-ray tubes. Summarizing all these characteristics, synchrotron radiation has a higher brilliance compared to X-rays generated by conventional tubes. Therefore, synchrotron radiation is also superior to conventional X-ray tubes in terms of beam coherence. However, the transverse coherence length of an extended and divergent source increases with propagation distance as shown by equation 2.3. This intuitive explanation is illustrated in more detail figure 2.2 b). Under certain conditions, interference effects are therefore also observed with conventional X-ray tubes as coherence is generated just by means of propagation [47, 48].

2.1.2. Interaction of X-rays with matter

Because X-rays serve as the carrier of electromagnetic force, they interact with electrons when propagating through matter. In the following we concentrate on the three major types of interactions.

Elastic X-ray scattering

First, we consider elastic or coherent scattering of X-rays by a free electron. Electrons in matter can usually be treated as free electrons, because X-ray energies are much higher than the binding energies of most atomic electrons. This is true at least for electrons outside the atomic K- or L-shell. During this scattering interaction, the X-ray energy does not change. Their direction of propagation, however, changes while the electron's state after the interaction remains unchanged. In terms of classical physics, electrons are forced into a harmonic oscillation by the electric field of the incoming X-ray. According to the Maxwell equations, an oscillating electron radiates an electromagnetic wave with the same frequency as the electron's oscillation, i.e. the same frequency as the incoming X-ray. Electrons are described as a driven harmonic oscillator in this classical picture. X-ray frequencies are much higher than the resonance frequencies of weakly bound electrons. This results in a phase difference of π between incoming and scattered X-rays. Figure 2.3 a) illustrates this process for a plane wave polarized in x-direction. The ratio of the

intensity scattered into a certain solid angle I_{sc} , and the incoming intensity I_0 is defined as the differential scattering cross-section $d\sigma/d\Omega$. In the case of elastic X-ray scattering by a free electron, this cross-section is referred to as the Thomson differential scattering cross-section and it is given by the following equation [43]:

$$\frac{d\sigma}{d\Omega} = r_{el}^2 P^2 = r_{el}^2 \frac{1}{2} (1 + \cos^2(2\theta)) \quad . \quad (2.4)$$

Here, r_{el} represents the Thomson scattering length or the classical electron radius, P is a factor which accounts for the polarization of the incoming radiation. The polarization term for unpolarized sources is given by $P^2 = 1/2(1 + \cos^2(2\theta))$. We restrict all following considerations to this case because conventional X-ray tubes generate unpolarized radiation. The angle 2θ refers to the angle under which the scattering process is observed as shown in figure 2.3 a).

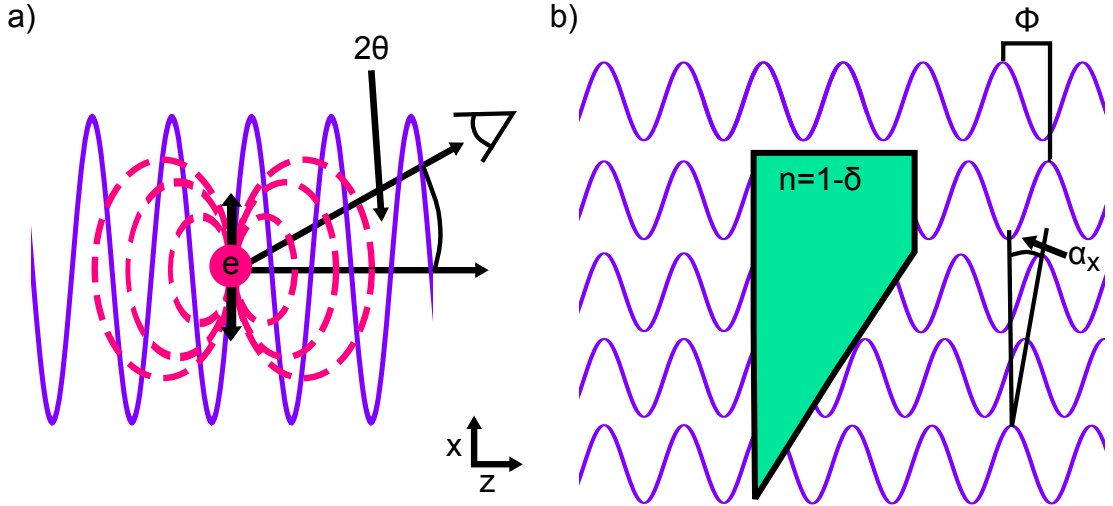


Figure 2.3.: This figure illustrates the processes of elastic X-ray scattering and X-ray refraction. **a)** An electron e harmonically oscillates along the x-axis (black arrows) in the electric field of an electromagnetic plane wave (purple wave), which is polarized in x-direction. The oscillating electron emits a scattered wave in the form of dipole radiation (pink dashed wavefront) with the same energy as the incoming wave. Scattered X-rays have a π -phase shift when compared to the incoming X-ray. The scattering process is observed under an angle 2θ . **b)** A wave propagates through a material with refractive index $n = 1 - \delta$. X-rays that have been elastically scattered by the electrons are superimposed to the incoming X-rays. The resulting wavefront is shifted in phase by Φ . Due to a gradient of this phase shift Φ the wavefront gets refracted by an angle α .

It is important to note that $d\sigma/d\Omega$ is independent of the X-ray energy which only holds true under the assumption of free electrons. This assumption is fulfilled as long as the X-ray energy does not match the energy of a bound atomic electron on the inner shells which

2. THEORY

otherwise results in a resonant excitation. However, we do not consider such scenarios in this work and restrict all considerations to elastic scattering by free electrons.

Refraction of X-rays

Refraction is a macroscopic result of elastic X-ray scattering in matter. The refracted wave is a superposition of the incoming wave and all scattered waves. Its phase term is shifted when compared to the incoming wave due to this superposition. Refraction is phenomenologically described by the refractive index $n = 1 - \delta$ of a material. In the X-ray regime, δ is of an order of $10^{-5} - 10^{-6}$ and the refractive index is slightly smaller than unity. For visible light n is typically larger than one. The fact that n is smaller than unity in the X-ray regime is related to the phase shift of π for elastic X-ray scattering. The refractive index describes the ratio of the X-ray's absolute wavevector in matter k_{mat} and the vacuum wavevector k . Therefore, equation 2.1 transforms into following equation for X-rays propagating through matter:

$$\Psi(z, t)_{mat.} = \Psi_0 e^{i(k_{mat}z - \omega t)} = \Psi_0 e^{i(nkz - \omega t)} \quad . \quad (2.5)$$

When we consider that each electron in the sample scatters the incoming wave according to equation 2.4, we obtain following relation between δ , the Thomson scattering length r_{el} and the X-ray wavelength λ [43]:

$$\delta = \frac{\lambda^2 \rho_{el} r_{el}}{2\pi} \quad . \quad (2.6)$$

This relation depends on the electron density ρ_{el} indicating that a macroscopic change in electron density results in X-ray refraction [44]. According to equation 2.5 and 2.6, X-rays passing through an object of varying thickness $\Delta z(x)$ exhibit a phase shift $\Phi(x)$ when compared to a wave traveling in vacuum [43]:

$$\Phi(x) = -\delta k \Delta z(x) \quad . \quad (2.7)$$

This gradual phase shift in x-direction results in a refraction of the wavefront as illustrated in figure 2.3 b). The angle of refraction α is related to the gradient of the phase shift $\Phi(x)$ by following equation [43]:

$$\alpha = \frac{1}{k} \frac{\partial \Phi(x)}{\partial x} \quad . \quad (2.8)$$

Inelastic X-ray scattering

Besides elastic X-ray scattering, X-rays and electrons also interact inelastically. This was first observed by A. Compton in 1922 and explained as a particle interaction between X-ray photons and electrons [46]. Inelastic scattering implies that the incoming photon transfers part of its energy to the scattering electron. The scattered photons therefore have

less energy as compared to the incoming photons. The energy loss of the X-ray photon is transformed into kinetic energy of the electron which therefore acquires momentum after scattering. This is illustrated in figure 2.4 a).

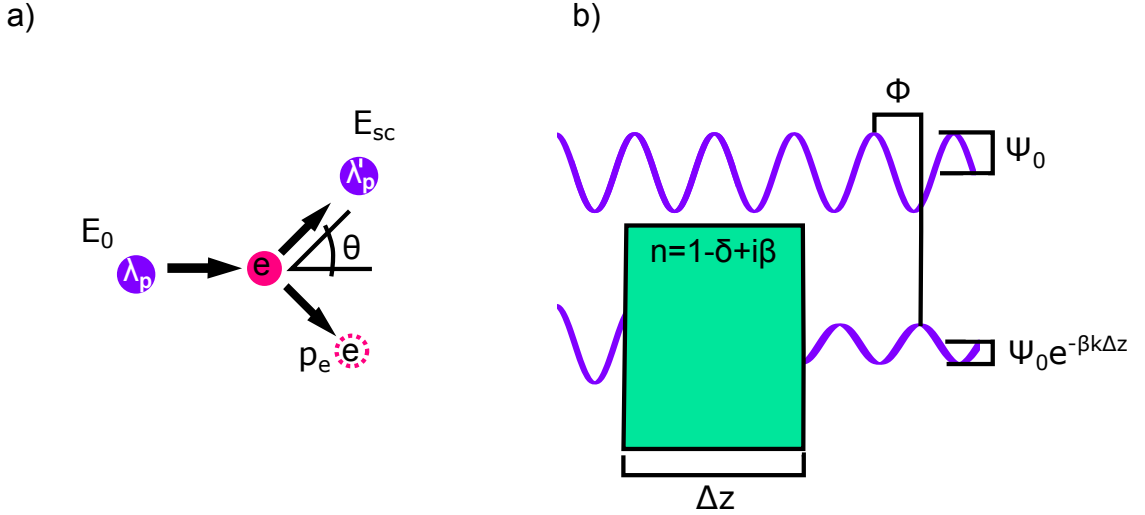


Figure 2.4.: This figure shows a schematic illustrations of Compton scattering and X-ray absorption. **a)** When an X-ray photon is inelastically scattered by an electron e , the energy of the photon decreases from E_0 to E_{sc} . Therefore, its wavelength λ_p increases to λ'_p while the propagation direction changes by an angle θ . The electron, initially at rest, has a momentum p_e after scattering. **b)** X-ray absorption is described by adding a complex term β to the refractive index n . Thus, the maximal amplitude Ψ_0 of the wave decreases by a factor $e^{-\beta k \Delta z}$ behind an object of thickness Δz .

The energy of the scattered photon E_{sc} is calculated based on conservation of energy and momentum. It is related to the scattering angle θ according to following equation [46]:

$$E_{sc} = \frac{E_0}{1 + \frac{E_0}{m_e c^2} (1 - \cos(\theta))} \quad . \quad (2.9)$$

Here, m_e is the mass of an electron at rest and E_0 represents the energy of the incoming photon before scattering. Due to this energy loss and the corresponding wavelength change, this process is referred to as inelastic or incoherent scattering. For $E_0 < m_e c^2 = 511$ keV, however, this energy loss becomes very small. Furthermore, the Compton scattering cross-section, which is stated by the Klein-Nishina formula, approaches the Thomson scattering cross-section for low X-ray energies and small scattering angles [50]. For the remainder of this work we consider X-ray energies well below the electron rest mass and small scattering angles. Therefore we neglect inelastic scattering and concentrate on elastic scattering only.

2. THEORY

X-ray absorption

Besides a partial energy transfer in Compton scattering, the full energy of an X-ray photon is transferred to an electron in the case of photoelectric absorption. Having absorbed the photon's energy, the excited electron is liberated from its atom and an electron hole is created on one of the inner shells. Photoelectric absorption therefore results in a loss of X-ray intensity. The Beer-Lambert Law describes this process when X-rays travel through an object of thickness Δz [43]:

$$I(\Delta z) = I_0 e^{-\mu_{abs}\Delta z} \quad . \quad (2.10)$$

Here, $I(\Delta z)$ is the intensity observed behind the object, I_0 is the incoming intensity and μ_{abs} is the material specific linear absorption coefficient. Absorption is also described by the refractive index when adding a complex term β to n in equation 2.5. This leads to the following representation of the wave:

$$\Psi(z, t)_{mat} = \Psi_0 e^{i(nkz - \omega t)} = \Psi_0 e^{i(1-\delta)kz} e^{-\beta kz} \quad . \quad (2.11)$$

Thus, the wave's amplitude behind an object of thickness Δz is decreased by $e^{-\beta k \Delta z}$ (see image b) in figure 2.4) [43]. Taking into account that the intensity is proportional to the squared wave amplitude, we obtain following relation between β and μ_{abs} :

$$\beta = \frac{\mu_{abs}\lambda}{4\pi} \quad . \quad (2.12)$$

2.1.3. X-ray imaging

Due to their high energy, X-rays are not fully extinguished when propagating through an object and a significant fraction of X-rays penetrates the object. X-ray absorption therefore serves as the basis for conventional X-ray imaging. Here, transmitted X-rays are detected behind the sample. Current technology only allows to measure the beam's intensity, while information on the phase term is lost. The detection of X-rays in conventional imaging typically relies on two principles, i.e. the direct and the indirect detection of X-rays. Indirect detectors first convert X-rays to visible light in a scintillator material. The visible light is subsequently converted to electrons in a photodiode. This signal is evaluated by an electrical readout unit and represents information on the X-ray intensity. Indirect detectors integrate the incoming X-ray intensity during the exposure time. Thus, they have no means to discriminate photons of different energy. Direct detection methods make use of sensor materials which directly convert incoming X-rays into an electric signal. This has the advantage that single photons can be counted when using appropriate readout units. Furthermore, it facilitates energy resolved measurements [51].

In conventional X-ray imaging the transmitted X-ray intensity is used to non-destructively study on the sample's internal structure. The sample is typically illuminated by a polychromatic X-ray beam and the transmitted fraction of the beam is recorded with a two-dimensional pixelated detector. Of course, the transmitted intensity is reduced when compared to the incoming intensity because of X-ray absorption. But also Compton scattering at large angles contributes to the loss in X-ray intensity. We refer to the combination of these two effects as X-ray attenuation. Based on the initial beam intensity I_0 and the transmitted intensity I_T , both detected by a pixel at the location (x, y) on the detector, we define a linear attenuation coefficient μ_{att} similar to equation 2.10. This attenuation coefficient is averaged over the full X-ray spectrum as conventional detectors do not allow for energy-resolved measurements. Furthermore, samples typically are not homogenous regarding their attenuation properties. Therefore, the multiplication of μ with the sample thickness Δz in equation 2.10 is replaced by an integral of μ_{att} through the object along its full length l_z along the z -axis. This integration results in following representation of the transmitted intensity I_T :

$$I_T(x, y) = I_0(x, y) e^{-\int_{l_z} \mu_{att}(x, y, z) dz} \quad . \quad (2.13)$$

Based on equation 2.13, we define the transmittance T behind a sample as follows:

$$T(x, y) = \frac{I_T(x, y)}{I_0(x, y)} = e^{-\int_{l_z} \mu_{att}(x, y, z) dz} \quad . \quad (2.14)$$

The sample's transmittance is measured in each detector pixel (x, y) and we refer to such X-ray images as transmittance images. Calculating the negative logarithm of the transmittance provides us with the line integral of μ_{att} in each detector pixel (x, y) . We refer to such X-ray images as attenuation projections $P(x, y)$:

$$P(x, y) = -\ln(T(x, y)) = \int_{l_z} \mu_{att}(x, y, z) dz \quad . \quad (2.15)$$

Based on equation 2.15, the full three dimensional distribution of the samples attenuation coefficient $\mu_{att}(x, y, z)$ is obtained by CT measurements [2, 3]. Here, images of the sample are acquired, while the sample is rotated around an axis which is perpendicular to the optical axis. By means of a filtered backprojection (FBP) algorithm, which is based on the Radon transform, $\mu_{att}(x, y, z)$ is reconstructed in three dimensions [52]. This allows to study internal features of a sample which are distinguishable based on their attenuation properties.

Typically, transmittance images and the corresponding attenuation projections show a geometrically magnified image of the object under investigation. The reason for this magnification is the divergence of an X-ray beam generated by a conventional X-ray tube.

2. THEORY

Figure 2.5 illustrates how a sample is magnified by a divergent X-ray beam. The magnification factor M is derived by geometrical considerations which result in the following equation:

$$M = \frac{d_{S,D}}{d_{S,S}} . \quad (2.16)$$

Here, $d_{S,D}$ is the distance between source and detector, while $d_{S,S}$ represents the distance between source and sample.

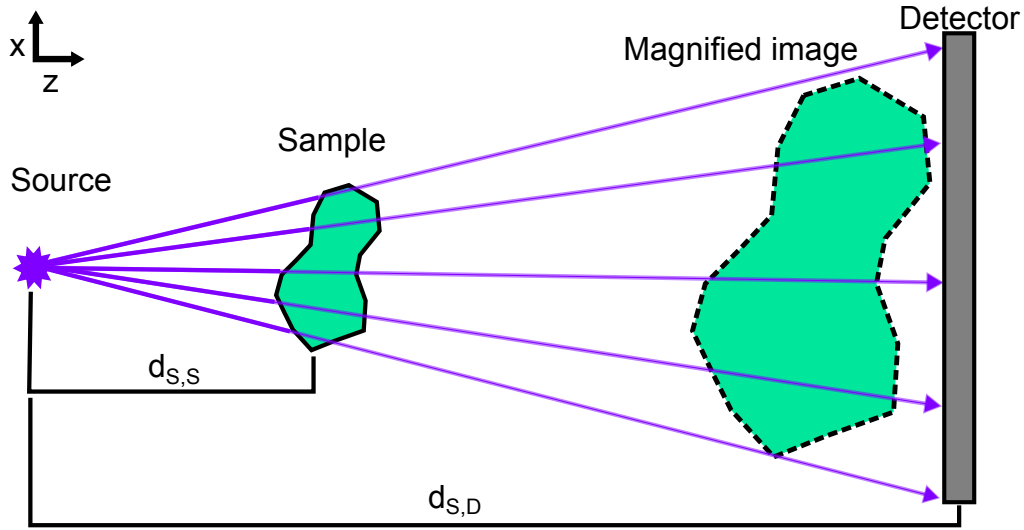


Figure 2.5.: This figure illustrates how a sample is magnified by a divergent X-ray beam. A conventional X-ray tube generates a divergent X-ray beam as indicated by the purple arrows. It illuminates a sample which is placed at a distance $d_{S,S}$ from the source. The beam's divergence results in a geometrical magnification of the sample. A magnified image (dashed contour) is therefore recorded by a detector placed at a distance $d_{S,D}$ from the source.

X-ray detectors measure the X-ray intensity, i.e. the squared amplitude of the wave, while information on the phase of the incoming X-ray wavefront is not obtained. Therefore, only the complex part of the refractive index is probed in conventional X-ray imaging. However, it is possible to determine the real part of the refractive index by measuring refraction angles.

2.2. Grating-based X-ray imaging

Measuring refraction angles is the basic principle of grating-based X-ray imaging in order to obtain information on the real part of the refractive index. Since refraction angles are typically very small for the X-ray regime, a reference pattern is used to transform the

refraction of X-rays into an intensity modulation which is then measured by conventional X-ray detectors. In the following we address this method in more detail.

2.2.1. The Talbot-Lau interferometer

Grating-based X-ray imaging with conventional X-ray equipment is based on a Talbot-Lau interferometer consisting of three microstructured gratings. These gratings are placed between the source and the detector at particular positions which are defined in the following sections. They either serve as absorption gratings or phase gratings. In the first case, X-rays are absorbed by the highly absorbing material of the grating lamellae. In the latter case, the grating lamellae are made of a weakly absorbing material and X-rays exhibit a phase shift when passing through the grating lamellae. Grating periods are typically in the range of $1 - 10 \mu\text{m}$, while the height of the grating structure reaches from several micrometers for phase gratings up to several hundred micrometers for absorption gratings. Due to those high aspect ratios, X-ray gratings are usually manufactured by a so-called LIGA process [53].

X-ray gratings and the Talbot-effect

The illumination of grating structures with electromagnetic waves was first studied and described by H. F. Talbot in 1836 [21]. While illuminating a grating with a coherent light source, Talbot observed a characteristic interference pattern. This pattern is periodically replicated at certain distances behind the grating creating a so-called Talbot-carpet. The Talbot-effect is also observable in the X-ray regime under certain conditions [18]. The distance d_T at which the pattern is repeated behind the grating is called Talbot-distance and it is defined as follows [45]:

$$d_T = \frac{2p_1^2}{\lambda} . \quad (2.17)$$

The grating structure has a period of p_1 and λ represents the X-ray wavelength. We refer to the grating that generates the Talbot-carpet as grating G_1 in the remainder of this work. Phase and absorption gratings both generate Talbot-carpets. Phase gratings, however, are generally preferred, because they do not absorb a considerable amount of the incoming intensity in contrast to absorption gratings. As this is beneficial for imaging we only consider phase gratings to be used as G_1 in this work.

An exemplary Talbot-carpet generated by a monochromatic plane wave behind a phase grating is illustrated in figure 2.6. Besides a repetition of this pattern along the propagation direction at a distance d_T , binary intensity profiles are formed perpendicular to the propagation direction at fractional Talbot-distances d_{frac} . This is illustrated by the purple profile on the right side of figure 2.6. Their period is given by the following equation [45]:

2. THEORY

$$p_2 = \frac{p_1}{m} . \quad (2.18)$$

Here, the parameter m is used to distinguish the following two cases. It is $m = 2$, in the case of a phase grating which introduces a phase shift of π to the wavefront, while it becomes $m = 1$ for a phase shift of $\pi/2$. These binary intensity profiles are replicated at fractional Talbot-distances d_{frac} [45]:

$$d_{frac} = \frac{l \cdot u}{16} d_T, \quad \text{with} \quad l = 1, 3, 5... . \quad (2.19)$$

Here the parameter u is used to distinguish between the following two cases. It is set to $u = 1$ for a phase shift of π , while it becomes $u = 4$ for a phase shift of $\pi/2$.

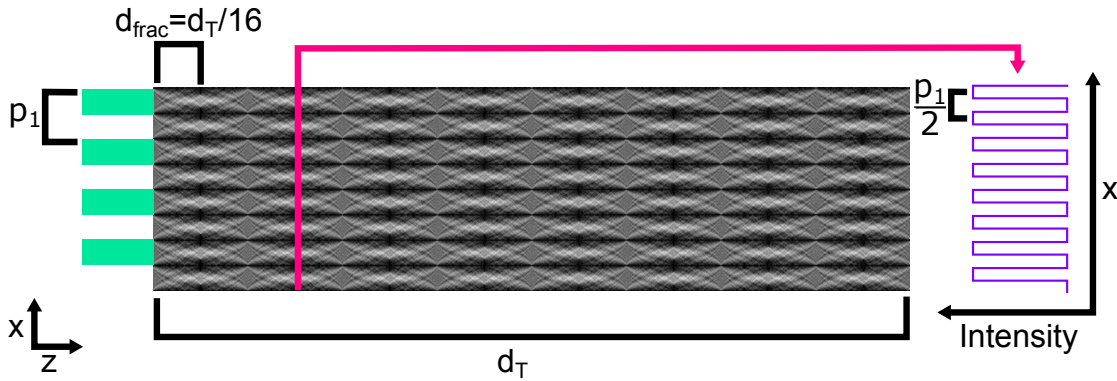


Figure 2.6.: This figure shows a Talbot-carpet generated by a phase grating of period p_1 . X-rays passing through the grating lamellae (green rectangles) are shifted in phase by π in this case. They interfere behind the grating and a Talbot-carpet is generated. At certain distances d_{frac} , binary intensity profiles (purple profile on the right) are observed perpendicular to the propagation direction. Their period is $p_1/2$ for the given scenario.

Equations 2.17, 2.18 and 2.19 were derived based on the assumption of a plane wave which intrinsically has a large transverse coherence length. This assumption is usually valid for X-ray beams generated by synchrotron sources. Making use of the Talbot-effect with laboratory X-ray tubes requires further considerations.

Conventional X-ray tubes and the source grating

First of all, conventional X-ray tubes generate divergent beams and therefore magnify the Talbot-carpet according to equation 2.16. The magnification has to be considered when calculating the fractional Talbot-distances and the period of the transverse intensity profile at these positions. This results in the following equation for d_{frac} [54]:

$$d_{frac} = M \frac{2p_1^2}{\lambda} . \quad (2.20)$$

The period p_2 of the transverse intensity profiles is calculated in this case as follows [54]:

$$p_2 = M \frac{p_1}{m} . \quad (2.21)$$

Here, the parameter m again distinguishes the two cases of a π phase shift ($m = 2$) and a phase shift of $\pi/2$ ($m = 1$). The factor M represents the magnification factor introduced in equation 2.16 [45]. The source to sample distance $d_{S,S}$ simply needs to be replaced by the source to grating distance d_{S,G_1} in this case.

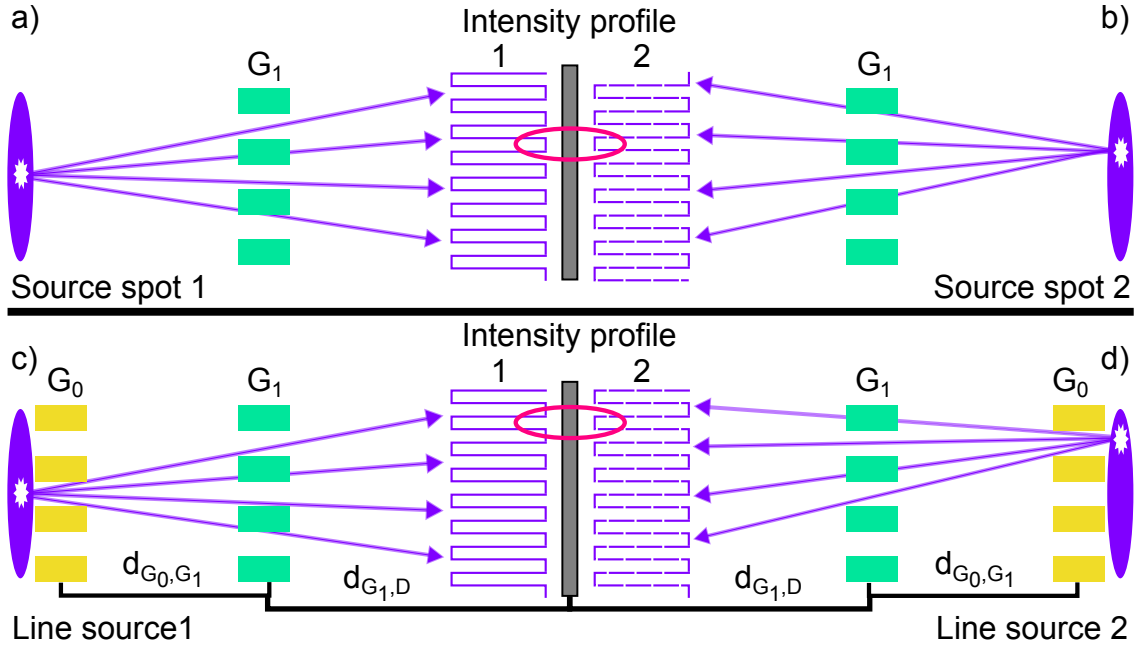


Figure 2.7.: This figure schematically illustrates the purpose of G_0 . **a) and b)** The two exemplary spots (white stars) of an extended source (purple ellipse) are laterally displaced. Source spot 2 is mirrored to the right hand side of the figure for a better visualization. X-rays emitted from these spots generate intensity profiles (purple profiles) which superimpose at the detection plane. According to the displacement of source spot 1 and 2, these intensity profiles are displaced as well. The minima of profile 1 coincide with the maxima of profile 2 (marked by a pink ellipse). This results in an overall flat intensity profile at the detection plane. **c) and d)** The extended source spot is divided into multiple thin line sources by a source grating G_0 . The intensity profiles created by two exemplary line sources are shown and the second line source is again mirrored to the right hand side. The separation between line source 1 and 2, i.e. the period of grating G_0 , results in a constructive superposition of the two profiles (marked by a pink ellipse). Thus, the binary intensity profile is maintained at the detection plane.

Furthermore, X-rays coming from different points of an extended source create Talbot-carpets that are displaced to each other perpendicular to the propagation direction. There-

2. THEORY

fore, the binary intensity profile is washed out as it is illustrated at the top of figure 2.7. Two exemplary source spots of an extended X-ray source are shown. Each spot gives rise to a Talbot-carpet. However, the intensity profiles are displaced according to the displacement between the two source spots. Their superposition results in a flat intensity line and the Talbot-effect is not observable in this case. To prevent this inadvertent superposition, a further grating is placed right behind the X-ray source [23]. This grating is also an absorption grating blocking parts of the beam and therefore allows for a constructive superposition only. According to geometric considerations, the period p_0 of this source grating is given by following equation [45]:

$$p_0 = p_2 \frac{d_{G_0, G_1}}{d_{G_1, D}} . \quad (2.22)$$

Here, d_{G_0, G_1} refers to the distance between source grating G_0 and phase grating G_1 , while $d_{G_1, D}$ is the distance between the phase grating G_1 and the detection plane.

X-rays only pass through the slits of the source grating. The intensity profiles originating from each slit superimpose constructively and the binary intensity profile is maintained. This is illustrated at the bottom of figure 2.7. This geometrical explanation of the source grating's function is further complemented by an increase of the beam's transverse coherence length due to G_0 . A coherent beam is a prerequisite to observe interference effects such as the Talbot effect. In terms of coherence, the source grating confines the extended source to several thin line sources. According to equation 2.3, the transverse coherence length of each line source is larger compared to that of the fully extended source. Each of these coherent line sources, therefore, gives rise to a Talbot-carpet that is superimposed with the Talbot-carpets originating from the other line sources. The longitudinal coherence length of the beam also affects the appearance of the Talbot-carpet. It was shown that a polychromatic beam blurs the Talbot-carpet along the propagation axis, while the transverse intensity patterns at fractional Talbot-distances are maintained [54].

Analyzing Talbot-carpets by phase-stepping

The period of a phase grating usually is in the range of 1–10 μm and the observed intensity profiles have a period of the same length scale according to equation 2.21. Analyzing a Talbot-carpet therefore requires detectors with a pixel size that is smaller than p_2 . Detectors with such small pixels only work efficiently with a high X-ray flux provided by synchrotron sources. Single grating imaging is therefore possible at synchrotron sources [55]. Conventional X-ray tubes do not provide a sufficient X-ray flux and it is therefore not feasible to use such high resolution detectors for imaging experiments with conventional X-ray tubes. Detectors used for laboratory-based X-ray imaging usually have a pixel size in the range of tenths of micrometers up to several hundreds of micrometers. Obviously, they do not allow to analyze the intensity profile of the Talbot-carpet directly. This

requires a third grating that is placed at the distance d_{frac} behind the phase grating G_1 [20]. This so-called analyzer grating is an absorption grating and its period p_2 ideally matches the period of the binary intensity profile [56].

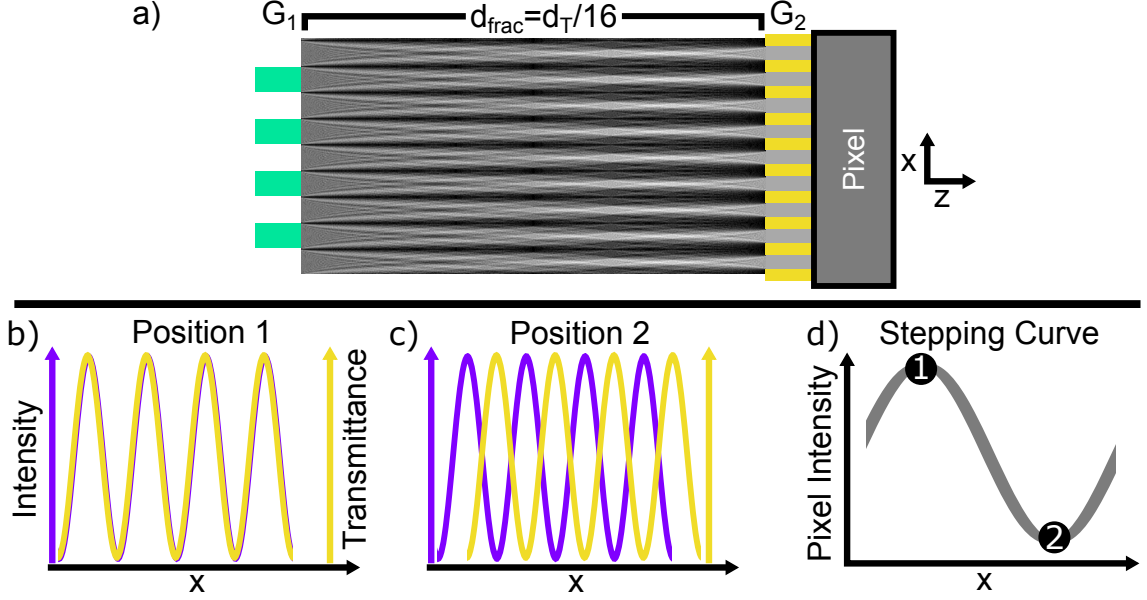


Figure 2.8.: This figure illustrates how a Talbot-carpet’s intensity profile is analyzed with large detector pixels. **a)** An analyzer grating with period p_2 is placed at the distance d_{frac} behind G_1 right in front of the detector. It is moved along the x -axis in order to analyze the Talbot-carpet. **b)** The transmittance function (yellow curve) of G_2 coincides with the intensity profile (purple curve) of the Talbot-carpet for position 1. Here, the maximum intensity is transmitted and detected by a detector pixel. **c)** The analyzer grating blocks the Talbot-carpet and the intensity transmitted to the detector is minimal for position 2. **d)** Plotting the intensity of one pixel for multiple grating positions results in the so-called stepping curve. This curve ideally has the same period as the analyzer grating and the intensity profile. Grating positions 1 and 2 are marked on the stepping curve.

The detector is placed right behind the analyzer grating. Figure 2.8 illustrates the corresponding experimental configuration. We refer to this analyzer grating as the grating G_2 . In order to analyze the Talbot-carpet, this grating is moved perpendicular to the propagation direction as well as the grating lamellae. This movement results in an intensity variation, which is recorded in each pixel of the detector by acquiring images for several positions of grating G_2 along the x -axis. Two exemplary grating positions are illustrated at the bottom of figure 2.8. This movement of the analyzer grating is often referred to as a phase-stepping scan [20]. It is mathematically described by a convolution of the Talbot-carpet’s intensity profile and the transmittance function (see equation 2.14) of the

2. THEORY

analyzer grating. This is illustrated by the purple and yellow curve in figure 2.8 b) and c). In a real case scenario, the intensity profile of the Talbot-carpet is rather smooth than rectangular as it has been shown for the ideal case before. The same is true for the transmittance function of G_2 owing to grating imperfections related to the manufacturing process. This convolution results in a periodic signal which is detected in each detector pixel. We refer to this signal as the stepping curve which is shown in figure 2.8 d). It is defined by a mean intensity, an amplitude and a phase parameter. These parameters represent an average over several periods of the Talbot-carpet's intensity profile for each pixel.

Thus, it is feasible to generate and analyze Talbot-carpets with conventional laboratory X-ray equipment by using a three grating Talbot-Lau interferometer. When a sample is placed before or behind the phase grating the original Talbot-carpet is distorted due to the interaction of X-rays with the sample. This distortion provides information on the refractive index and the scattering properties of the sample. In the following we explain how images are extracted from the acquired data.

2.2.2. Data processing and image formation

We reconsider the stepping curve (see figure 2.8) which is recorded in a pixel located at position (i, j) on the detector. We consider grating lamellae that are aligned perpendicular to the x-axis and parallel to the y-axis. In this case, the stepping curve is approximated by the following equation [24]:

$$f_{i,j,t}(x) = a_{0,t}(i, j) + a_{1,t}(i, j) \cos\left(\frac{2\pi x}{p_2} + \varphi_{1,t}(i, j)\right) \quad \text{with } t = s, r \quad . \quad (2.23)$$

The index $t = s, r$ indicates that the stepping curve has to be measured twice. One scan, i.e. a reference scan ($t = r$), is acquired without sample, while a second scan is acquired with the sample in the beam ($t = s$). The coordinate x indicates the movement of one of the three gratings along the x-axis. The interaction of X-rays and the sample results in a change of the three parameters a_0 , a_1 and φ_1 . This change is used to extract three different contrast channels.

Attenuation images

X-ray attenuation results in an overall loss of intensity of the Talbot-carpet according to equation 2.13. Since a_0 is the Talbot-carpet's intensity, it represents a projection of the attenuation coefficient through the sample for each pixel (i, j) [18]:

$$\int_{V_{sample}} \mu_{att}(i, j, z) dz = -\ln\left(\frac{a_{0,s}(i, j)}{a_{0,r}(i, j)}\right) \quad . \quad (2.24)$$

This equation emphasizes that attenuation images obtained by grating-based X-ray imaging provide the same information as conventional X-ray images. The image on the left hand side of figure 2.9 shows a transmittance image of a cup of cappuccino. The corresponding stepping curve of one pixel for the reference (purple solid line) and the sample measurement (green dashed line) is shown on the right. Strongly attenuating features of the sample correspond to bright pixels. Therefore, the glass side walls and the liquid coffee are clearly observable. The data points of the right plot represent the detected intensity in one pixel (marked by a green circle) for multiple positions of grating G_1 along the x-axis. Stepping curves are fitted to the data points according to equation 2.23.

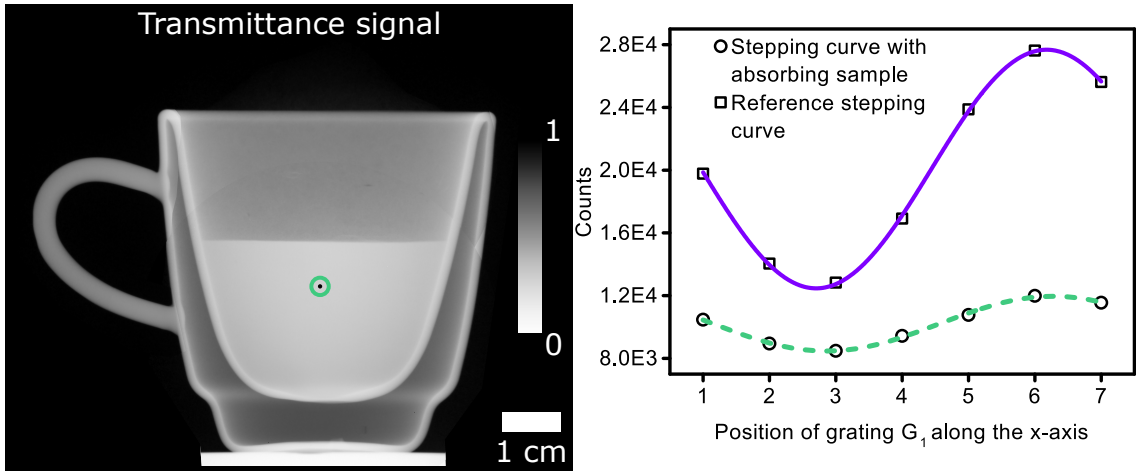


Figure 2.9.: This figure illustrates how transmittance images are extracted. A transmittance image of a cup of cappuccino is shown on the left. Highly attenuating features such as the glass side walls of the cup and the liquid coffee appear bright in the image. The stepping curve of the reference and sample scan of one pixel (marked by a green circle) are shown on the right. Due to X-ray attenuation, the sample curve has less overall intensity as compared to the reference curve.

Refraction and differential phase-contrast images

Besides attenuating the beam, the sample also shifts the phase of the X-ray wavefront. This phase shift is related to the real part δ of the refractive index n according to following equation [43]:

$$\Phi(x) = k \int_{V_{sample}} \delta(z, x) dz \quad . \quad (2.25)$$

According to equation 2.8, a gradient of this phase shift results in a refraction of the X-ray beam by an angle α . Therefore, information on the real part of the refractive index is

2. THEORY

obtained by measuring the refraction angles in each pixel of the detector. Refraction by an angle α into x-direction results in a shift $\Delta x_s = d \cdot \alpha$ of the Talbot-carpet along the x-axis at distance d behind the sample. Here, we assume that the angle α is very small which holds true for X-ray refraction in most cases [44]. Accordingly, the stepping curve is shifted as well and we define its phase term difference between reference and sample scan as follows:

$$\Delta\varphi_1(i, j) = \varphi_{1,r}(i, j) - \varphi_{1,s}(i, j) \quad . \quad (2.26)$$

This phase term difference is related to the lateral shift of the Talbot-carpet according to following equation [23]:

$$\frac{p_2}{2\pi} \Delta\varphi_1(i, j) = d_{s,G_2} \cdot \alpha(i, j) = \Delta x_s(i, j) \quad . \quad (2.27)$$

Here, p_2 represents the period of the analyzer grating G_2 , while d_{s,G_2} is the distance between sample and analyzer grating.

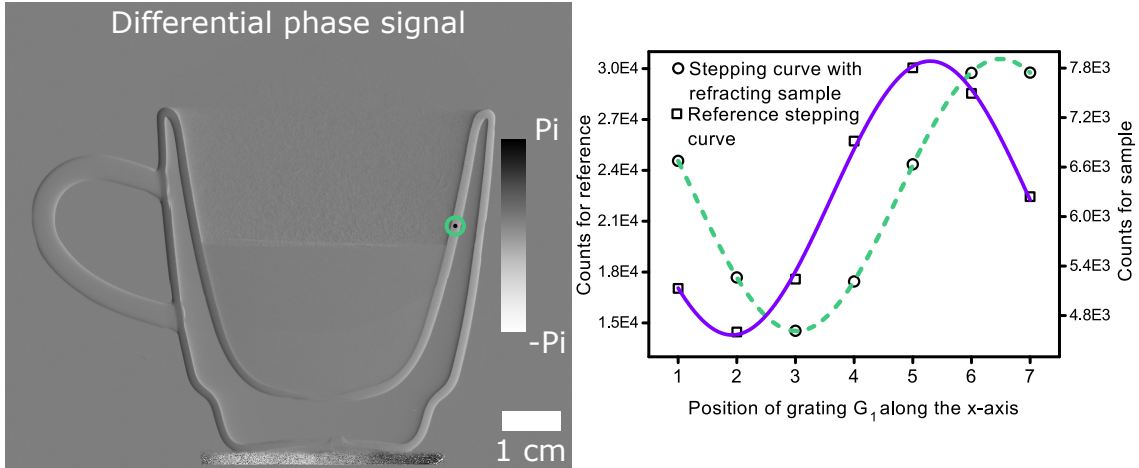


Figure 2.10.: This figure shows a DPC image of a cup of cappuccino. Depending on its curvature, the glass cup refracts the X-ray beam to the left or right. Therefore, the cup's side walls are shown by either bright or dark regions owing to the direction of refraction. Refraction by the liquid coffee is weak and not observable here. Stepping curves of the reference and sample scan of one pixel (marked by a green circle) are shown on the right hand side. The curve of the sample scan is shifted along the x-axis when compared to the reference scan. This shift is transformed into a differential phase signal according to equation 2.28. Note that the detected intensity is lower for the sample scan due to attenuation. This is indicated by the y-axis on the right.

Equation 2.27 represents the case when the sample is placed between gratings G_1 and G_2 . The case when the sample is placed between gratings G_0 and G_1 follows similar geometric

considerations [45]. When combining equations 2.25 and 2.8, a projection of δ is obtained based on the stepping curve's phase change $\Delta\varphi_1$ [45]:

$$\frac{\partial}{\partial x} \int_{V_{sample}} \delta(i, j, x, z) dz = -\frac{p_2}{2\pi d_{s,G_2}} \Delta\varphi_1(i, j) \quad . \quad (2.28)$$

Equation 2.28 emphasizes that grating-based X-ray imaging allows to measure the derivative of the projection of δ perpendicular to the grating lamellae. Therefore, we refer to such images as differential phase-contrast images. This differential contrast is illustrated in figure 2.10. The grating lamellae are oriented along the vertical axis and therefore refraction in the horizontal direction is observed only. Bright and dark features represent the glass walls because X-ray are refracted into negative and positive x-direction depending on the glass' curvature. Refraction caused by the liquid coffee is too weak in this case and therefore is not observable. The shift of the stepping curve along the x-axis is illustrated on the right hand side of figure 2.10. The data points (black hollow rectangles and circles) represent the detected intensity of one pixel (marked by a green circle) for several positions of grating G_1 along the x-axis. Stepping curves are fitted to the data points according to equation 2.23.

X-ray scattering and dark-field images

Grating-based X-ray imaging provides a third contrast channel besides X-ray attenuation and refraction. It is related to the ultra-small and small-angle scattering of X-rays originating from variations of the sample's electron density on a micrometer length scale [24–27]. These microscopic features do not refract the X-ray beam on a macroscopic scale, but instead scatter the beam. Scattered X-rays reduce the visibility of the Talbot-carpet's intensity profile, which we define for each pixel as follows [24]:

$$V(i, j) = \frac{a_1(i, j)}{a_0(i, j)} \quad . \quad (2.29)$$

The visibility reduction caused by a sample follows an exponential law similar to that of X-ray attenuation [57]. Therefore, we define a scattering coefficient ε , which is related to the visibility reduction according to following equation [57]:

$$\int_{V_{sample}} \varepsilon(i, j, z) dz = -\ln \left(\frac{a_{1,s}(i, j) a_{0,r}(i, j)}{a_{0,s}(i, j) a_{1,r}(i, j)} \right) = -\ln(DF) \quad . \quad (2.30)$$

Here, the visibility of the sample scan is normalized to the visibility of the reference scan. This normalized visibility is often referred to as the dark-field signal DF due to its similarity to visible light dark-field microscopy [24]. The physical meaning of the scattering coefficient ε is elaborated in more detail in chapter 4. We refer to such projections as dark-field or scattering images. Measuring the parameter a_1 , provides

2. THEORY

information on the sample's scattering properties. This is emphasized by the image on the left of figure 2.11 illustrating that the sample's microstructure results in a strong scattering signal. The cappuccino's milk foam produces a strong scattering signal due to the large number of liquid-air-interfaces in the milk foam. In contrast to that, the liquid coffee does not scatter because it is a homogenous liquid. Edge scattering is also observed for the vertical edges of the coffee cup.

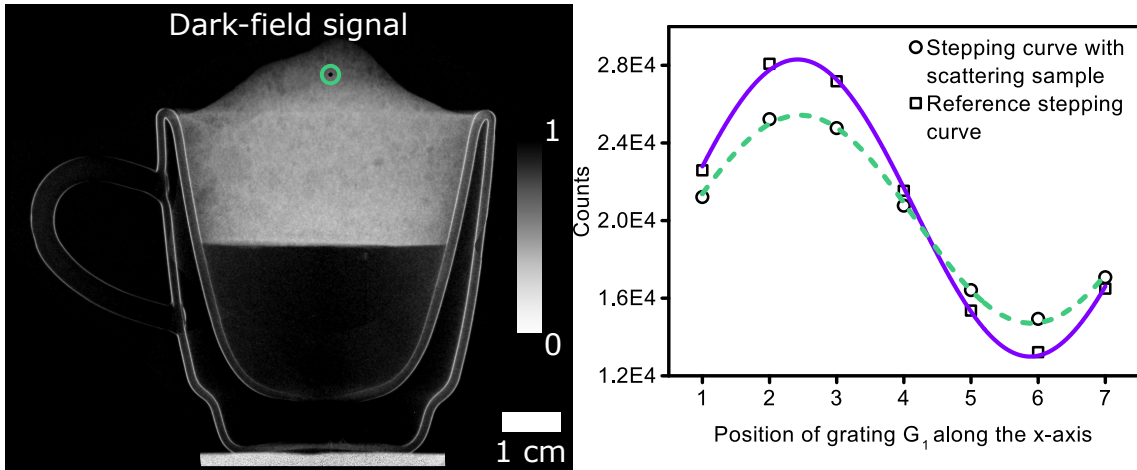


Figure 2.11.: This figure illustrates how scattering-based dark-field images are obtained. A dark-field image of a cup of cappuccino is shown on the left. The grating lamellae are oriented along the vertical. As edges scatter perpendicular to their edge profile, the cup's vertical edges produce a strong scattering signal. Here, the coffee does not scatter because it can be seen as a homogenous liquid in this scenario. Furthermore, a region of strong scattering is shown on top of the liquid. This region corresponds to milk foam, which scatters X-rays due to the large number of liquid-air-interfaces. Stepping curves of the reference and sample scan of one pixel (marked by a green circle) are shown on the right. The sample scan has a reduced amplitude when compared to the reference scan. Notably the stepping curve's mean intensity is not significantly reduced due to the foam's weak X-ray attenuation. This emphasizes that X-ray scattering reduces the visibility of the Talbot-carpet's intensity profile.

Because the grating lamellae are oriented along the vertical axis, the interferometer's sensitivity axis is along the horizontal. Edges give rise to scattering perpendicular to their edge profile resulting in a strong dark-field signal at the vertical edges. Furthermore, the visibility reduction is shown on the right hand side of figure 2.11 by the stepping curve of the reference (solid purple line) and sample scan (green dashed line). Notably, the stepping curve's mean intensity is not significantly reduced by the foam due to low attenuation. The data points (black hollow rectangles and circles) represent detected intensity of one pixel (marked by a green rectangle) for multiple positions of grating G_1 along the x-axis. Stepping curves are fitted to the data points according to equation 2.23.

Besides providing two dimensional images with transmittance, dark-field or DPC, equations 2.24, 2.28 and 2.30 allow for a tomographic reconstruction of the acquired data. Therefore, three dimensional information on the attenuation coefficient, the real part of the refractive index as well as the scattering coefficient are also accessible in grating-based X-ray imaging.

3. Details about the experimental system

This chapter contains detailed information about the experimental realization of an Talbot-Lau interferometer for X-ray imaging. All experiments, which are presented in this work, were obtained with the described experimental setup. Otherwise, modifications and other experimental equipment is addressed at appropriate positions later on.

3.1. X-ray tube and detector

A commercially available X-ray tube XWT-160-SE from X-ray Worx GmbH (Garbsen, Germany) serves as the X-ray source of the imaging system. It is an open microfocus tube operating in reflection mode. The tube provides acceleration voltages of 10 – 160 kV and a maximum target power load of 300 W at 160 kV. The anode's target material defining the emission spectrum is tungsten. X-rays exit the vacuum chamber through an aluminum window with a thickness of 2 mm. This window also serves as a filter for the tungsten spectrum by reducing the contribution of low energy X-rays. Furthermore, the beam is collimated to a cone beam with a half angle of 15°. The X-ray source spot is located at a distance of 0.6 cm from the tube's outer surface. It has an elliptical shape and its dimensions increase with increasing target power load. Up to 30 W, the small axis of the elliptical source spot increases from approximately 4 to 10 μm , while it increases rapidly from 10 to more than 100 μm for a target power load range of 30 – 150 W. Detailed measurements of the obtained X-ray spectrum and the shape and dimension of the X-ray source spot are presented in the master thesis of Markus Baier titled "*Experimental characterization and optimization of a high-resolution X-ray grating interferometer setup with respect to material research*" [58].

A commercially available flat panel detector PaxScan®2520DX from Varian medical systems (Palo Alto, USA) is used for image acquisition. It consists of a 600 μm thick scintillator screen made of columnar structured cesium iodide (CsI) and a photo diode matrix of amorphous silicon. The scintillator screen is positioned at a distance of 0.9 cm to the outer surface of the protection plate covering the scintillator. The physical size of each element of the photo diode matrix is 127x127 μm and each element represents one detector pixel. The total area covered by the 1920x1536 pixel is 24.4x19.5 cm^2 .

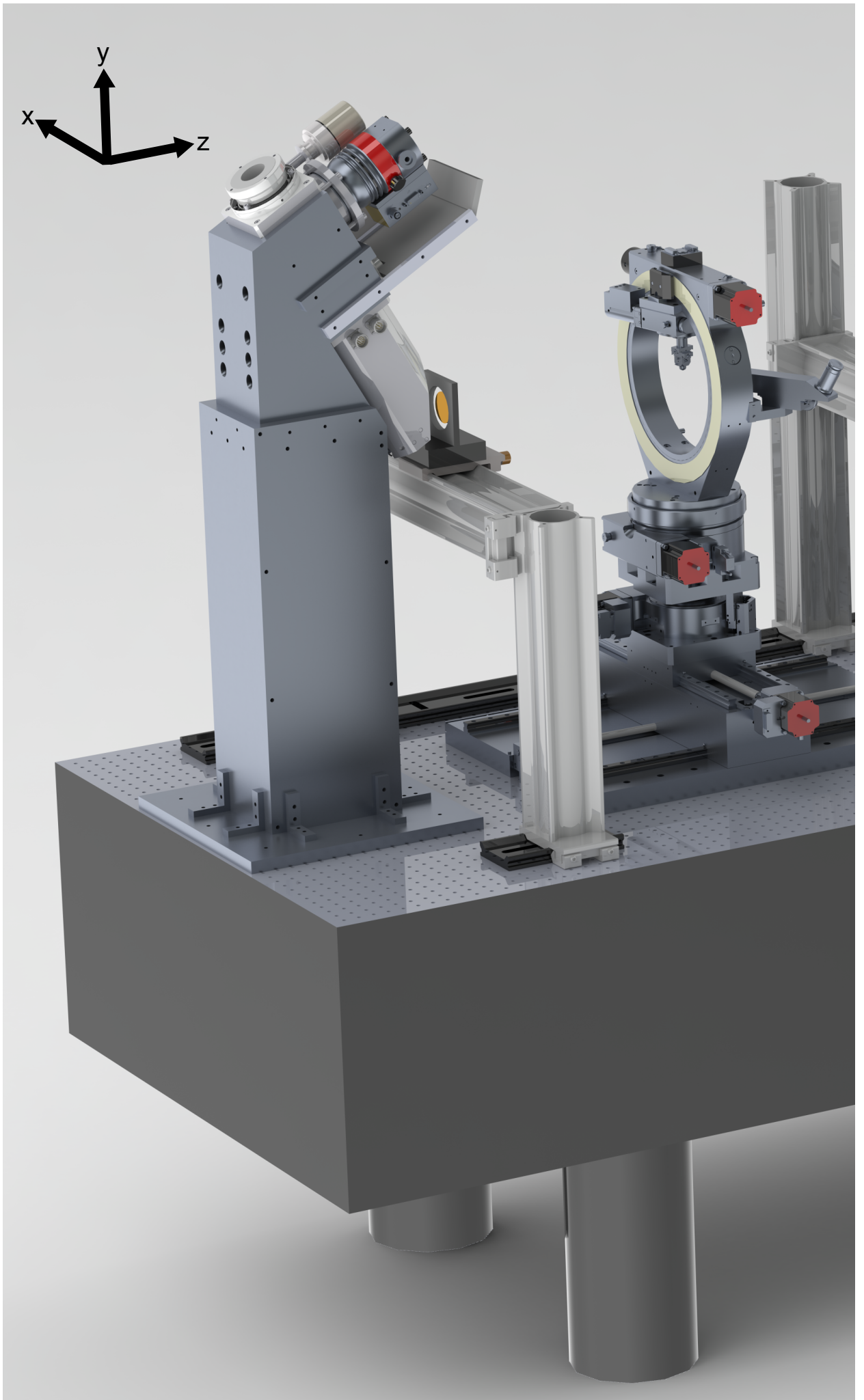


Figure 3.1.: 3D rendering of the experimental setup.

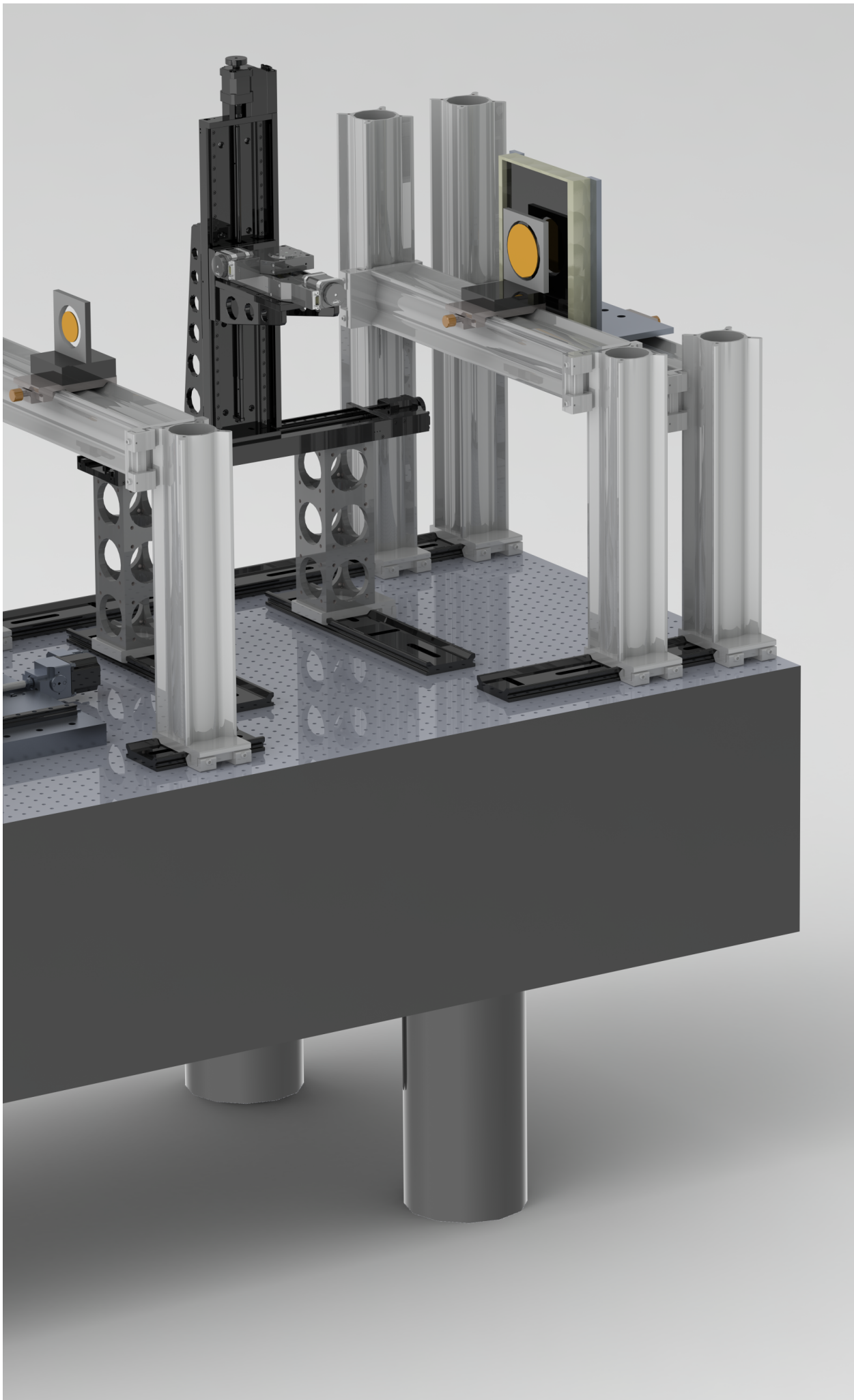


Figure 3.1 (continued)

3. DETAILS ABOUT THE EXPERIMENTAL SYSTEM

X-rays are converted to visible light by the scintillator and the photo diode matrix collects the visible light. The visible light signal is integrated for each acquired frame. The columnar structure of the CsI scintillator is beneficial for imaging because it reduces the point spread function (PSF) of the detector system when compared to an unstructured scintillator. Further details on the detector’s PSF are presented in the aforementioned master thesis of Markus Baier [58]. The read out unit of the detector operates at 0.5–12.5 frames per second (fps) but for most measurements we used a frame rate of 1 fps.

3.2. X-ray gratings and the Talbot-Lau interferometer

The grating interferometer consists of three microstructured gratings. Their grating lamellae are oriented along the y-direction for the presented experimental setup. Detailed parameters of the three gratings are presented in table 3.1.

Table 3.1.: Specifications of the three gratings used in this study

Grating	G_0	G_1	G_2
Effect	absorption	$\pi/2$ phase-shift	absorption
Lamellae material	Gold	Nickel	Gold
Material height [μm]	160 – 170	8	160 – 170
Grating period [μm]	10	5	10
Duty cycle	0.5	0.5	0.5
Substrate thickness [μm]	500	200	150
Geometry	Round d=5 cm	Round d=5 cm	Round d=9 cm
Layout	Bridge	/	Bridge

According to equation 2.7, the phase grating’s lamellae result in a phase shift of $\pi/2$ for an X-ray energy of 45 keV when taking the nickel height of 8 μm into account. We refer to this energy as the interferometer’s design energy, because it is the X-ray energy for which the phase grating results in the required phase shift. Therefore, the tube was operated at an acceleration voltage of 60 kV for all experiments giving rise to a mean energy of the X-ray spectrum of around 45 keV, taking into account absorption by the aluminum window and the energy dependence of the scintillator material’s absorption coefficient. Indeed, a maximum visibility of approximately 28% was obtained for energies of 40 – 45 keV by energy resolved measurements with the gratings described in table 3.1. Detailed information on the measurements and analysis of X-ray spectra are presented in reference [58]. The first fractional Talbot distance is 92.7 cm for the given parameters according to equation 2.20. Here, we also presume a symmetric interferometer with $d_{G_0,G_1} = d_{G_1,G_2}$ and a magnification factor of $M = 2$ for the phase grating. Due to experimental constraints, the source grating is placed at a distance of 8.5 cm to the tube, while the phase grating is positioned at a distance of 101.2 cm to the tube accordingly. The analyzer grating is placed at a distance of 193.9 cm to the tube. The detector is placed

1 cm behind the analyzer grating at a distance of 194.9 cm to the tube. The microfocus tube's small source spot at target power loads smaller than 10 W allows for the realization of a two grating interferometer omitting the source grating. This configuration was used for grating alignment prior to the measurements. The phase and analyzer grating were aligned without the source grating using a target power load of 10 W based on the Moiré fringe pattern. Then, the source grating was mounted and aligned to the phase and analyzer grating based on the Moiré fringe pattern. For reasons of time efficiency, the three grating configuration was used in all experiments because it allows high flux measurements due to large source spots. Stepping curves are obtained by moving the phase grating along the x-axis for reference and sample measurements. An illustration of the experimental setup is shown in figure 3.1. An Eulerian cradle is located between source and phase grating. It serves as a sample stage that moves the sample in x-, y- and z- direction and also rotates the sample by all three Eulerian angles. A second sample stage is located between the phase and analyzer grating. It allows to move the sample in x-, y- and z- direction as well as to rotate the sample around the y-axis.

3.3. Optimization of the system

The set of gratings presented in table 3.1 was the initial configuration of the experimental setup. During the course of this work, the performance of the setup was further improved by replacing the source and phase grating. The reference pattern's visibility is used as a measure for the performance of the setup. It is defined in equation 2.29 in chapter 2. Figure 3.2 displays three different visibility maps of the step-wise optimized setup. Measurements were performed with an acceleration voltage of 60 kV and a target power load of 100 W. In order to measure the stepping curve in each pixel, G_1 was moved in 7 steps by 5 μm along the x-axis. An image was acquired with an exposure time of 1 s for each step. The detector's framerate was set to 1 fps. The visibility maps in figure 3.2 represent the reference pattern's average visibility measured by each detector pixel.

Table 3.2.: Specifications of the new phase and source gratings used in this work.

Grating	G_0	G_1
Effect	absorption	π phase-shift
Lamellae material	Gold	Gold
Material height [μm]	200	8.6
Grating period [μm]	10	10
Duty cycle	0.5	0.5
Geometry	Round d=5 cm	Round d=5 cm
Layout	Sunray	/

While the new phase grating improved the visibility from 21.86% up to 24.56%, the new source grating resulted in a visibility increase to 31.18%. The major improvement caused

3. DETAILS ABOUT THE EXPERIMENTAL SYSTEM

by the new source grating is related to its layout. While the old source grating was based on a bridge design the new grating was produced with a sun-ray layout. More information on the different grating layouts is provided for example in reference [59]. Furthermore, the vertical lines of reduced visibility shown in figure 3.2 a) and b) are removed in image c). Those lines originated from heat damage of the old source grating due to a continuous use in high flux measurements. A detailed description of the new gratings is given in table 3.2.

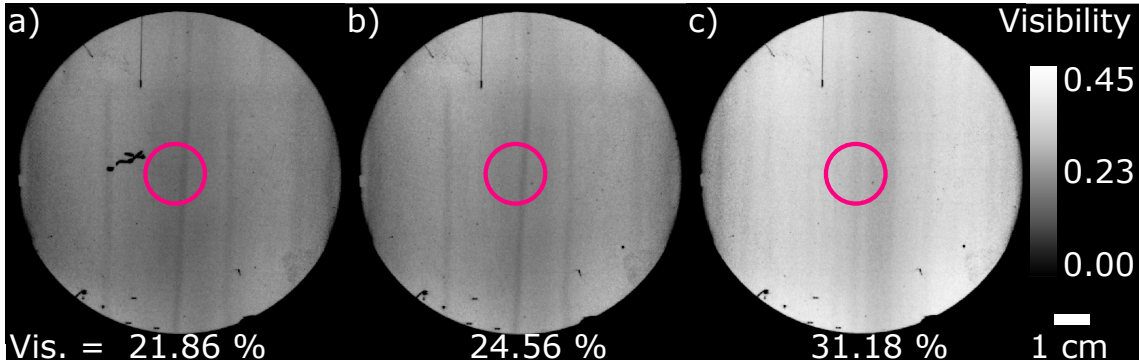


Figure 3.2.: a) The visibility map of the initial grating configuration given in table 3.1 is shown. The visibility of 21.86% was calculated from the region of interest indicated by the red circle. Besides some artifacts showing a visibility of 0% some vertical lines of reduced visibility perturb the circular field of view. b) The visibility map after implementing the new phase grating is shown. Details on this grating can be found in table 3.2. While the dominant artifact in the center of the field of view is removed, also the visibility increases to 24.56%. c) The visibility map is shown after implementing a new source grating (see table 3.2). While the vertical lines of reduced visibility have vanished, the visibility further increases to 31.18%. The remaining artifacts stem from defects on the analyzer grating, which are related to the manufacturing process.

The lamellae's gold height of $8.6 \mu\text{m}$ of the new phase grating results in a phase shift of π for an X-ray energy of 45 keV according to equation 2.7. Equation 2.20 therefore results in the same first fractional Talbot distance for the new grating as for the old phase grating. Thus, the interferometer's geometry was not changed. According to equation 2.21, the new phase grating's period was increased to $10 \mu\text{m}$, taking into account the magnification factor of $M = 2$ for the phase grating.

4. Quantitative X-ray dark-field imaging

In this chapter, a theoretical model for the quantification of the dark-field signal is developed. First, we give a summary on previous efforts and approaches to this problem. Having introduced basic concepts of scattering theory, a brief excursion is presented addressing a particular neutron scattering technique, which shares some physical characteristics with grating-based X-ray dark-field imaging. Further on, a theoretical framework is developed, which relates the dark-field signal to physical quantities known from classical scattering theory. Finally, we validate our theoretical findings with experimental results based on a novel experimental approach. This approach allows to obtain quantitative structural information on the nano- to micrometer length scale with grating-based imaging systems using laboratory X-ray equipment. The results presented in this chapter have been published in the following article:

F. Prade et al. "**Short-range order in mesoscale systems probed by X-ray grating interferometry**". In: *EPL* 112.6 (2015), p. 68002. DOI: 10.1209/0295-5075/112/68002

Parts of the following text were adapted from this article.

Literature overview

In first efforts, rigorous wave propagation theory was applied to relate the dark-field signal to structural properties of the sample. As a result, a relation between the dark-field signal and the auto-correlation function of the sample's microstructure was found [25, 26]. While Yashiro et al. restricted their considerations to a scenario where the sample was placed in front of the phase grating, Lynch et al. extended the obtained dark-field model for experiments where the sample is placed behind the phase grating. These theoretical findings were further experimentally supported by synchrotron measurements. Structural properties were successfully characterized in those experiments by measuring the dark-field signal of microparticle solutions with various interferometer configurations and X-ray energies. As a first exemplary application, the two dimensional auto-correlation function of a rubber sponge's microstructure was successfully studied using a synchrotron setup [61]. However, an experimental approach making such measurements feasible with laboratory X-ray sources has not been available so far. Recently, a general theoretical approach for

the dark-field signal's quantification was outlined by M. Strobl. It indicates some striking similarities between the dark-field signal and a neutron scattering technique known as spin-echo small-angle neutron scattering (SESANS) [27, 62–64]. M. Strobl confirmed the relation between the dark-field signal and the sample's auto-correlation function from the perspective of classical scattering theory. According to this relation, grating interferometers perform a back transformation of the object's scattering function into real space. Thus, a real-space correlation of the sample's microstructure is easily extracted in a quantitative manner by fitting experimental data with already available models of correlation functions. The transfer of synchrotron-based quantitative dark-field imaging as described in references [25–27, 61] to small-scale laboratory setups opens up new possibilities for materials research and non-destructive testing. In order to emphasize this potential, the following chapter provides detailed insight on the physical foundation of the dark-field signal based on the theoretical formalism of small-angle scattering techniques. We further describe the experimental feasibility to transfer this method to setups based on conventional X-ray tubes and present first experimental results.

4.1. Small-angle X-ray scattering

4.1.1. Differential scattering cross-section

Elastic X-ray scattering by a free electron has been introduced in chapter 2. Now, we elaborate further on the general formulation of scattering processes and their experimental application for the characterization of structural properties. Figure 4.1 illustrates important physical quantities which are used to formulate the measured scattered intensity.

We consider an X-ray beam of incoming flux Φ_0 which is scattered by an electron. The beam's flux is proportional to the squared amplitude Ψ_0 of the incoming wavefront. Hence, the scattered intensity I_{sc} is proportional to the product of the scattered flux Φ_{sc} and the area of the detector A_D , which is located at distance R_D to the electron and at solid angle $\Delta\Omega$. The following equation states these proportionality relations between the detected scattered intensity I_{sc} and incoming intensity I_0 with respect to solid angle $\Delta\Omega$ [43]:

$$I_0 \propto \Delta\Omega\Psi_0^2 \quad \text{and} \quad I_{sc} \propto R_D^2\Delta\Omega\Psi_{sc}^2 \quad \text{with} \quad R_D^2\Delta\Omega = A_D \quad . \quad (4.1)$$

The differential scattering cross-section $d\sigma/d\Omega$ is defined as the ratio of scattered to incoming intensity resulting in following equation:

$$\frac{d\sigma}{d\Omega} = \frac{I_{sc}}{I_0} = \frac{R_D^2\Psi_{sc}^2}{\Psi_0^2} \quad . \quad (4.2)$$

The scattered wave's amplitude $\Psi_{sc,1}$ originating from a single free electron is described by a spherical wave [43]:

$$\Psi_{sc,1}(\vec{R}) = -\frac{\Psi_0 a_{sc} e^{i\vec{k}\vec{R}}}{R} \quad (4.3)$$

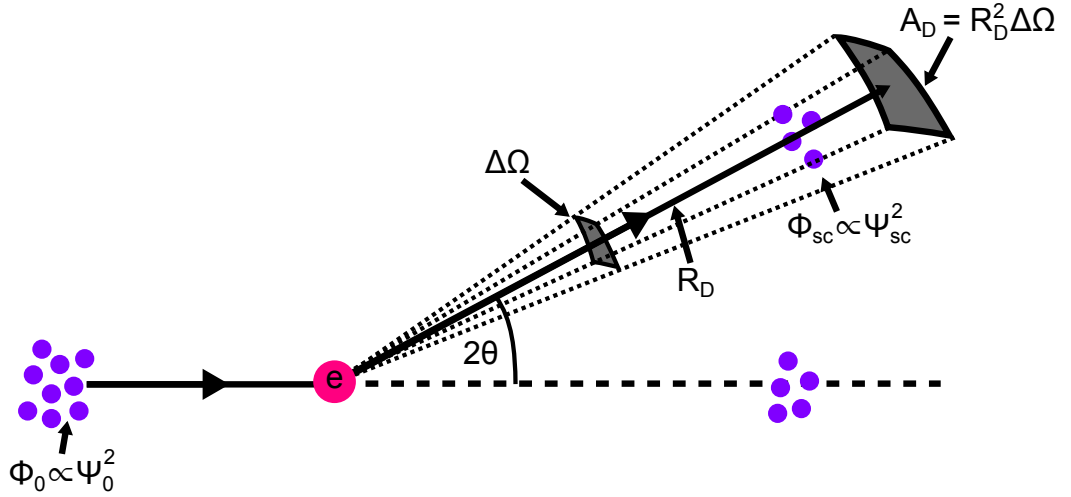


Figure 4.1.: This figure shows a schematic illustration of the differential scattering cross-section. An X-ray beam of incoming flux Φ_0 is scattered by an electron. A detector of area A_D detects X-rays scattered into solid angle $\Delta\Omega$ at a distance R_D . The flux of scattered X-rays is Φ_{sc} and it is proportional to the incoming wave's squared amplitude. Scattered and incoming intensities are proportional to the scattered and incoming flux multiplied by the corresponding area. The definition of the differential scattering cross-section $d\sigma/d\Omega$ is based on these quantities.

Here, a_{sc} represents the scattering amplitude or scattering length of the electron. It describes the strength of the scattering interaction. The parameter R is the modulus of vector \vec{R} which represents the position at which the scattered wave is observed. In the case of elastic X-ray scattering by a free electron, the scattering amplitude a_{sc} is represented by the classical electron radius or Thomson scattering length r_{el} and the polarization factor P (see equation 2.4). As mentioned in chapter 2, we restrict all considerations concerning scattering processes to free electrons. Under the assumption of small scattering angles and of $\theta < 0.1^\circ$ the electron's scattering amplitude reduces to r_{el} while $P = 1$ when using unpolarized X-ray sources [12].

4.1.2. Theoretical small-angle scattering formalism

The assumption of small scattering angles leads to the mathematical formalism of small-angle X-ray scattering (SAXS). It is derived by solving the Schrödinger equation of a wave

4. QUANTITATIVE X-RAY DARK-FIELD IMAGING

interacting with a potential. Iteratively solving the Schrödinger equation results in a series expansion for the solution of the scattered wave, which is called the Born series. This expansion can be restricted to its first term under the assumption of a weak potential. This results in the Born approximation for the solution of the scattered wave [65]. Assuming a weak potential is equivalent to an incoming wave which is constant within the scattering volume. In addition, SAXS also uses the following two geometrical simplifications: On one hand, the scattered wave resembles a plane wave as the wavefront's curvature is negligible at large a distance. Furthermore, the detector is placed far away from the scattering object and therefore $R_D \gg r$ when considering scattering by two electrons separated by \vec{r} .

Instead of solving the Schrödinger equation to obtain a solution for the scattered wave, we use a phenomenological approach starting from a two electron scenario. Figure 4.2 a) shows a schematic illustration of this case.

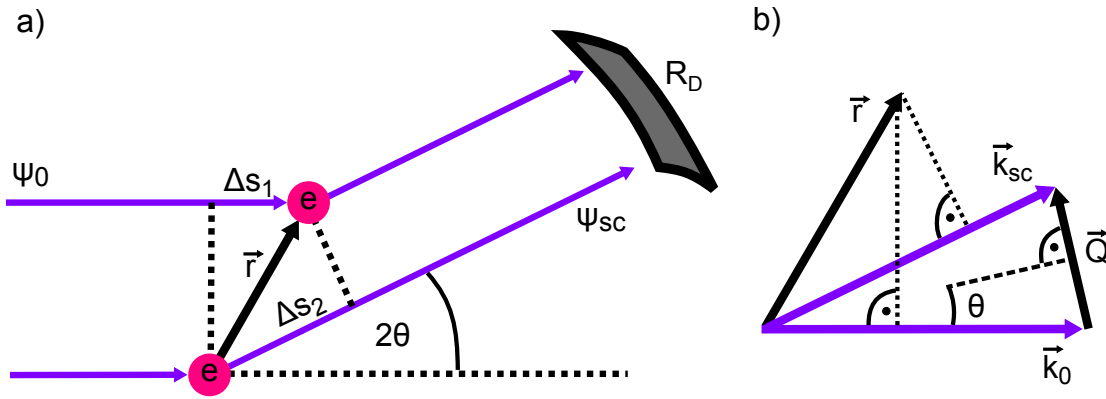


Figure 4.2.: This figure shows a schematic drawing of scattering by two electrons and a geometrical representation of the scattering vector \vec{Q} . **a)** An incoming wave is scattered by two electrons separated by \vec{r} . Due to the path difference $\Delta s = \Delta s_2 - \Delta s_1$ the two scattered waves have a phase difference $\Delta\Phi = (2\pi/\lambda)\Delta s$ when reaching the detector at distance R_D . For convenience we define the scattering angle as 2θ . **b)** The phase difference $\Delta\Phi$ is obtained by projecting vector \vec{r} onto the wavevectors \vec{k}_0 and \vec{k}_{sc} . This is indicated by the dashed lines orthogonal to \vec{k}_0 and \vec{k}_{sc} . Furthermore, the scattering vector \vec{Q} is defined by this geometry as $\vec{Q} = \vec{k}_{sc} - \vec{k}_0$.

An incoming wave is scattered by two electrons at an angle 2θ . The scattered waves originating from the two electrons travel different distances (Δs_1 and Δs_2) before reaching the detector. The path difference $\Delta s_2 - \Delta s_1$ results in a phase difference $\Delta\Phi$, which is calculated based on geometrical considerations as illustrated in figure 4.2 b). By projecting

4.1. SMALL-ANGLE X-RAY SCATTERING

vector \vec{r} onto the wave vectors of the incoming and scattered wave, \vec{k}_0 and \vec{k}_{sc} respectively, one obtains the following expression for $\Delta\Phi$ [12]:

$$\Delta\Phi = -\frac{2\pi}{\lambda}(\Delta s_2 - \Delta s_1) = -(\vec{k}_{sc}\vec{r} - \vec{k}_0\vec{r}) = -\vec{r}\vec{Q} \quad . \quad (4.4)$$

Here, we define the scattering vector \vec{Q} as the difference of the wavevectors \vec{k}_0 and \vec{k}_{sc} . The phase difference of the two scattered waves has to be considered when calculating the total scattered intensity. This results in the following expression of the scattered wave $\Psi_{sc,N}(\vec{Q})$ for the discrete case of N electrons [12]:

$$\Psi_{sc,N}(\vec{Q}) = -\frac{\Psi_0 r_{el} e^{ik_0 R_D}}{R_D} \sum_{j=1}^N e^{-i\vec{Q}\vec{r}_j} \quad . \quad (4.5)$$

The phase differences of all N electrons, which are located at a distance \vec{r}_j from an arbitrary point of origin, are summed up and multiplied with the scattered wave of a single electron (see equation 4.3). The more realistic scenario of a continuous electron distribution $\rho_{el}(\vec{r})$ requires some further considerations: A small volume dV , also written as d^3r , located at position \vec{r} contains $\rho_{el}(\vec{r})dV$ electrons that scatter with a phase difference of $\exp(-i\vec{Q}\vec{r})$ compared to an arbitrary point of origin. This is illustrated in figure 4.3.

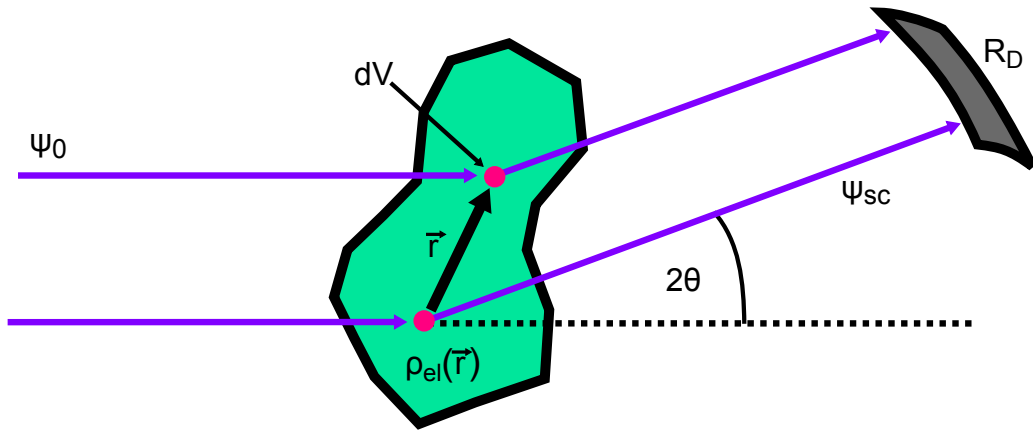


Figure 4.3.: This figure illustrates X-ray scattering by a continuous electron distribution. An incoming wavefront is scattered by a continuous distribution of electrons $\rho_{el}(\vec{r})$. Each volume element dV , also written as d^3r , of the sample scatters with a strength of $r_{el}\rho_{el}(\vec{r})dV$. A fraction of the incoming intensity is scattered at an angle 2θ and is detected at distance R_D .

As the number of electrons increases, we replace the summation in equation 4.5 by an integral over the sample's volume V_r . Thus, the scattered wave is represented as follows [12]:

4. QUANTITATIVE X-RAY DARK-FIELD IMAGING

$$\Psi_{sc,obj}(\vec{Q}) = -\frac{\Psi_0 r_{el} e^{ik_0 R_D}}{R_D} \int_{V_r} \rho_{el}(\vec{r}) e^{-i\vec{Q}\vec{r}} d^3r = -\frac{\Psi_0 e^{ik_0 R_D}}{R_D} \int_{V_r} \rho_{sl}(\vec{r}) e^{-i\vec{Q}\vec{r}} d^3r \quad . \quad (4.6)$$

Here, the scattering length density $\rho_{sl}(\vec{r}) = r_{el}\rho_{el}(\vec{r})$ is introduced. Furthermore, we define the final integration of this equation as the form factor $F(\vec{Q})$ of the scattering object [12]:

$$F(\vec{Q}) = \int_{V_r} \rho_{sl}(\vec{r}) e^{-i\vec{Q}\vec{r}} d^3r \quad . \quad (4.7)$$

Scattering of many equivalent objects separated by R_j is described similar to equation 4.5. In order to obtain the scattered wave, the form factors $F(\vec{Q})$ of all N particles are multiplied by a phase of $\exp(-i\vec{Q}\vec{R}_j)$ and summed up [66]:

$$\Psi_{sc,Nobj}(\vec{Q}) = \sum_{j=1}^N F(\vec{Q}) e^{-i\vec{Q}\vec{R}_j} = F(\vec{Q}) \sum_{j=1}^N e^{-i\vec{Q}\vec{R}_j} = F(\vec{Q}) S(\vec{Q}) \quad . \quad (4.8)$$

The term $S(\vec{Q})$ represents the so-called structure factor. It provides information on the distribution of scattering objects within the sample. The structure factor is negligible, if particles are distributed randomly, while it contributes significantly, if the object's distribution follows a certain pattern or order. Thus, as soon as particle positions are correlated in space, i.e. in the presence of short- or long-range ordering, $S(\vec{Q})$ strongly affects scattering experiments. Going further into detail on the structure factor is beyond the scope of this work. However, it is a useful tool to interpret some of the experimental results presented at a later point. But first, we continue with the derivation of the differential scattering cross-section.

To formulate the differential scattering cross-section using equation 4.2, the squared amplitude of the scattered wave is calculated by multiplication with its complex conjugate. This is represented by the following double integral [12]:

$$\Psi_{sc,obj}^2(\vec{Q}) = \Psi_{sc}(R_D) \Psi_{sc}^*(R_D) = \frac{\Psi_0^2}{R_D^2} \int_{V_r} \int_{V_{r'}} \rho_{sl}(\vec{r}) \rho_{sl}(\vec{r}') e^{i\vec{Q}\vec{r}} e^{-i\vec{Q}\vec{r}'} d^3r d^3r' \quad . \quad (4.9)$$

By defining $\vec{R} = \vec{r}' - \vec{r}$, this integral is rewritten as follows [12]:

$$\Psi_{sc,obj}^2(\vec{Q}) = \frac{\Psi_0^2}{R_D^2} \int_{V_r} \int_{V_R} \rho_{sl}(\vec{r} + \vec{R}) \rho_{sl}(\vec{r}) e^{-i\vec{Q}\vec{R}} d^3r d^3R = \frac{\Psi_0^2}{R_D^2} \int_{V_R} \gamma(\vec{R}) e^{-i\vec{Q}\vec{R}} d^3R \quad . \quad (4.10)$$

According to the Wiener-Khintchine Theorem, the squared amplitude of the scattered wave is given by the Fourier transform of the scattering length density's auto-correlation function $\gamma(\vec{R})$:

$$\gamma(\vec{R}) = \int_{V_R} \rho_{sl}(\vec{r} + \vec{R}) \rho_{sl}(\vec{r}) d^3r \quad . \quad (4.11)$$

Inserting equation 4.10 into equation 4.2 results in following expression for the differential scattering cross-section for a continuous electron distribution [12, 67]:

$$\frac{d\sigma}{d\Omega}(\vec{Q}) = \frac{1}{V_R} \int_{V_R} \gamma(\vec{R}) e^{-i\vec{Q}\vec{R}} d^3R \quad . \quad (4.12)$$

For convenience, the differential scattering cross-section is normalized to the object's volume V_R . The normalized cross-section yields the fraction of scattered X-rays observed at scattering vector \vec{Q} . Equation 4.12 emphasizes that scattering experiments determine the Fourier transform of the auto-correlation function of the scattering length density distribution. While the differential scattering cross-section represents the fraction of X-rays scattered by a scattering vector \vec{Q} , the total fraction of X-rays scattered in all directions is given by the integral of the differential scattering cross-section over the full \vec{Q} -space:

$$\sigma = \int_{V_Q} \frac{d\sigma}{d\Omega}(\vec{Q}) d^3Q \quad . \quad (4.13)$$

A further simplification is usually made in SAXS by setting the component of \vec{Q} pointing along the propagation direction to zero, i.e. here $Q_z = 0$. This is feasible as we assume elastic scattering at small angles for which the energy of scattered X-rays remains unchanged [68]. Consequently, the integration of the differential scattering cross-section along the z-axis can be carried out:

$$\frac{d\sigma}{d\Omega}(\vec{Q}) = \frac{1}{V_R} \int_{V_x, V_y} G(x, y) e^{-i(Q_x x + Q_y y)} dx dy \quad . \quad (4.14)$$

Here, the projection $G(x, y)$ of the auto-correlation function $\gamma(\vec{R})$ along the propagation direction, i.e. here the z-axis, is introduced. The projection is defined as follows [68]:

$$G(x, y) = \frac{1}{\Gamma} \int_{V_z} \gamma(x, y, z) dz \quad \text{or} \quad G(x, y) = \frac{1}{\sigma} \int_{V_{Q_x}, V_{Q_y}} \frac{d\sigma}{d\Omega}(\vec{Q}) \cos(Q_x x + Q_y y) dQ_x dQ_y \quad . \quad (4.15)$$

These two definitions yield the equivalent unit-less function $G(x, y)$ with $G(0) = 1$ and $G(\pm\infty) = 0$. We therefore introduce the unit-less parameter Γ to the first definition in equation 4.15 for reasons of normalization. The second definition uses an inverse Fourier transform of equation 4.12, which simplifies into a cosine transform assuming $\gamma(\vec{R})$ to be a real and even function, because $\exp(i\vec{Q}\vec{r})$ is equivalent to $\cos(\vec{Q}\vec{r}) + i\sin(\vec{Q}\vec{r})$. Only the cosine transform remains in this case while the sine transform vanishes. By performing the back transformation of equation 4.12 into real-space, structural information is obtained. Having developed the theoretical tools necessary to interpret scattering data, we now give a brief introduction to a particular neutron scattering technique. Spin-echo small-angle neutron scattering (SESANS) shares some striking physical characteristics with grating-based X-ray imaging. It serves as a basis to transfer the mathematical small-angle scattering formalism to Talbot-Lau interferometry [27].

4.1.3. Spin-echo small-angle neutron scattering

Figure 4.4 illustrates the basic configuration of a SESANS experiment. A polychromatic and divergent neutron beam is spin polarized along the x-axis by a polarizer. The polarized beam passes through two geometrically identical coils creating a magnetic field pointing into negative (coil 1) and positive y-direction (coil 2). The spin of the polarized beam precesses in the x-z-plane around the y-axis in those fields. However, as the magnetic fields are geometrically identical, but inverted along the y-axis, the polarization is preserved behind the two coils. The polarization is measured by an analyzer and a detector at the end of the experiment. A sample, which is placed between the two coils, scatters the neutrons. Scattered neutrons pass the second coil at an angle 2θ reducing the beam's polarization because the precession angle acquired due to the first coil 1 is not fully compensated by the second coil 2 anymore. The remaining polarization in x-direction P_{sc} of neutrons scattered by a scattering vector Q_x is calculated as follows [62]:

$$P_{sc}(Q_x) = P_0 \cos(\Delta\phi(Q_x)) \quad . \quad (4.16)$$

The scattering vector's z-component Q_z is negligible due to the restriction to small angles. Furthermore, the y-component Q_y is neglected as well because it does not influence the polarization in x-direction [62, 63]. P_0 represents the beam polarization observed without a sample. The argument of the cosine $\Delta\phi(Q_x)$ represents the remaining precession angle in the x-z-plane behind the second coil. It geometrically depends on the scattering vector Q_x . According to equation 4.13, a total fraction of σ of the neutron beam is scattered. The remaining fraction of neutrons $1 - \sigma$ contributes fully to the polarization. In contrast to that, neutrons scattered at scattering vector Q_x contribute to the polarization in x-direction according to equation 4.16. The fraction of scattered neutrons is given by the differential scattering cross-section $\frac{d\sigma}{d\Omega}(Q_x)$. The remaining polarization of the scattered fraction of neutrons is added to the polarization of the unscattered fraction of neutrons.

The total polarization P_{tot} observed by the analyzer is therefore calculated as follows [62, 67]:

$$P_{tot} = (1 - \sigma)P_0 + \int_{V_{Q_x}} \frac{d\sigma}{d\Omega}(Q_x)P_0 \cos(\Delta\phi(Q_x))dQ_x \quad . \quad (4.17)$$

Here, P_0 multiplied by $(1 - \sigma)$ accounts for the contribution of unscattered neutrons. The contribution of scattered neutrons is integrated over the full Q_x -space.

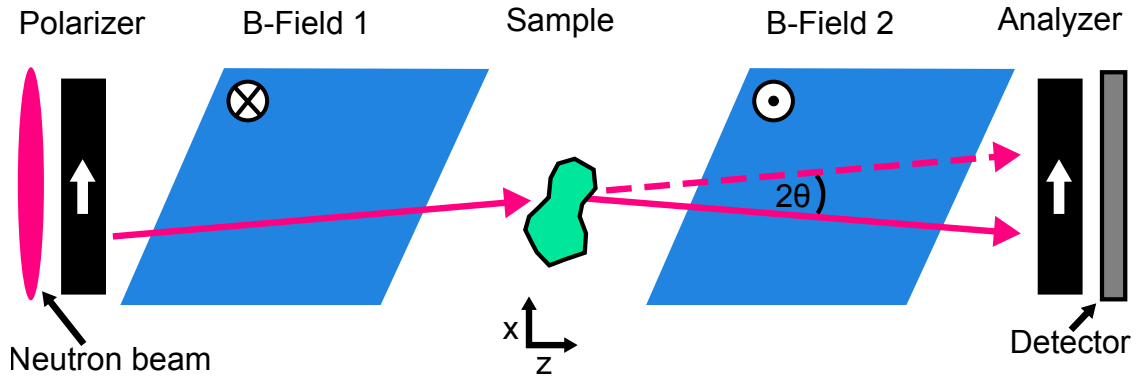


Figure 4.4.: This figure depicts an experimental setup for SESANS experiments. A polychromatic and divergent neutron beam is polarized along the x-direction by a polarizer. The polarized beam passes through two magnetic fields pointing along negative (field 1) and positive y-direction (field 2). The beam polarization is measured by an analyzer and a detector. A sample, which scatters neutrons by an angle 2θ , causes a loss in polarization along the x-axis.

By normalizing the remaining polarization with the initial polarization, and taking into account the definition of the correlation function $G(x)$ in equation 4.15, we obtain the following relation [62, 68]:

$$\frac{P_{tot}}{P_0} = 1 - \sigma + \sigma G(\xi_{corr}) \quad . \quad (4.18)$$

The variable ξ_{corr} depends on the geometry of the experimental setup and the magnetic field strength B . As equation 4.17 represents an inverse Fourier transform, ξ_{corr} represents the real-space transformation variable equation 4.18. It is usually in the range of a few micrometers. More details on the calculation of ξ_{corr} are presented in references [62, 63, 67, 68]. Equation 4.18 emphasizes that the normalized polarization yields information on the correlation function $G(\xi_{corr})$, which is defined in equation 4.15, and therefore allows to study the object's microstructure. For example, microstructural parameters of compressive powders and food products, such as cheese and yogurt were studied based on SESANS measurements [69, 70].

In a recent publication, physical similarities of SESANS and the dark-field signal were pointed out [27]. While the neutron beam's initial polarization is used similar to the visibility of a grating interferometer, the normalized polarization after interaction with a sample is physically equivalent to the dark-field signal [27]. Furthermore, the measured scattering signal is superimposed to the unscattered beam for both techniques and in both cases it is modulated by a cosine function. In SESANS, this modulation stems from the precession of the polarization vector, while in grating-based imaging it is caused by the modulation of the Talbot carpet's intensity profile. These common physical characteristics of both techniques immediately suggest to transfer the theoretical framework of SESANS to grating-based X-ray imaging to obtain a theoretical model for the dark-field signal. This is the purpose of the following section.

4.2. Implications of SAXS theory for the dark-field signal

In order to derive the physical meaning of the scattering coefficient ε introduced in equation 2.30 and its relation to quantities of scattering theory, we briefly recapitulate the working principle of a grating interferometer. The general layout of a Talbot-Lau interferometer is illustrated in figure 4.5. Its principle components are two absorption gratings G_0 and G_2 and a phase grating G_1 . Grating G_0 provides beam coherence necessary to observe interference [23]. Due to the fractional Talbot-Effect a characteristic intensity pattern, i.e. the Talbot-carpet, is created behind the phase-grating G_1 . Grating G_2 allows to analyze this pattern with conventional X-ray detectors, which usually have large pixels that do not allow to resolve the pattern directly [20].

We consider an incoming X-ray beam with intensity I_0 which illuminates the interferometer. If no sample interacts with the beam, the resulting intensity profile along the x-direction at the position of G_2 is well approximated according to equation 2.23 [57]. Here, a simplified representation is used by omitting the pixel position index, and considering only one pixel:

$$\frac{I_r(x)}{I_0} = a_0 + a_1 \cos \left[\frac{2\pi}{p_2} x \right] \quad . \quad (4.19)$$

The observed intensity profile shows a cosine modulation along the x-axis at the position of the analyzer grating. Its period depends on the period p_2 of G_2 . In the following, we refer to this intensity profile as the reference pattern denoted by the index r . The parameter a_0 represents the fraction of incoming intensity that is evenly distributed as the mean of the pattern, while a_1 gives the fraction that is transformed into the amplitude of the pattern. Both parameters, a_0 and a_1 , depend on the specifications of the gratings used, and they are unique for each combination of gratings and energy. They are therefore

4.2. IMPLICATIONS OF SAXS THEORY FOR THE DARK-FIELD SIGNAL

unique for each individual experimental setup. The purple curve in figure 4.5 represents such a reference pattern. If a sample is placed between G_1 and G_2 , a fraction of the beam is scattered by a scattering vector \vec{Q} according to the differential scattering cross-section $d\sigma/d\Omega(\vec{Q})$ (see equation 4.2). The interferometer is not sensitive to scattering in y -direction because the grating lamellae run along the y -axis. We will therefore neglect the y -component Q_y in the following considerations. Furthermore, the z -component Q_z vanishes due to the assumption of small scattering angles [62, 66].

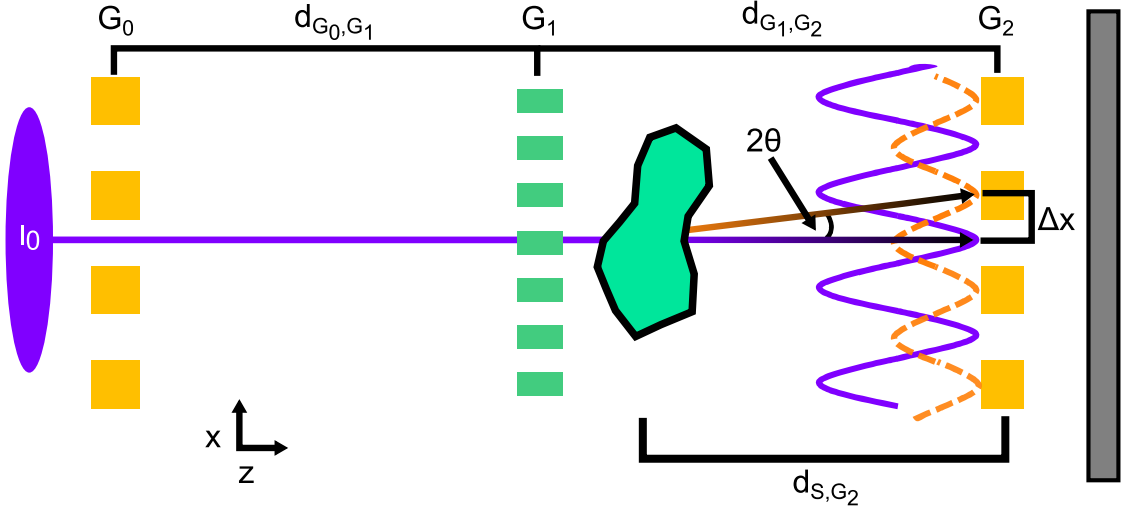


Figure 4.5.: This figure depicts the general layout of a Talbot-Lau interferometer and the observed reference pattern and a scattered pattern. The interferometer consists of a source of intensity I_0 , three gratings and a detector pixel. The purple solid curve represents the unscattered reference pattern. A sample positioned at a distance d_{S, G_2} to grating G_2 interacts with the X-rays. The orange dashed curve illustrates the pattern originating from X-rays scattered in x -direction at an angle 2θ . Both curves are shifted along the x -axis by Δx .

The scattered X-ray fraction gives rise to a periodic pattern similar to the reference pattern of the unscattered beam given by equation (4.19). In contrast to the reference pattern, this scattered pattern has less intensity, and it is slightly shifted by Δx along the x -axis due to scattering in this direction. An exemplary pattern of scattered X-rays is illustrated by the orange dashed curve in figure 4.5. It depends on Q_x and is formulated as follows:

$$\frac{I_s(Q_x, x)}{I_0} = a_0 t \frac{d\sigma}{d\Omega}(Q_x) + a_1 t \frac{d\sigma}{d\Omega}(Q_x) \cos \left[\frac{2\pi}{p_2} (x + \Delta x) \right] . \quad (4.20)$$

4. QUANTITATIVE X-RAY DARK-FIELD IMAGING

The differential scattering cross-section accounts for the fraction of intensity that is scattered by Q_x , while Δx accounts the scattered pattern's shift in x-direction. In the following, we refer to I_s as the scattered pattern denoted by the index s . Here, the thickness of the sample t is introduced in order to account for extended objects. In equation 4.2, $d\sigma/d\Omega$ of a single object is normalized to its volume. Hence, the scattered fraction of the whole sample is given by a multiplication of the differential cross-section with the sample thickness. X-ray attenuation is here neglected for reasons of simplicity. However, it is easily included by multiplication of equation 4.20 with an exponential term according to the Beer-Lambert law as stated in equation 2.14.

Besides being scattered, a certain fraction of the beam is transmitted, and superimposes the scattered pattern at the site of the detector. The pattern I_{us} of this unscattered fraction is obtained by multiplying the reference pattern stated in equation 4.19 with a factor of $(1 - \sigma t)$. We obtain the superposition I_{s+us} by adding the unscattered pattern I_{us} to the scattered pattern I_s stated in equation 4.20. This procedure results in following representation for the superposition I_{s+us} :

$$\begin{aligned} \frac{I_{s+us}(Q_x, x)}{I_0} = & \underbrace{(1 - \sigma t) \left(a_0 + a_1 \cos \left[\frac{2\pi}{p_2} x \right] \right)}_{I_{us}} \\ & + \underbrace{a_0 t \frac{d\sigma}{d\Omega}(Q_x)}_{I_s} \\ & + \underbrace{a_1 t \frac{d\sigma}{d\Omega}(Q_x) \cos \left[\frac{2\pi}{p_2} (x + \Delta x) \right]}_{I_s} . \end{aligned} \quad (4.21)$$

The superposition of scattered and unscattered pattern depends on Q_x . Thus, we integrate $I_{s+us}(Q_x, x)$ over the full Q_x -range because all scattering vectors contribute to the total observed intensity pattern I_{tot} :

4.2. IMPLICATIONS OF SAXS THEORY FOR THE DARK-FIELD SIGNAL

$$\begin{aligned}
 \frac{I_{tot}(x)}{I_0} &= (1 - \sigma t) \left(a_0 + a_1 \cos \left[\frac{2\pi}{p_2} x \right] \right) \\
 &\quad + a_0 t \int_{V_{Q_x}} \frac{d\sigma}{d\Omega} (Q_x) dQ_x \\
 &\quad + a_1 t \int_{V_{Q_x}} \frac{d\sigma}{d\Omega} (Q_x) \cos \left[\frac{2\pi}{p_2} (x + \Delta x) \right] dQ_x \quad . \quad (4.22)
 \end{aligned}$$

Under the assumption that the differential scattering cross-section is an even function, i.e. $\frac{d\sigma}{d\Omega} (Q_x) = \frac{d\sigma}{d\Omega} (-Q_x)$, the cosine term $\cos [x + \Delta x]$ can be split up according to following identity:

$$\frac{\cos [x + \Delta x] + \cos [x - \Delta x]}{2} = \cos [x] \cos [\Delta x] \quad . \quad (4.23)$$

Using equation 4.23 and the definition of the total scattering cross-section σ given by equation 4.13, equation 4.22 is rewritten as follows:

$$\begin{aligned}
 \frac{I_{tot}(x)}{I_0} &= (1 - \sigma t) \left(a_0 + a_1 \cos \left[\frac{2\pi}{p_2} x \right] \right) \\
 &\quad + a_0 t \sigma \\
 &\quad + a_1 t \cos \left[\frac{2\pi}{p_2} x \right] \int_{V_{Q_x}} \frac{d\sigma}{d\Omega} (Q_x) \cos \left[\frac{\lambda d_{S,G_2}}{p_2} Q_x \right] dQ_x \quad . \quad (4.24)
 \end{aligned}$$

A detailed derivation of equation 4.24 is given in appendix A. Here, we also used the following relation between Δx and the scattering vector Q_x under the small-angle approximation for the scattering angle 2θ :

4. QUANTITATIVE X-RAY DARK-FIELD IMAGING

$$\Delta x = \sin(2\theta) d_{S,G_2} \approx \frac{\lambda Q_x d_{S,G_2}}{2\pi} \quad . \quad (4.25)$$

This relation is derived based on simple geometric considerations shown in figures 4.5 and 4.2. Equation 4.24 can be further simplified, and using the correlation function $G(x)$ (see equation 4.15) finally yields the following expression for the I_{tot} :

$$\frac{I_{tot}(x)}{I_0} = a_0 + a_1 \cos \left[\frac{2\pi}{p_2} x \right] \times \left(1 - \sigma t + \sigma t G \left(\frac{\lambda d_{S,G_2}}{p_2} \right) \right) \quad . \quad (4.26)$$

Remarkably, this resembles the reference pattern given by equation 4.19 with just a slight modification. An additional term including the correlation function $G(x)$ is multiplied to the cosine term. This term is equal or less than unity, due to the definition of $G(x)$, and it consequently reduces the amplitude, or visibility, of the observed pattern I_{tot} .

Here, we emphasize that the argument $\lambda d_{S,G_2}/p_2$ of the correlation function in equation 4.26 corresponds to the beam separation of the first diffraction order as reported in references [71, 72]. From this point of view, the sample is scanned by a split beam and spatial correlations within the sample are probed at the length scale of this beam separation. We refer to the beam separation as ξ_{corr} in the remainder of this work. If the sample is placed in front of the grating G_1 , the beam separation equals to $\xi_{corr} = \lambda d_{G_0,S}/p_0$. Here, p_0 is the period of G_0 , and $d_{G_0,S}$ represents the distance between the source grating and sample. This corresponds to findings of previous publications [26, 27, 73]. Scanning the sample with a split beam is another characteristic that grating-based X-ray dark-field imaging shares with SESANS. Here, the neutron's spin wave is split into diffraction orders by the magnetic fields and the sample is scanned with this split beam [72]. Figure 4.6 illustrates how a sample is scanned by two beams spatially separated by ξ_{corr} .

The last line of equation 4.24 implies that a grating interferometer transforms the scattering function $d\sigma/d\Omega$ back into the system's correlation space. According to equation 4.15, this results in a direct relation between the dark-field signal and the correlation function $G(\xi_{corr})$.

The dark-field signal is defined as visibility (see equation 2.29) obtained with the sample normalized to the reference pattern's visibility. Dividing equation 4.26 by equation 4.19 results in the following expression for the dark-field signal DF :

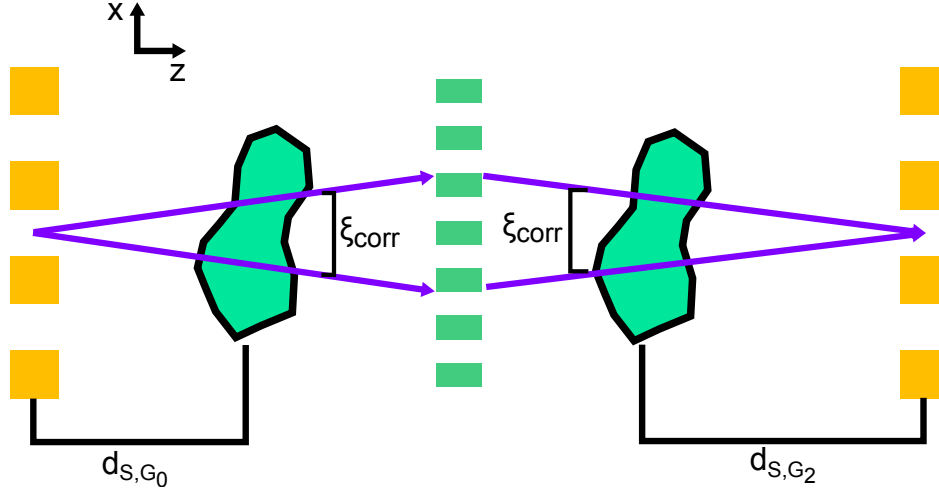


Figure 4.6.: This figure illustrates how a sample is scanned by a split beam in grating-based X-ray imaging. The gratings split the beam into the first diffraction order. The parameter ξ_{corr} represents the spatial separation of these diffraction orders. Correlations within the sample are probed on the length scale of the beam separation.

$$\begin{aligned}
 DF(\xi_{corr}) &= 1 - \sigma t + \sigma t G(\xi_{corr}) \\
 &= \exp[\sigma t (G(\xi_{corr}) - 1)] \\
 &= \exp \left[\int_{V_{Sample}} \sigma(z) (G(\xi_{corr}, z) - 1) dz \right] . \quad (4.27)
 \end{aligned}$$

The second line of equation 4.27 represents the case of scattering by many particles [74, 75], while the third line represents the case of inhomogeneous samples [27]. Here, the sample thickness t is replaced by a line integral through the sample equivalent to the line integral given in equation 2.24 in chapter 2.28. A similar result has been obtained in reference [76] under the assumption of a Gaussian differential scattering cross-section and the limitation to single scattering. Thus, the presented mathematical formalism provides a more general understanding of the dark-field signal.

Equation 4.27 directly relates the dark-field signal to the real-space correlation function $G(\xi_{corr})$ of the sample's microstructure. The correlation length ξ_{corr} determines at which specific length correlations within the sample are probed by dark-field measurements. As already outlined in the previous text, ξ_{corr} is calculated as follows:

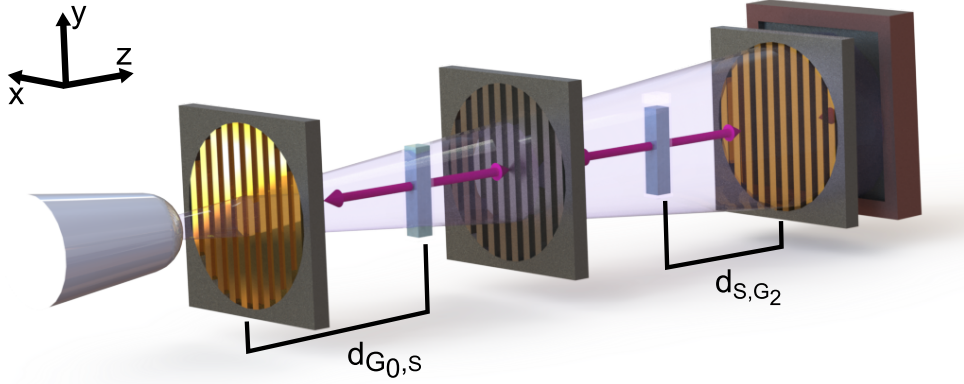


Figure 4.7.: This figure illustrates the experimental procedure to measure the correlation function $G(x)$ with a laboratory-based X-ray grating interferometer. The sample is placed either between G_0 and G_1 , or between G_1 and G_2 , and the correlation length ξ_{corr} is tuned by varying the sample's position. For each sample position, a dark-field image is acquired.

$$\xi_{corr} = \begin{cases} \frac{\lambda d_{S,G_2}}{p_2} & , \text{ if the sample is placed between } G_1 \text{ and } G_2 \quad , \\ \frac{\lambda d_{G_0,S}}{p_0} & , \text{ if the sample is placed between } G_0 \text{ and } G_1 \quad . \end{cases} \quad (4.28)$$

According to equation 4.28, the correlation function $G(x)$ can be evaluated for a certain range of the correlation length by tuning the parameter ξ_{corr} within the experimentally feasible limitations.

4.3. Experimental validation

Tuning ξ_{corr} is experimentally achieved by either moving the sample between G_0 and G_1 or G_1 and G_2 , while acquiring dark-field images at different sample positions defined by d_{S,G_2} or $d_{G_0,S}$. This experimental approach is illustrated in figure 4.7. In order to prove the experimental feasibility of this approach, and to validate the theoretical findings of the previous section, measurements on suspensions of microparticles were performed. Each sample contained silicon dioxide (SiO_2) microspheres of a well-defined diameter. Hence, suspensions of monodisperse spherical microparticles with following diameters (according to the manufacturer's specifications) were imaged: 0.519 ± 0.014 , 0.966 ± 0.03 , 2.79 ± 0.12 and $7.38 \pm 0.24 \mu\text{m}$. The microparticles were acquired from microparticles GmbH (Berlin, Germany). A photograph of the sphere suspension samples is show in appendix B in figure B.1.

4.3.1. Measurements on diluted suspensions of monodisperse microspheres

In the first experiment, the microspheres were suspended in water. The suspensions were filled into plastic cuvettes with rectangular cross-section and an inner diameter of 1 cm. 500 mg of SiO_2 microspheres were suspended in 2 ml of water for each sphere diameter. The specifications of the interferometer and the gratings used are given in table 3.1 in chapter 3. The tube was operated at 150 W. For each dark-field image, 7 phase steps were acquired with an exposure time of 2 s per step. The samples were either moved from G_0 to G_1 , or G_1 to G_2 in 5 mm steps, and a dark-field image was acquired for each sample position.

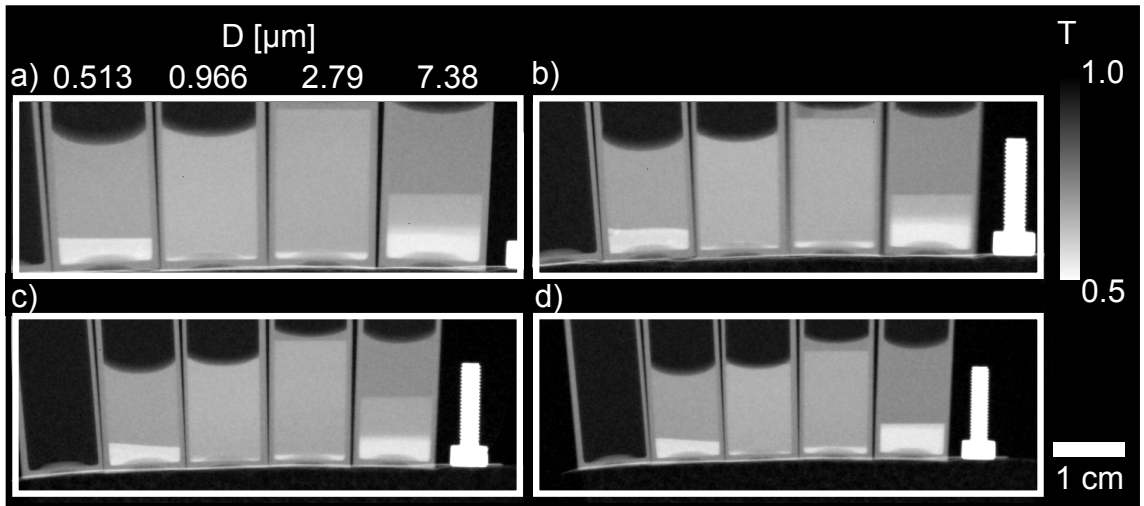


Figure 4.8.: This figure shows transmittance images of suspensions of monodisperse SiO_2 microspheres acquired at different sample positions $d_{S,G_2} = 0.646$ m (a), $d_{S,G_2} = 0.446$ m (b), $d_{S,G_2} = 0.246$ m (c) and $d_{S,G_2} = 0.046$ m (d). As the sample moves closer to G_2 , magnification decreases. It is important to note that no effect on the transmittance signal is observable.

Figure 4.8 shows transmittance images of four microsphere suspensions at different sample positions. The samples appear with less magnification as the distance d_{S,G_2} decreases, while the transmittance signal remains unchanged for each position. Regions of increased attenuation are located at the bottom of the cuvettes containing microspheres with diameters of 0.513, 2.79 and 7.38 μm . These regions correspond to SiO_2 spheres that settled onto the cuvette's bottom prior and during the experiment. These regions are not considered for the evaluation of this experiment as we focus on the suspension first. However, due to the sphere's settling the exact sphere concentration cannot be stated for this experiment.

4. QUANTITATIVE X-RAY DARK-FIELD IMAGING

The corresponding dark-field images of this measurement are displayed in figure 4.9. In contrast to the transmittance signal, the dark-field signal shows a strong dependence on the sample position. The scattering signal of the four suspensions reduces, and the samples have vanished from image d) of figure 4.8 when close to G_2 . In order to emphasize this observation, we calculate the mean dark-field signal averaged over the region of interest (ROI), which is marked by the green rectangles in figure 4.9. This was done for the suspension containing microspheres with a diameter of $0.519 \pm 0.014 \mu\text{m}$. The resulting mean dark-field signal is plotted against the system's correlation length ξ_{corr} in figure 4.10.

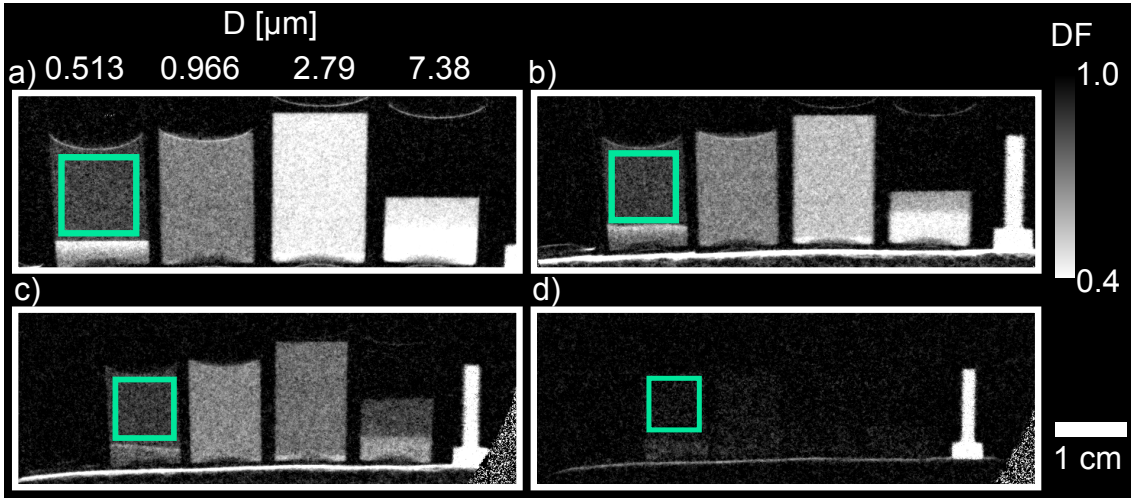


Figure 4.9.: This figure shows dark-field images of suspensions of monodisperse SiO_2 microspheres at different sample positions $d_{S,G_2} = 0.646 \text{ m}$ (a), $d_{S,G_2} = 0.446 \text{ m}$ (b), $d_{S,G_2} = 0.246 \text{ m}$ (c) and $d_{S,G_2} = 0.046 \text{ m}$ (d). When the samples are close to G_2 , image magnification decreases. The dark-field signal strongly depends on the sample's position. As the scattering signal decreases when the sample is positioned close to G_2 , the samples have almost vanished in image d).

The correlation length was calculated according to equation 4.28 assuming a mean X-ray energy of 45 keV. A correlation length of $\xi_{corr} = 0$ corresponds to the case when the sample is placed exactly at the position of G_2 . The averaged dark-field signal approaches unity for small values of ξ_{corr} , i.e. when the sample is close to G_2 . The signal decreases quickly with increasing ξ_{corr} , and reaches a constant level just below 0.875 for a correlation length of $\xi_{corr} > 0.5 \mu\text{m}$. This visual examination already provides qualitative information on the sample's microstructure.

The correlation function $G(x)$ basically describes the overlap of two spheres separated by x [68]. An illustration of this is given in figure 4.11. Hence, correlation only exists if this separation is smaller than the sphere's diameter. Hence, the correlation function $G(\xi_{corr})$ drops to zero for $\xi_{corr} > D$. According to equation 4.27, the dark-field signal

reaches a constant level of $DF = \exp(-\sigma t)$ in this case. This behavior is shown by the dark-field signal's curve in figure 4.10. In addition to that, a quantitative characterization of the sample's microstructure is feasible with the appropriate model for the correlation function $G(x)$. In the case of a sphere, $G(x)$ is analytically known and is approximated by the following equation [63, 67]:

$$G_{sphere}(x) \approx \exp\left[-\frac{9}{8}\left(\frac{x}{R}\right)^2\right]. \quad (4.29)$$

The parameter R approximately represents the sphere's radius. Using this model, it is possible to fit the experimental data by inserting equation 4.29 into equation 4.27. The pink curve in figure 4.10 represents the resulting fit. The fitting parameter R is $0.223 \mu\text{m}$ for this measurement. This finding is in good agreement with the sphere's actual diameter of $0.513 \mu\text{m}$ taking the precision of the manufacturer's specifications as well as measurement errors into account. These errors mainly originate from the accuracy of sample positioning, which is assumed to be $\pm 2 \text{ cm}$. Errors of the sample position translate directly into errors when calculating the correlation length. Therefore we obtain an error of $\Delta\xi_{corr} = 0.06 \mu\text{m}$.

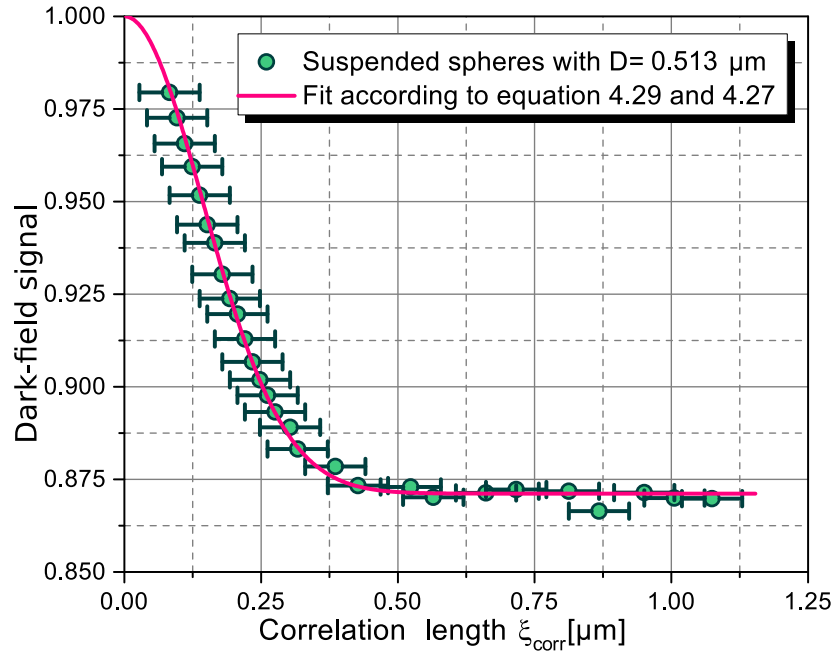


Figure 4.10.: This graph shows the mean dark-field signal of a suspension of SiO_2 microspheres with a diameter of $0.513 \mu\text{m}$. The dark-field signal is plotted against the correlation length ξ_{corr} . The sample was moved from G_0 to G_1 in 5 mm steps. The number of data points is reduced to provide a good visualization. The error-bars in x-direction are dominated by the accuracy of the sample position of 2 cm and result in $\Delta\xi_{corr} = 0.06 \mu\text{m}$. The data was fitted according to equation 4.29.

4. QUANTITATIVE X-RAY DARK-FIELD IMAGING

We neglect errors of the grating period and the mean energy of the X-ray spectrum. Equation 4.27 further contains the parameter σ which is provided by the fit as well. It contains information on the microparticle concentration and the difference of electron density between water and SiO_2 [68]. However, due to the sphere's settling on the bottom of the cuvette the sphere concentration was unknown, and we therefore omit a quantitative analysis of σ .

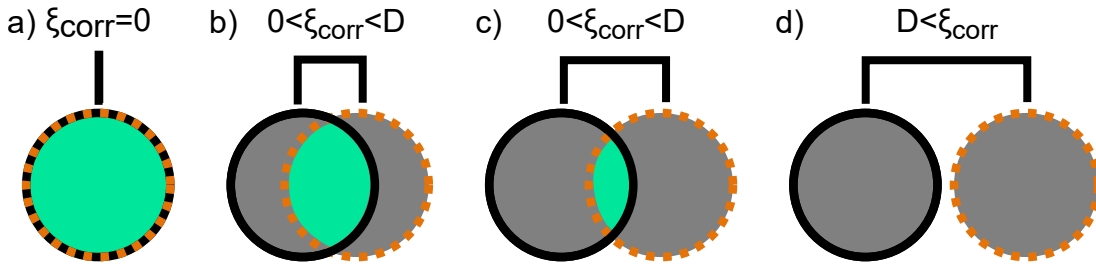


Figure 4.11.: This figure shows a graphical interpretation of the auto-correlation function of a sphere. The sphere's auto-correlation function is represented by the overlap of two spheres with diameter D . One sphere is shown by a black solid circle, while the other sphere is shown by a orange dashed circle. By increasing the separation ξ_{corr} between the two spheres, their overlap decreases. **a)** For $\xi_{corr} = 0$, the spheres perfectly overlap and the shared volume (green region), i.e. the correlation function, is at the maximum. **b) and c)** When ξ_{corr} increases the shared volume decreases along with the correlation function. **d)** As soon as the separation becomes larger than the sphere's diameter $\xi_{corr} > D$, the shared volume decreases to 0 as no correlation exists.

The average dark-field signal was calculated for each suspension sample. The spheres with diameter $D = 7.68 \mu\text{m}$ settled quickly, and a sufficient fraction of suspended microspheres was not maintained long enough to allow an analysis. Figure 4.12 shows the average dark-field signal for three suspensions containing spheres of diameters $D = 0.513$, $D = 0.966$ and $D = 2.79 \mu\text{m}$. Graph a) represents the measurements in which the samples were placed between G_0 and G_1 , while graph b) represents the measurement in which the samples were placed between G_1 and G_2 . The data points of each sample are axisymmetric to the phase grating G_1 . This symmetry validates equation 4.28, which formulates the correlation length ξ_{corr} . The correlation length ξ_{corr} is given at the top x-axis of each graph. It linearly decreases from $\xi_{max} \approx 2.5 \mu\text{m}$ at the position of G_1 to $\xi_{corr} = 0 \mu\text{m}$ at the positions of G_0 or G_2 , respectively. A reliable visual interpretation of the curve's that represent the microspheres with a diameter $D = 2.79 \mu\text{m}$ is not feasible because the diameter is well above the maximum correlation length of the interferometer. This maximum length is given by $\xi_{max} = \lambda d_{G_1, G_2} / p_2 \approx 2.5 \mu\text{m}$ when inserting the parameters given in table 3.1. A continuous signal decrease towards grating G_1 is therefore observed, and a constant level is not reached in this case. The dark-field signal curve representing the

4.3. EXPERIMENTAL VALIDATION

spheres with a diameter of $0.966 \mu\text{m}$ shows a different behavior as a minimum is observed before the dark-field signal levels out at a constant level of $DF = 0.7$. In this case, the constant level is reached at a correlation length of $\xi_{corr} > 1 \mu\text{m}$. Therefore, we can estimate the sphere diameter in this case to be around $1 \mu\text{m}$, which is in good agreement to the manufacturer's specifications. Unfortunately the minima, which was observed for this sample, does not allow a quantitative analysis according to equation 4.29.

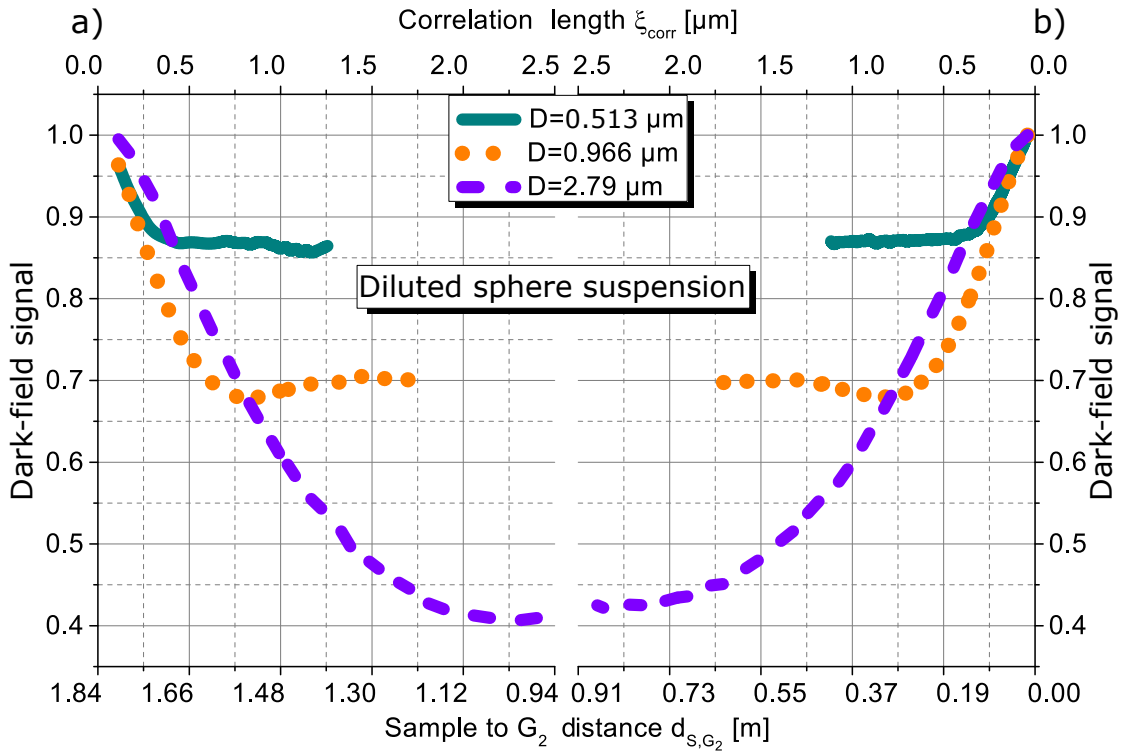


Figure 4.12.: The two graphs show the mean dark-field signal of SiO_2 microsphere suspensions containing spheres with diameters of $D = 0.513 \mu\text{m}$ (green solid curve), $D = 0.966 \mu\text{m}$ (orange dotted curve) and $D = 2.79 \mu\text{m}$ (purple dashed curve). Graph a) shows data for measurements obtained with samples placed between G_0 and G_1 , while graph b) shows data obtained with the sample between G_1 and G_2 . The curves are axisymmetric to the position of G_1 . While the dark-field signal of spheres with a diameter of $D = 2.79 \mu\text{m}$ continuously decreases when moving towards G_1 , the other two samples show a constant dark-field signal for certain correlation lengths. The sphere's diameters can be qualitatively determined based on this constant dark-field signal. In addition to that, a minimum is observed for the spheres with a diameter of $D = 0.966 \mu\text{m}$.

4.3.2. Measurements on dense monodisperse microsphere suspensions

In order to understand the origin of this minima a second experiment was conducted. The second experiment was conducted according to the same protocol of the first experiment. But for this experiment, the spheres were allowed to settle on the bottom of the plastic cuvettes. This resulted in a highly concentrated dense sphere suspension. The spheres occupied a volume of approximately 0.5 ml in this case resulting in a SiO_2 concentration of 1 g/ml. The samples were positioned either between G_0 and G_1 , or between G_1 and G_2 . Dark-field images were acquired at several sample positions separated by 5 mm. The average dark-field signal was calculated for a ROI covering the settled microspheres.

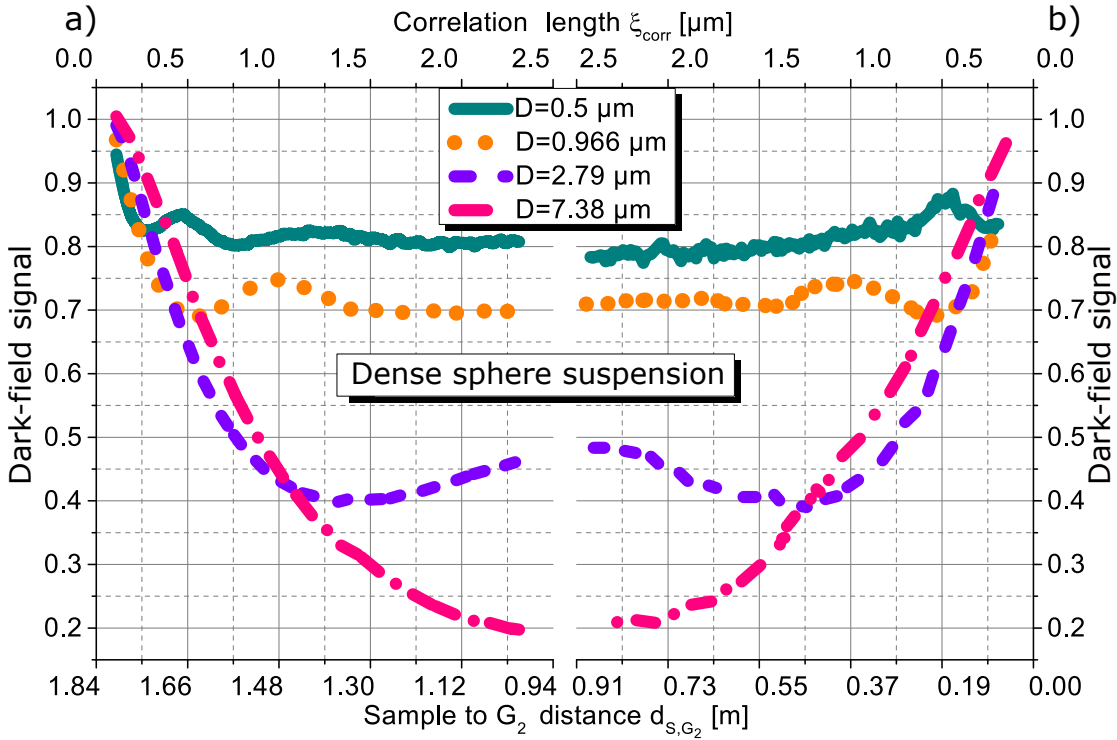


Figure 4.13.: The two graphs show the mean dark-field signal of dense microsphere suspensions acquired between G_0 and G_1 (graph a), or G_1 and G_2 (graph b). The curves of SiO_2 microspheres with diameters of $D = 0.513 \mu\text{m}$ (green solid curve), $D = 0.966 \mu\text{m}$ (orange dotted curve) and $D = 2.79 \mu\text{m}$ (purple dashed curve) show a similar behavior. In these three cases, the signal increases after having reached a minimum at different correlation lengths.

Figure 4.13 shows the average dark-field signal of the four samples. Here, the dark-field signal shows a similar behavior when comparing the data acquired for spheres with diameters of $0.513 \mu\text{m}$, $0.966 \mu\text{m}$ and $2.79 \mu\text{m}$. Each curve reaches a minimum that is followed

by a maximum for the $0.513 \mu\text{m}$ and $0.966 \mu\text{m}$ spheres. The data shows that the dark-field signal of each sample reaches a minimum when the system's correlation length ξ_{corr} approaches the sphere's radius of each sample. These findings are explained in a qualitative manner due to the relation of the dark-field signal to the correlation function $G(x)$. Settled spheres form a random hexagonal lattice as it was already observed in SESANS experiments [74, 77]. Therefore, the correlation function increases when the correlation length approaches the sphere's diameter. The dark-field signal therefore reaches a maximum when $\xi_{corr} = D$, which in this case corresponds to the nearest neighbor distance. A graphical interpretation of the correlation function for this scenario is illustrated in figure 4.14.

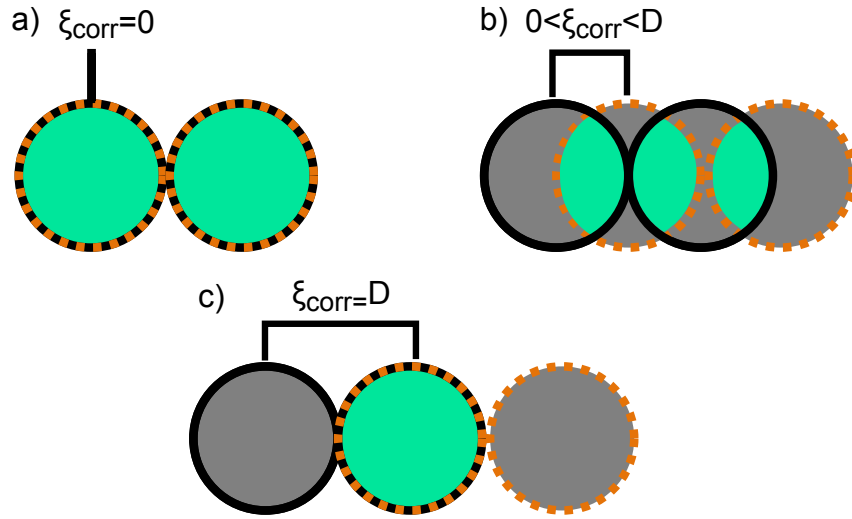


Figure 4.14.: This figure gives a graphical interpretation of the correlation function of a dense sphere suspension. In this case, we consider two pairs of spheres separated by ξ_{corr} . One pair is shown by two black solid circles, while the other pair is shown by the orange dashed circles. **a)** For $\xi_{corr} = 0$ the two pairs perfectly overlap and the shared volume (green region), i.e. the correlation function, is at the maximum. **b)** When ξ_{corr} increases, the shared volume decreases and so does the correlation function. **c)** However, as soon as ξ_{corr} approaches the sphere's diameter D , the shared volume increases again because two spheres are in perfect overlap again. This case shows that the nearest neighbor distance corresponds to the correlation length for which the correlation function has a maximum. For hard spheres this corresponds to the sphere's diameter.

The observed minima appear at correlation lengths of approximately $0.25 \mu\text{m}$ for the $0.513 \mu\text{m}$ spheres, $0.5 \mu\text{m}$ for the $0.966 \mu\text{m}$ spheres and $1.4 \mu\text{m}$ for the $2.79 \mu\text{m}$ spheres. The dark-field signal's maxima appear at correlation lengths of approximately $0.5 \mu\text{m}$ for the $0.513 \mu\text{m}$ spheres and $1 \mu\text{m}$ for the $0.966 \mu\text{m}$ spheres, while no maximum is observed for the $2.79 \mu\text{m}$ spheres. Because the nearest neighbor distance observed for each sample

4. QUANTITATIVE X-RAY DARK-FIELD IMAGING

matches the sphere's diameters, these observations are in very good agreement with the specifications provided by the manufacturer. The dark-field curves of the spheres with a diameter of $D = 7.38 \mu\text{m}$ show a continuous decrease since the relevant correlation lengths are above the maximum correlation length of the interferometer.

The findings of this second experiment allow us to understand the result obtained in the first experiment for the $0.966 \mu\text{m}$, which is shown in figure 4.12. The spheres were not properly suspended in this case but had formed small clusters resulting in the observed minimum.

Our results show that, besides the sphere's form factor (see equation 4.7), the structure factor defined in equation 4.8 also influences the dark-field signal. This structure factor arises from a spatial correlation in the positioning of the scattering objects, i.e. when a short- or long-range order of the microspheres exists in the sample. In contrast to that, the results of the first experiment showed influence by the form factor (see equation 4.7) of a single sphere only.

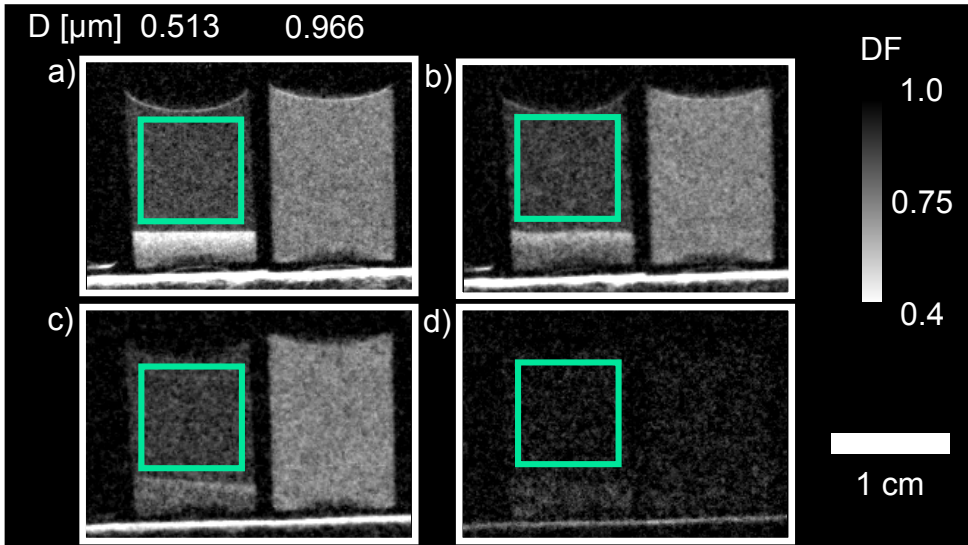


Figure 4.15.: This figure shows three dark-field images a-c) that are registered to the image acquired with the sample close to G_2 shown in image d). After registration, the sample appears with the same dimensions and it is located at the same position in each image. This allows to analyze the dark-field signal of all images pixel-wise. Thus, the correlation function $G(x)$ can be fitted to each pixel according to equations 4.27 and 4.29. The quantitative pixel-wise information can be transformed into a quantitative image.

4.3.3. Quantitative dark-field imaging

Instead of calculating the mean dark-field signal for a large ROI, quantitative information can also be used for quantitative imaging in the case of the $0.513 \mu\text{m}$ spheres. This is achieved by registering all dark-field images acquired at different positions d_{S,G_2} to the dark-field image acquired closest to G_2 . Image registration is only feasible for images acquired between G_1 and G_2 because the sample does not fit the field of view when it is close to G_0 due to large magnification. By registering all images to the one acquired closest to G_2 , an extrapolation of the dark-field signal from one pixel to several pixels in order to enlarge the image is avoided. Consequently, the dark-field signal of several pixels of an image acquired at large magnification is averaged in order to shrink the image. Figure 4.15 shows three dark-field images after being registered to the image acquired with the sample closest to G_2 . The registration was performed based on the attenuation images and the obtained transformation matrix was applied to the dark-field images. A screw therefore was placed next to the samples (see figure 4.9) in order to serve as a fix point for registration.

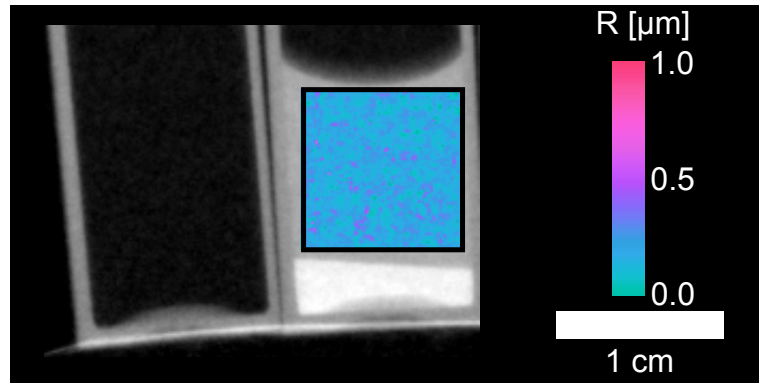


Figure 4.16.: This figure shows a quantitative dark-field image as an overlay to the corresponding transmittance image. The fitting procedure was carried out for a ROI within the suspension containing microspheres with a diameter of $D = 0.513 \mu\text{m}$. The fitted average sphere radius is shown for each pixel within this ROI. The pixel-wise quantitative evaluation gives an average sphere radius of approximately $0.25 \mu\text{m}$ for each pixel indicated by the blue color. This matches the manufacturers specifications giving a sphere diameter of $0.513 \mu\text{m}$.

After registration, the sample appears with the same dimensions and at the same position in each image. Thus, the dark-field signal can be analyzed pixel-wise in order to obtain a dark-field curve for each pixel, which is similar to the curve plotted in figure 4.10. The dark-field curve of each pixel is then fitted according to equations 4.27 and 4.29 to determine the average sphere radius in each pixel. This fitting procedure was carried out for the suspension of microspheres with a diameter of $0.513 \mu\text{m}$. The result is shown for a ROI within the suspension in figure 4.16. The fitted average sphere radius is shown

as an overlay to the transmittance image. An average sphere radius of approximately $0.25 \mu\text{m}$ is obtained in each pixel indicated by the blue color of the ROI. This matches the manufacturers specifications giving a sphere's diameter of $0.513 \mu\text{m}$.

4.4. Summary and discussion

Our results show how quantitative structural information, i.e. the form- and structure factor of a microstructure, can be studied with a laboratory grating-based X-ray dark-field imaging system. Besides the structure size, also short-range ordering of microscopic features in large objects can be studied on a length scale of a few hundreds of nanometers up to a few micrometers. Due to the cosine weighting of the scattered intensity, this information is already obtained in real-space allowing for immediate qualitative interpretation of the data. Measurements are possible either between G_0 and G_1 , or between G_1 and G_2 . Since the structural parameters can be extracted for each single pixel of the detector, the data can easily be represented in a two-dimensional image. The possibility to combine this technique with CT makes it a very interesting tool for microstructural studies on large objects.

However, there are some limitations to this technique. As mentioned above, the highest correlation length of the system is determined by the geometry of the interferometer and the gratings specifications. Increasing the maximum correlation length is not easy since the fractional Talbot distances and grating periods are closely connected to each other as indicated by equations 2.17-2.22 in chapter 2. Using gratings with smaller periods in order to decrease the fractional Talbot distances is one option. By correspondingly increasing the total setup length, higher fractional Talbot orders could be exploited. Thus, it is feasible to increase the maximum correlation length to $5 \mu\text{m}$ for an optimized setup, taking into account the current limitations in grating production as well as a feasible setup length of approximately 2 m. Furthermore, the effect of a polychromatic X-ray spectrum for quantitative measurements has not been studied so far. Equation 4.27 represents the case for monochromatic X-rays. However, our experimental results emphasize that it is feasible to assume that measurements are performed at the mean energy of the X-ray spectrum. Using this mean energy still provides quantitative results as shown by the presented experimental results. Appendix A.2 gives a brief outlook into the polychromatic extension of equation 4.27. In this case, the correlation function $G(x)$ is multiplied by an additional weighting term, which takes the energy dependence of the intensity I_0 and amplitude a_1 into account. Consequently, the measured data is dominated by the energy for which I_0 multiplied by a_1 reaches a maximum. If this corresponds to the design energy of the interferometer, experimental results are obtained that allow quantitative studies as presented. Of course, further experiments have to be carried out to study polychromatic effects in more detail. While our first experiments took a few hours, we were able to decrease the time of data acquisition down to 20 minutes for a full scan.

Therefore the study of slow dynamic processes becomes feasible in the future. This opens new possibilities for example the study of dynamics in colloid systems or materials such as cement where slow changes on the micrometer length scale play an important role.

5. Application of X-ray dark-field imaging in cement and concrete research

In this chapter, the potential of X-ray dark-field imaging for its application in the research of building materials such as cement, mortar and concrete is outlined. After an introduction to cement based materials, first results are presented on the scattering signal's change during the hydration of cement. We further study the influence of environmental parameters such as temperature on our experiments, as well as the influence of aggregates such as limestone grains. Then, a method is presented that transforms the obtained temporal information into images. Regions of inhomogeneous cement hydration are spatially localized based on the acquired images. We extend those methods from two dimensions into three dimensions as the next step by performing a time-resolved tomography scan on a cement sample containing limestone grains of different types. The obtained results are explained in the scope of experiments on water transport in porous materials which are summarized in the beginning of this chapter.

The presented results are published in the following articles, and parts of the following text were adapted from these:

F. Prade et al. "**Observing the setting and hardening of cementitious materials by X-ray dark-field radiography**". In: *Cement and Concrete Research* 74 (2015), pp. 19–25. DOI: 10.1016/j.cemconres.2015.04.003

F. Prade et al. "**Time-resolved X-ray dark-field tomography revealing water transport in a fresh cement sample**". In: *Scientific Reports* 6 (2016). DOI: 10.1038/srep29108

F. Yang et al. "**Dark-field X-ray imaging of unsaturated water transport in porous materials**". In: *Applied Physics Letters* 105.15, 154105 (2014). DOI: 10.1063/1.4898783

5. APPLICATION OF X-RAY DARK-FIELD IMAGING IN CEMENT AND CONCRETE RESEARCH

F. Yang et al. "**X-ray dark-field contrast imaging of water transport during hydration and drying of early age cement-based materials**". In: *In preparation* (2016)

S. Grumbein et al. "**Hydrophobic Properties of Biofilm-Enriched Hybrid Mortar**". In: *Advanced Materials* 28.37 (2016), pp. 8138–8143. DOI: 10.1002/adma.201602123

5.1. Introduction to cement-based building materials

The following background information, as well as the general principles of cement-based materials are described in more detail in references [82–84]. Portland cement is a prominent building material used in civil engineering worldwide. It is the basic material for many mortar- and concrete-mixtures which are widely used to construct buildings, bridges, dams and other important infrastructural elements. Portland cement is a powdery material with particle sizes of usually less than 100 μm . Its major constituents are calcium oxide (CaO) and silicon dioxide (SiO_2) with a mass ratio of typically $\text{CaO}/\text{SiO}_2 > 2$. Furthermore, cement powder contains other oxides such as aluminum oxide, iron oxide and magnesium oxide. Cement is referred to as a hydraulic material which sets and hardens when mixed with a well-defined amount of water. We refer to a mixture of cement powder with water as cement paste in the following text. After mixing, water reacts with the solid cement particles resulting in a change of microstructure which solidifies the cement paste. This process is outlined in more detail at a later point in this chapter to provide a detailed understanding of the presented experimental results. By adding mineral aggregates to cement paste, mortar or concrete is produced. Mortar is obtained when adding aggregates with a maximum grain size of 4 mm to cement paste, while concrete is obtained when aggregates with larger grain size are added. Freshly prepared mixtures are cast into a mold to form components of arbitrary shape. After setting and hardening, the solidified cement paste serves as a stone like matrix that interconnects the aggregate grains in order to form a solid material. Understanding the cement matrix's microstructural evolution, which determines its setting and hardening characteristics, is crucial to further improve the mechanical properties, durability and sustainability of cement-based building materials.

X-ray microscopy techniques are successfully applied at synchrotron facilities to obtain information on the microstructure of cementitious materials and its development during setting and hardening. The importance of such microstructural studies is emphasized in reference [85], which indicates that the microstructural morphology directly determines the setting behavior of cementitious materials. In addition to that, the growth of a hydration layer around single cement particles was visualized using soft X-ray attenuation microscopy [39, 40]. However, X-ray microscopy techniques require a small sample size,

or a special sample preparation in order to resolve microstructural features in cement paste on a sub-micron to micron length scale. Hence, in-situ X-ray microscopy experiments are very challenging.

More established methods such as ultrasound testing are used to study larger cement volumes for their setting and hardening behavior [86–88]. Besides ultrasound testing, other conventional quality control techniques exist like the Vicat-needle test (DIN EN 196-3), the slump test (DIN EN 12350-5), or compaction test (DIN EN 12350-4). Numerous other techniques have been proposed which are partly summarized in reference [89]. New approaches are further described in reference [90]. Furthermore, the relation of the degree of reaction to structural developments is discussed in reference [85] by comparing several testing techniques such as ultrasound and shrinkage measurements. Structural information is also obtained from acoustic emission experiments [91]. Here, the cavitation of small bubbles forming in cement paste during setting is probed. While the mentioned techniques allow for measurements on large sample volumes, their common drawback is the missing of spatial information as they only provide information on the bulk material.

Throughout this chapter we outline the potential of grating-based X-ray dark-field imaging to study the microstructure of large scale objects. Therefore, it is also an ideal tool to study cement-based materials. Besides probing the microstructural evolution during setting and hardening, it also provides spatial information on large samples in the range of several centimeters. This brings the potential to localize regions of differing microstructure within the sample stemming from an inhomogeneous hydration or the use of additives and aggregates.

Besides the importance of early age microstructural developments for the mechanical properties of cement-based materials, microstructural features such as pores and cracks also influence the durability of cement-based materials at later age. Water that penetrates the material through pores and cracks results in unwanted swelling or damage upon freezing [92, 93]. Furthermore, the penetrating water carries ions, which cause cracking due to salt crystal growth or corrosion of metal reinforcement structures embedded in the concrete [94–96]. The capability of a material to adsorb water by capillary suction is usually referred to as water sorptivity. Water sorptivity is usually measured gravimetrically providing precise information on the total mass of adsorbed water, while the penetration depth of the water front is only approximated under error prone assumptions [97, 98]. Methods providing spatially resolved water front measurements are magnetic resonance imaging, neutron and X-ray radiography [99–101]. While magnetic resonance and neutron imaging techniques provide good contrast between the water front and the surrounding porous material, they both suffer from low spatial resolution when compared to X-ray imaging. However, standard attenuation based X-ray imaging suffers from weak X-ray attenuation in water when compared to cement or other building materials. This

5. APPLICATION OF X-RAY DARK-FIELD IMAGING IN CEMENT AND CONCRETE RESEARCH

results in noisy water front profiles. Therefore, contrast agents are typically used to increase X-ray attenuation in water [102, 103]. It is important to mention that contrast agents alter the mechanical properties of water or chemically react with the porous matrix. Therefore, pure water measurements are preferred for in-situ experiments. As pores and cracks on the micrometer length scale result in X-ray scattering, grating-based X-ray dark-field imaging has the potential to study water ingress in porous materials with improved contrast as compared to attenuation based imaging.

In the following chapter we present experimental results which emphasize the potential of grating-based X-ray dark-field imaging to probe microstructural changes in cement-based materials, and to study water transport in porous materials.

5.2. Measurements on water transport in porous materials with dark-field imaging

5.2.1. Materials and methods

Sample preparation

Two different materials were studied. First, we present measurements on mortar samples which were treated at different temperatures before the experiment. The mortar samples had a rectangular shape with dimensions of $10 \times 20 \times 2 \text{ mm}^3$ in x-, y- and z-direction. A detailed description of the sample preparation protocol and mix design is given in the supplementary material of reference [33]. The samples were dried in an oven at 50°C for 48 h after mixing. One sample was further treated at 200°C for 1 h, while another sample was further treated at 120°C for 3 h. The third sample was not treated any further. We refer to those samples as M_{120} , M_{200} and M_U . The index indicates the additional temperature treatment of 120°C , 200°C and the untreated sample, respectively. After the temperature treatment, a 0.07 mm thick polyimide film was pasted to each surface of the sample except for the surface which was later submerged in water during the experiment. This tape reduced water evaporation from the lateral surfaces during the experiment.

The second type of material was a mortar to which biofilm was added during mixing in order to modify its water sorptivity. A detailed protocol of the sample preparation is given in reference [81]. Samples were $10 \times 40 \times 5 \text{ mm}^3$ in x-, y- and z-direction, and they were also wrapped in polyimide film prior the experiment. Furthermore, control mortar samples were measured to compare the results obtained for biofilm-modified mortar samples to those obtained for unmodified mortar samples.

5.2. MEASUREMENTS ON WATER TRANSPORT IN POROUS MATERIALS WITH DARK-FIELD IMAGING

Experimental equipment and parameters

The measurements on temperature treated mortars were performed with the set of gratings shown in table 3.1 in chapter 3. However, a different tube than described in chapter 3 was used. It was a commercially available X-ray tube COMET XRS-160 (MXR-160HP/11), manufactured by COMET AG in Switzerland, using a tungsten target and a focal spot size of 1 mm in diameter. The X-ray tube was operated at an acceleration voltage of 60 kVp and a current of 30 mA. The detector used in this study was an older version (Varian PaxScan®2520D) of the one described in chapter 3, but it had the same physical characteristics. It was operated at a framerate of 10 fps. 7 phase steps were acquired for each reference and sample scan with an exposure time of 0.5 s per step.

The biofilm-modified mortar samples were measured using the experimental equipment as described in chapter 3. Here, the tube was operated at 60 kVp and 100 W resulting in a focal spot size of approximately 100 μm . 7 phase steps were acquired for each reference and sample scan with an exposure time of 1 s per step.

The samples were placed at a distance of $d_{S,G_2} = 60$ cm to the analyzer grating for both experiments.

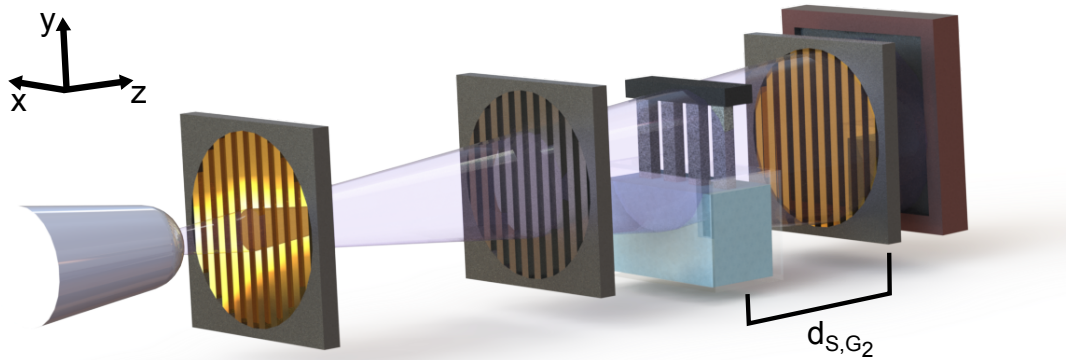


Figure 5.1.: This figure illustrates the general experimental setup to study water sorptivity of porous materials by grating-based X-ray dark-field imaging. To determine a material's water sorptivity, samples (4 gray rectangular prisms) are mounted upside down to a stage (black rectangular prism), and dark-field images are acquired after the sample's tips have been submerged in a water bath. The sample's scattering signal changes due to intrusion of water into pores.

Data acquisition, processing and analysis

A schematic illustration of the experimental setup is shown in figure 5.1. The samples were attached to a sample stage in such a way that the surface which was not covered by

5. APPLICATION OF X-RAY DARK-FIELD IMAGING IN CEMENT AND CONCRETE RESEARCH

the polyimide film faced downwards. A container with de-mineralized water was placed under the samples in the field of view of the imaging system. Twenty reference scans were acquired before the samples were submerged with their bottom surface into the water bath as well as after the experiment.

For the temperature treated mortars, sample scans were then acquired continuously for 13 h. Within the first hour, images were acquired every 10 s while a delay of 120 s was introduced before each acquisition for the remaining 12 h.

For the biofilm-modified mortars, sample scans were acquired continuously for 24 h. Within the first hour, images were acquired every 10 s while a delay of 300 s was introduced before each acquisition for the remaining 23 h.

Sample scans which were acquired during the first half of the experiments were processed with an average of the twenty reference scans acquired before the measurement. Sample scans which were acquired during the second half of the experiments were processed with an average of the twenty reference scans acquired after the measurement. This procedure assured a feasible time difference between sample and reference scan to provide artifact free images.

5.2.2. Measurements on water transport in temperature treated mortar samples

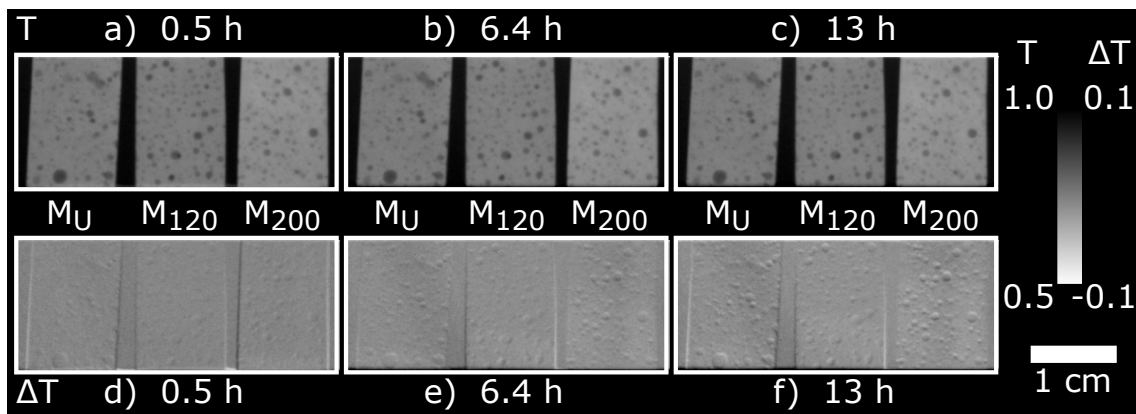


Figure 5.2.: This figure depicts transmittance images of three temperature treated mortar samples acquired 0.5 h (a), 6.4 h (b) and 13 h (c) after submerging the sample into water. Images d-f) show the difference of each image with the image acquired at $t = 0$ h. Intrusion of water is not observed based on the presented images. The increasing contrast of edges and pores in the difference images is related to a slight movement on the samples during the measurement.

5.2. MEASUREMENTS ON WATER TRANSPORT IN POROUS MATERIALS WITH DARK-FIELD IMAGING

Images a-c) in figure 5.2 show transmittance images of the three temperature treated mortar samples M_U , M_{120} and M_{200} . Image a) was acquired 0.5 h after the mortar samples were submerged into the water bath, while images b) and c) were acquired after 6.4 h and 13 h, respectively. The mortar samples have similar transmittance values and morphology since they were prepared according to the same mixing protocol. Different temperature treatment does not affect the transmittance images. Furthermore, no change is observed in images acquired at different points in time. Intrusion of water into the mortar samples therefore is not observable based on transmittance images acquired under the given experimental conditions. In order to further emphasize this finding, images d-f) in figure 5.2 show the difference between images a-c) and the transmittance image acquired at 0 h, i.e. immediately after submerging the sample into water. Here, a slight contrast variation is observed in images acquired at different points in time. Especially the sample's edges and large pores appear with a strong contrast in image e) and f). This is probably related to experimental conditions such as an unstable sample mounting and the focal spot stability of the X-ray tube. No additional signal increase stemming from the intrusion of water is observed. Images a-c) in figure 5.3 show dark-field images of three temperature treated mortar samples M_U , M_{120} and M_{200} corresponding to the transmittance images shown in figure 5.2. Sample M_{200} appears brighter in image a) when compared to samples M_U and M_{120} . This decreased dark-field signal indicates stronger scattering as compared to the other samples. This could be related to the different temperature treatment protocols applied to the three samples.

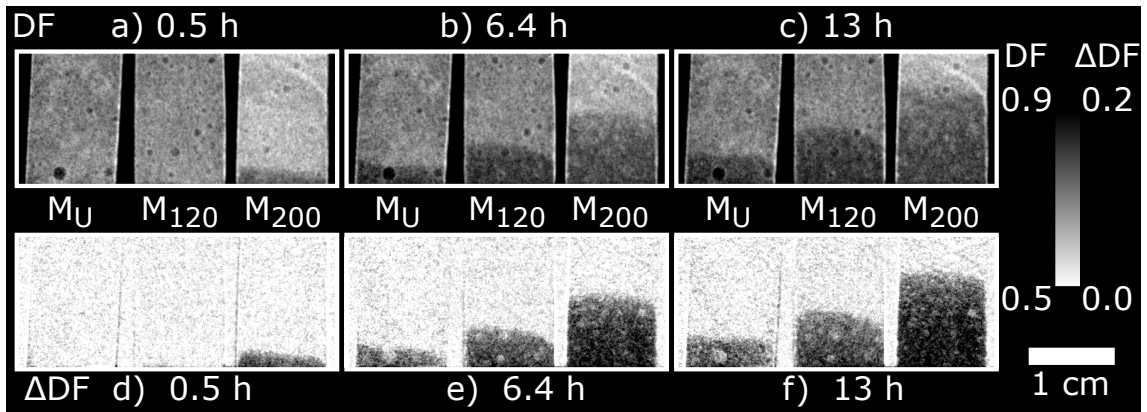


Figure 5.3.: This figure depicts dark-field images of three temperature treated mortar samples acquired 0.5 h (a), 6.4 h (b) and 13 h (c) after submerging the sample into water. Images d), e) and f) show the difference of images a-c) and the dark-field image acquired at $t = 0$ h. The water front penetrating the samples is shown in the dark-field images a-c) as a dark region, i.e. reduced scattering, at the bottom of each sample. This is even more pronounced in the difference images d-f). Sample M_{200} has the strongest sorptivity when compared to the samples M_{120} and M_U . Here, the dark region corresponding to reduced scattering grows faster as compared to the other samples.

5. APPLICATION OF X-RAY DARK-FIELD IMAGING IN CEMENT AND CONCRETE RESEARCH

In addition, a dark region shows up in image a) at the bottom of sample M_{200} indicating that scattering is reduced in this area. Samples M_U and M_{120} do not show any regions of reduced scattering in image a) except for some large pores. This region of reduced scattering in sample M_{200} grows towards the sample's top with time in images b) and c). This observation indicates the intrusion of water into the sample due to capillary forces. Furthermore, similar regions are observed for samples M_U and M_{120} after 6.4 h. These regions of reduced scattering have reached different heights in all three samples after 13 h. This indicates that temperature treatment influences the water sorptivity of mortar. These findings are further emphasized by images d-f) in figure 5.3, which show the difference of images a-c) with the dark-field image acquired at 0 h, i.e. immediately after submerging the samples into water. Here, the contrast between wet and dry regions is enhanced. This allows to determine the movement of the waterfront penetrating the sample, and to spatially analyze its vertical position by a simple threshold-based segmentation of wet and dry mortar. This procedure is further explained and supported by computational results in reference [33].

Due to improved contrast between wet and dry regions within mortar samples provided by dark-field images, we restrict the following consideration to dark-field images only.

5.2.3. Measurements on water transport in biofilm-modified mortar samples

Figure 5.4 shows dark-field images of two biofilm-modified mortar samples and two unmodified mortar samples acquired 2 min. (a), 10 min. (b) and 50 min. (c) after submerging the samples into water. A region of reduced scattering is observed after 2 min. in the unmodified samples. Over time, the dark region rises towards the top in both unmodified mortar samples. In contrast to that, the biofilm-modified mortar samples do not show any change within 50 min., and also during the remaining 23 h of the experiment no change was observed. This is further emphasized by images d-f) in figure 5.4, which show the difference of images a-c) and the dark-field image acquired immediately after submerging the samples into water. While the growing regions of reduced scattering in the control mortar samples appear at higher contrast compared to images a-c), no change is observed in the biofilm-modified mortar samples.

5.2.4. Discussion

Mortars, in general, have an open pore system with pore sizes in the sub-micrometer to millimeter length scale. Mortar adsorbs water due to capillary forces caused by its pore system. Once submerged in water, the mortar samples therefore take up water. Because of the large difference in electron density between air-filled pores and the solid mortar material, the pores scatter X-rays creating a strong signal in dark-field images. As water

5.2. MEASUREMENTS ON WATER TRANSPORT IN POROUS MATERIALS WITH DARK-FIELD IMAGING

permeates the pores, the mortar's scattering strength is reduced because the difference in electron density is reduced. This explains the dark regions of reduced scattering rising from bottom to top in the temperature treated mortar samples and the unmodified mortar samples.

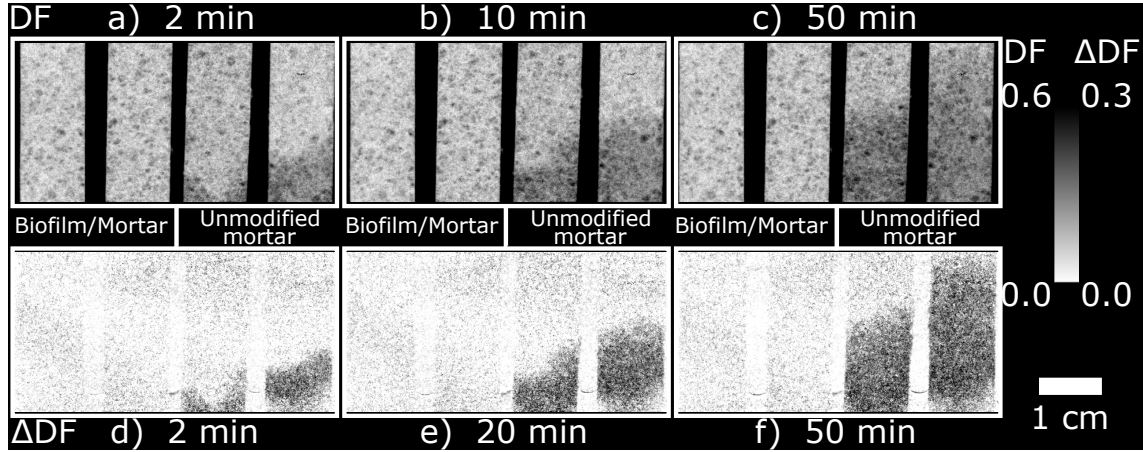


Figure 5.4.: This figure depicts dark-field images of two unmodified and two biofilm-modified mortar samples acquired 2 min. (a), 10 min. (b) and 50 min. (c) after submerging the sample into water. Images d-f) show the difference of images a-c) and the dark-field image acquired at $t = 0$ h. While water penetrates the unmodified mortar samples, the biofilm-modified mortar samples do not show any signs of water intrusion. The decreasing scattering signal due to water intrusion into the unmodified samples is even more pronounced in the difference images.

Temperature treatment of mortars is known to induce micro-cracking and of course dehydration. Therefore, the three mortar samples M_U , M_{120} and M_{200} are expected to show different sorptivity properties due to different treatment protocols. The amount of micro-cracks induced in mortar increases with increasing treatment temperature. As these cracks contribute to water sorptivity due to capillary forces, water penetrates the samples faster the higher the treatment temperature. Consequently, sample M_{120} adsorbs water faster when compared to sample M_U . This is illustrated by the water front, which reaches different heights in the three samples during the same time period. The contribution of water to the sample's X-ray attenuation is very small when compared to the solid mortar material. Therefore, water intrusions is not observed in the transmittance images in figure 5.2.

Water intrusion has unwanted effects in mortar materials such as damage upon freezing [93]. Creating a hydrophobic surface on the open pore system of mortar materials is one option to reduce water sorptivity of mortars [81]. Our measurements on biofilm-modified mortar samples emphasize this effect. As biofilm is added to the mortar during mixing, it creates a hydrophobic surface which counteracts the capillary forces, and therefore reduces

5. APPLICATION OF X-RAY DARK-FIELD IMAGING IN CEMENT AND CONCRETE RESEARCH

water intrusion. Therefore, dark-field images of the biofilm-modified samples remain unchanged. In contrast to that, the unmodified mortar samples show water adsorption as is typical for mortar.

The presented results emphasize that grating-based X-ray dark-field imaging is capable to study water transport in porous materials. Compared to attenuation-based X-ray imaging methods, the intrusion of water into pores on the micrometer length scale generates a strong change of the dark-field signal. Dark-field measurements therefore do not require any contrast agents. This is beneficial for in-situ experiments.

5.3. Time evolution of the dark-field signal of fresh cement paste

In this section, we present measurements on fresh cement paste and the evolution of its scattering signal within the first 2 days after sample preparation.

5.3.1. Materials and methods

Sample preparation

Table 5.1.: Chemical composition of the Portland cement CEM I 42.5 R used in this work in percent by weight. The data was originally published in reference [104].

Compound	<i>SiO₂</i>	<i>Al₂O₃</i>	<i>Fe₂O₃</i>	<i>FeO</i>	<i>CaO</i>	<i>MgO</i>
Mass fraction [% by weight]	20.9	4.0	2.5	n.a.	63.9	1.4
Compound	<i>TiO₂</i>	<i>SO₃</i>	<i>K₂O</i>	<i>Na₂O</i>	<i>H₂O</i>	
Mass fraction [% by weight]	0.2	3.2	1.6	0.3	2.3	

In this study a commercially available rapid curing Portland cement (CEM I 42.5 R) was used. The particle size distribution of this cement is shown in figure 5.5, while its chemical composition is presented in table 5.1. 3.9 g of distilled and deionized water were manually mixed with 12.5 g of cement powder for one minute at room temperature. The resulting water to cement mass-ratio (w/c-ratio) was $w/c = 0.312$. After mixing, the fresh cement paste was filled into the chambers of the sample holder shown in figure 5.6. The sample holder was made of plastic containing four sample chambers and a plastic lid. The dimensions of each sample chamber were 50x10x5 mm³ in y-, x- and z-direction. A proper sealing of the chambers was ensured by pasting double-sided adhesive tape on the plastic bars separating the chambers. After filling, the open side of the sample holder was covered with the plastic lid, which was fixed to the sample holder with four screws. Finally, the opening at the top of the sample holder was sealed with grease in order to

5.3. TIME EVOLUTION OF THE DARK-FIELD SIGNAL OF FRESH CEMENT PASTE

prevent water evaporation from the cement-air interface during the measurements. The sample was placed between the phase and analyzer grating at a distance of $d_{S,G_2} = 61$ cm to the analyzer grating. A photograph of the sample holder, the plastic lid and some cement samples is show in appendix B in figure B.2.

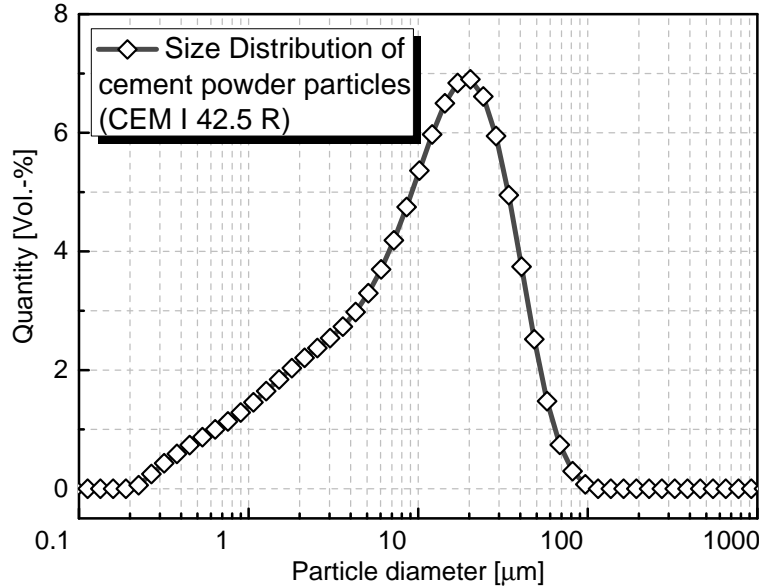


Figure 5.5.: This figure shows the particle size distribution of the Portland cement CEM I 42.5 R used for this study. Particles are smaller than $100 \mu\text{m}$. The largest volume fraction has a diameter of $20 \mu\text{m}$ (see the curve’s maximum). Therefore, fresh cement paste is expected to give a strong scattering signal in grating-based X-ray dark-field imaging.

Experimental equipment and parameters

The experiments were carried out with the set of gratings given in table 3.1 in chapter 3. A commercially available X-ray tube COMET XRS-160 (MXR-160HP/11), manufactured by COMET AG, Switzerland, was used in this study. It uses a tungsten target and a focal spot size of 0.4 mm. The X-ray tube was operated at an acceleration voltage of 60 kVp and a current of 13.3 mA. The detector used in this study, was a Varian PaxScan $\text{\textcircled{R}}$ 2520D. It is an old version of the one described in chapter 3, but it has the same physical characteristics. It was operated at a framerate of 10 fps.

Data acquisition, processing and analysis

Reference scans and sample scans were acquired for 48 h after sample preparation. Each scan consisted of seven equidistant phase steps with an exposure time of 10 s per step. Dark-field and transmittance images were obtained by processing each sample scan with

5. APPLICATION OF X-RAY DARK-FIELD IMAGING IN CEMENT AND CONCRETE RESEARCH

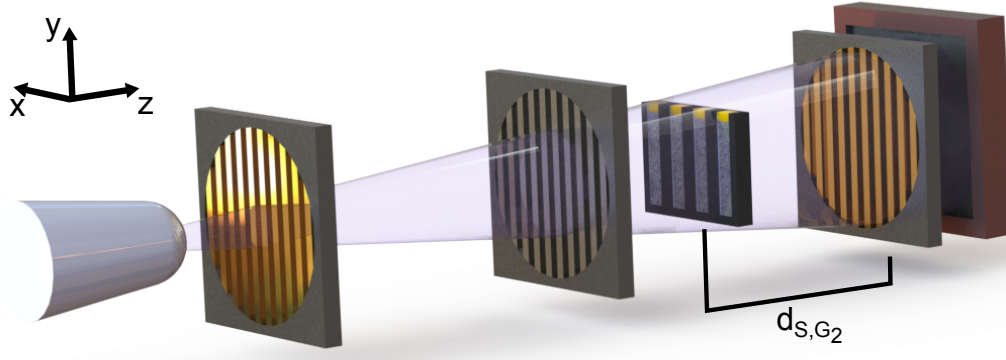


Figure 5.6.: This figure illustrates experimental setup for time-resolved dark-field radiography on fresh cement paste. The sample holder contains four chambers with dimensions of 10, 5 and 50 mm in x-, z- and y-direction. The fresh cement paste is filled into these chambers and sealed with grease at the top to reduce water evaporation. The open side is covered by a plastic lid during the experiments. It is screwed to the sample holder after the samples have been filled into the chambers. To monitor the progress of hydration in the cement paste, images are acquired for two days after sample preparation.

the previously recorded reference scan. For a quantitative signal analysis of the transmittance and dark-field images, a transmittance threshold segmentation was performed to separate cement from large air voids embedded in the samples. A binary mask was calculated based on the transmittance images, which labeled the cement material and air voids with 0 and 1, respectively. The histogram of transmittance values was fitted by a Gaussian function to obtain the cement's mean transmittance value and its standard deviation. Every pixel with a transmittance value within a two-sigma interval around the cement's mean transmittance value was labeled as cement. A mean transmittance and dark-field signal of a ROI covering the whole sample was calculated based on this mask. We only considered pixels which were labeled as cement in the binary mask. Finally, the negative logarithm of the mean transmittance and dark-field signal was calculated and divided by the sample thickness to obtain the linear attenuation coefficient μ and the scattering coefficient ε . The measurement was repeated three times, and the results were averaged to validate the experiment's reproducibility.

5.3.2. Experimental results

Figure 5.7 shows transmittance images of one exemplary measurement. The sample's transmittance signal does not change during the first 30 h after mixing the cement powder with water. Some large voids are embedded in the cement sample indicated by dark regions. The fact that the transmittance does not change is further illustrated in figure 5.9. The mean attenuation coefficient μ for each sample was calculated based on the ROI

5.3. TIME EVOLUTION OF THE DARK-FIELD SIGNAL OF FRESH CEMENT PASTE

marked by the orange rectangles in figure 5.7. It was calculated according to the procedure outlined in the previous materials and methods section.

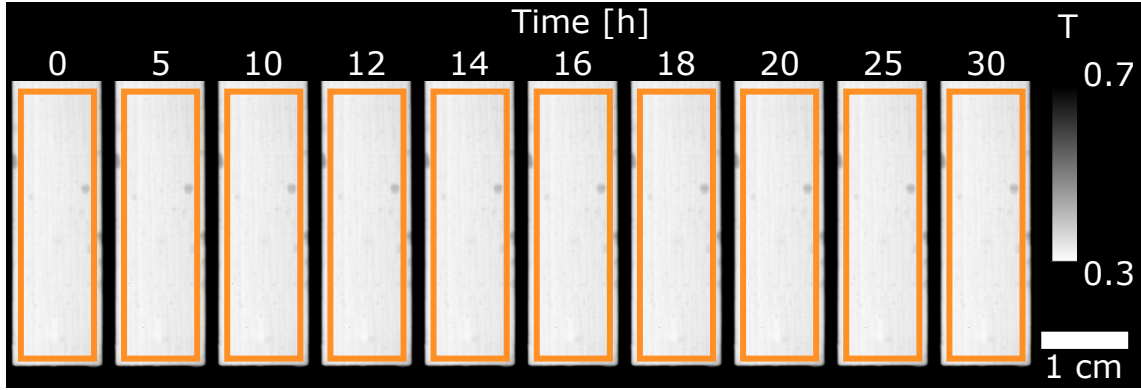


Figure 5.7.: This figure illustrates transmittance images of an exemplary fresh cement paste sample for the first 30 h after sample preparation. The cement’s transmittance does not change indicating that its attenuation properties remain constant. The colored rectangles mark the ROI used to calculate the average attenuation signal, which is plotted in figure 5.9.

The resulting attenuation coefficients of the three experiments were then averaged, and the standard deviation was calculated. Figure 5.9 shows the mean attenuation coefficient plotted against time. It is represented by the dotted orange curve, while its standard deviation is shown by the brown error band. The curve remains constant within a time period of 48 h. This progression agrees with the images presented in figure 5.7.

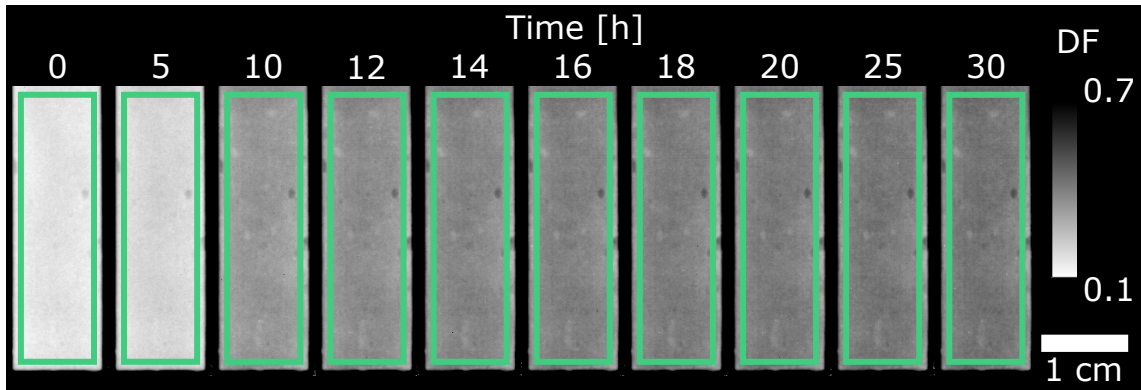


Figure 5.8.: This figure illustrates dark-field images of an exemplary fresh cement paste sample for the first 30 h after sample preparation. The cement’s dark-field signal strongly changes 5 h after preparation. As the sample appears darker with increasing time, its scattering strength decreases. The colored rectangles mark the ROI used to calculate the average scattering signal, which is plotted in figure 5.9.

5. APPLICATION OF X-RAY DARK-FIELD IMAGING IN CEMENT AND CONCRETE RESEARCH

Figure 5.8 shows dark-field images corresponding to the transmittance images in figure 5.7. In contrast to the transmittance signal, the dark-field signal of the cement sample strongly increases 5 h after sample preparation. Therefore, the cement appears darker with increasing time. This signal change is further emphasized by figure 5.9 which shows the mean scattering coefficient of three measurements (green dashed curve). The mean scattering coefficient of each sample was calculated based on the ROI marked by the green rectangles in figure 5.8.

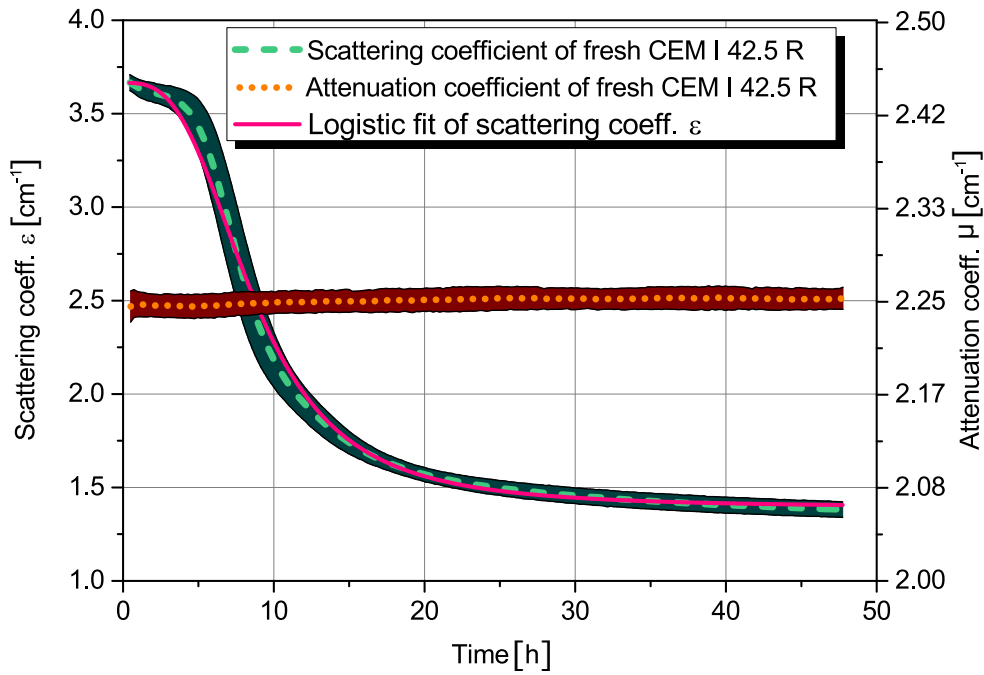


Figure 5.9.: This graph shows the time evolution of the attenuation and scattering coefficient of fresh cement paste for 48 h after sample preparation. The green dashed curve represents the scattering coefficient. It was averaged over three single measurements with the same type of cement prepared according to the same protocol. The orange dotted curve represents the corresponding attenuation coefficient. The error bands represent the standard deviation of the three single measurements. While the attenuation coefficient of cement paste does not change during the experiment, the scattering coefficient strongly decreases after 5 h and follows a logistic shape. Additionally, a logistic fit was therefore performed on the scattering coefficient according to equation 5.1. It is represented by the pink curve.

After 5 h, the mean scattering coefficient of cement strongly decreases, and it levels out after 20 h at a value of approximately $\epsilon = 1.4 \text{ cm}^{-1}$. Its shape resembles a logistic curve as given by equation 5.1.

$$\varepsilon(t) = \varepsilon_{\infty} + \frac{\varepsilon_0 - \varepsilon_{\infty}}{1 + \left(\frac{t}{t_{1/2}}\right)^g} \quad . \quad (5.1)$$

The scattering coefficient starts at an initial value of ε_0 and reaches a constant level of ε_{∞} for $t \rightarrow \infty$. The difference $\varepsilon_0 - \varepsilon_{\infty}$ gives the total decrease in scattering and is therefore referred to as the amplitude A . While the parameter $t_{1/2}$ resembles the time after which the signal has decreased by half of the amplitude, the parameter g is proportional to the curve's maximum gradient at this point. We will therefore refer to the parameter g as the maximum gradient of the logistic function. A fit to the scattering coefficient according to such a logistic function is shown by the pink curve in figure 5.9. This logistic fit follows the progress of the scattering coefficient nicely within the shown error bands. This emphasizes that the evolution of the scattering signal of cement paste follows a logistic model.

5.3.3. Discussion

Before putting the presented results into context with setting and hardening processes of cement, we briefly describe the microstructural evolution in fresh cement paste. More details on these processes are given by references [82–84].

Cement hydration

The reactions of cement powder with water are usually divided into four stages. First, highly soluble constituents of the cement particles dissolve in water immediately after mixing. This process lasts for less than a minute. The dissolved material forms first hydration products which settle on the surface of the cement particles. This layer creates a barrier between the cement particles and the free water preventing any further reaction during the next few hours. This second period of low reactivity is called induction period. During the third period, the rapid reaction period, cement particles further dissolve and react with free water forming hydration products, which nucleate and grow as a layer around the cement particles. The most important compounds created during this period are tri- and dicalcium silicates, which are hydrated by water and form a gel phase of calcium silicate hydrate and calcium hydroxide crystals. The reaction rate reaches a maximum between 10 – 20 h after mixing. As the hydration layer grows around the cement particles, it limits the diffusive transport of dissolved material into the space occupied by free water. This initiates the diffusion-limited reaction period during which reactions decelerate. Hydration of the remaining cement particle cores further continues over several weeks, while morphological changes of cement paste are only taking place on the nanometer length scale. A schematic representation of cement paste's microstructure for different points in time is shown in figure 5.10.

5. APPLICATION OF X-RAY DARK-FIELD IMAGING IN CEMENT AND CONCRETE RESEARCH

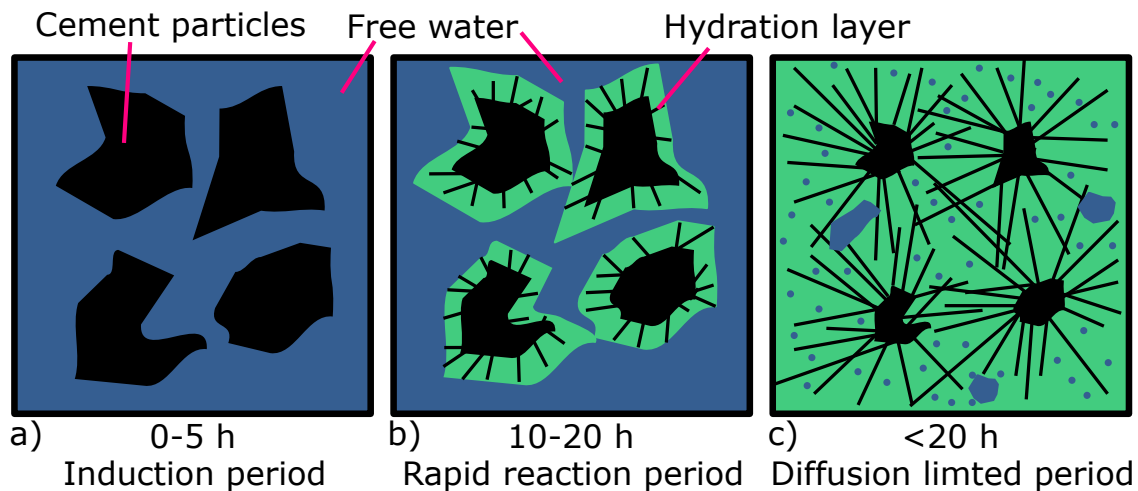


Figure 5.10.: This figure shows a schematic illustration of the microstructural evolution in cement paste. **a)** After mixing, the cement particles are suspended in water. During the induction period reactivity is low. It lasts for approximately 5 h after mixing. **b)** Approximately 10 h after mixing, the reaction rates increase, and a layer of hydration products grows around the particles. This rapid reaction period approximately lasts 10 h. **c)** When the hydration layer reaches a certain thickness, it limits the diffusive transport of dissolved material. Therefore, reactions are decelerated in the diffusion limited period.

As the hydration layer grows, primarily in form of calcium silicate hydrates, it interconnects the solid cement particles and therefore results in setting and hardening of cement paste. Pores, previously saturated with water are now filled with hydration products. Looking at a length scale of several micrometers, cement therefore appears more homogeneous after hydration.

Interpretation of the experimental results

Based on this basic knowledge about the hydration reactions in cement paste, we now move on to interpret our experimental results. X-ray attenuation depends on the X-ray energy and the atomic elements present in the sample. The exact chemical composition plays a minor role and is only observable in experiments looking at the fine structure of X-ray absorption spectra [43]. Reactions taking place within cement paste result in morphological changes on the sub-micron to micrometer length scale. Because the spatial resolution of our imaging system is about $100 \mu\text{m}$, it does not allow to spatially resolve these microstructural changes. Therefore, these reactions do not influence the attenuation signal of cement paste.

In contrast to that, the dark-field signal is based on X-ray scattering and therefore is sensitive to deviations of the electron density on a length scale which is smaller than the

5.3. TIME EVOLUTION OF THE DARK-FIELD SIGNAL OF FRESH CEMENT PASTE

spatial resolution of the imaging system. Initially, fresh cement paste is a suspension of solid cement particles in water. As particle sizes are usually well below $100\ \mu\text{m}$ (see figure 5.5), a strong scattering signal is observed for cement because of the electron density difference between the solid particles and free water. During hydration, the particles dissolve and therefore shrink, which results in a decrease of the scattering signal. Furthermore, the electron density difference between cement particles and their surrounding decreases as a result of the hydration layer which grows around the cement particles. This reduction in scattering contrast results in a further decrease of the scattering signal. The presented data clearly shows that morphological changes within the induction period are small during the first hours, and scattering is therefore almost constant during this period. The microstructure of cement then changes rapidly during the rapid reaction period, and scattering consequently decreases as the cement becomes more and more homogenous. Finally, the reduction of scattering slows down as microstructural changes decelerate in the diffusion-limited reaction period.

The temporal agreement of the scattering signal's evolution and the four reaction periods is further supported by the evolution of the speed of sound within fresh cement paste, which progresses similar to the scattering signal as it follows a logistic shape. A comparison of ultra-sound and scattering data is presented in reference [78]. The logistic fit was inspired by the application of logistic functions to ultrasound data presented in reference [87].

The logistic function's parameters are related to physical quantities describing the state of reaction at each point in time. The initial particle size distribution, chemical composition, w/c-ratio and the size distribution of embedded pores determines the parameter ε_0 . The parameters g and $t_{1/2}$ provide information on reaction rates within the cement paste. Finally, ε_∞ and the amplitude of the scattering coefficient's logistic decline are related to the degree of hydration. This parameter describes how much free water is consumed by hydration products at each point in time. However, quantification of these parameters is not straight forward. Cement is a complex material, and different chemical phases contribute to the scattering. Therefore, much more experimental work is necessary to study the contribution of each quantity to the scattering signal.

Our results show that qualitative information on the dynamics of cement hydration are provided by grating-based X-ray dark-field imaging. Furthermore, the data is spatially resolved which has some advantages when compared to standard testing techniques.

5.4. Influence of temperature on the dark-field signal of fresh cement paste

Chemical reactions taking place during cement hydration are influenced by environmental parameters such as the temperature. In the following we present experimental results emphasizing that this temperature dependence can be studied by grating-based X-ray dark-field imaging.

5.4.1. Materials and methods

Sample preparation

The same type of cement as outlined in the previous section was used for this experiment, and samples were prepared accordingly. A Peltier-element heated one chamber of the sample holder above room temperature, while one chamber was cooled below room temperature. Therefore, aluminum parts were attached to both sides of the Peltier-element and inserted into two chambers. The chamber in between remained at room temperature. The sample holder was placed at a distance of $d_{S,G_2} = 70$ cm from the analyzer grating.

Experimental equipment and parameters

The experiments were carried out with the same equipment and parameters that were already used in the previous experiment.

Data acquisition, processing and analysis

Data was acquired, processed and analyzed as described for the previous experiment. However, due to the temperature gradient in each sample, four different ROIs were used for quantitative signal analysis covering the sample from top to bottom.

5.4.2. Experimental results

Figure 5.11 shows dark-field images acquired 0.5 h (a) and 10 h (b) after mixing. The fresh cement paste samples were cooled (left), heated (right) or remained at room temperature (middle) during the experiment. The black rectangles shown at the top of the cooled and heated sample are part of the temperature controlling device. While all three samples initially show a homogenous dark-field signal in image a), a gradient is observed in the heated and cooled samples 10 h after preparation. The sample which remained at room temperature still shows a homogenous dark-field signal after 10 h. The cooled sample appears brighter at the top in image b), while its bottom is darker. This indicates that scattering is higher at the top of the cooled sample as compared to the bottom after 10 h. This observation is inverted for the heated sample. Here, the sample is darker at the top,

5.4. INFLUENCE OF TEMPERATURE ON THE DARK-FIELD SIGNAL OF FRESH CEMENT PASTE

while its bottom appears brighter meaning that scattering in this case is lower at the top as compared to the bottom. This finding is further emphasized by the curves presented in figure 5.12. It shows the scattering coefficients which were averaged over the ROIs marked by the colored rectangles shown in figure 5.11. The evolution of the scattering coefficients of each ROI agrees well with the observations in the dark-field images. While the scattering coefficient decreases slowly in the top ROI of the cooled sample (see the green curve in graph b)), it decreases faster for the lower ROIs. In contrast to that, the four ROIs of the untreated sample do not deviate from each other as the scattering coefficient displays the same progression for each ROI. In the case of the heated sample, the top ROI's scattering signal decreases faster as compared to the lower ROIs.

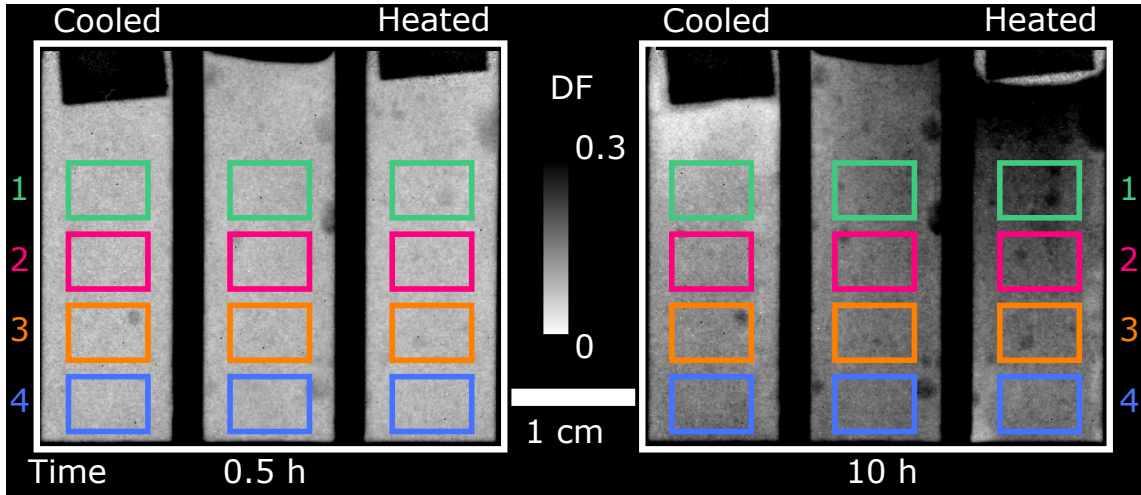


Figure 5.11.: This figure depicts dark-field images of three cement samples acquired 0.5 h and 10 h after sample preparation. The sample on the left was cooled, while the sample on the right was heated during the experiment. The middle sample remained at room temperature. A Peltier-element was used for heating and cooling. The aluminum parts attached to the Peltier-element correspond to the black rectangular features at the top of the heated and cooled sample. A gradient in the dark-field signal is observed after 10 h in the heated and cooled sample. It runs from top to bottom in each sample, while it is inverted for the heated and cooled sample. The colored rectangles mark ROIs over which the average scattering coefficient was calculated. The resulting graphs are shown in figure 5.12.

5.4.3. Discussion

The hydration reactions in fresh cement paste are always influenced by environmental conditions such as the temperature. As chemical reactions are slowed down at lower temperatures, microstructural changes within the cement paste are decelerated accordingly.

5. APPLICATION OF X-RAY DARK-FIELD IMAGING IN CEMENT AND CONCRETE RESEARCH

Therefore, the scattering coefficient at the top of the cooled sample decreases slower as compared to the other ROIs. In contrast to that, higher temperatures speed up hydration reactions, and microstructural changes are accelerated accordingly. Therefore, the scattering coefficient in the top ROI of the heated sample decreases much faster as compared to the other ROIs. Our results are in good agreement with expectations based on those thermodynamic considerations. Furthermore, this experiment emphasizes that local variations of the hydration dynamics and inhomogeneities in fresh cement paste can be spatially resolved by grating-based X-ray dark-field imaging.

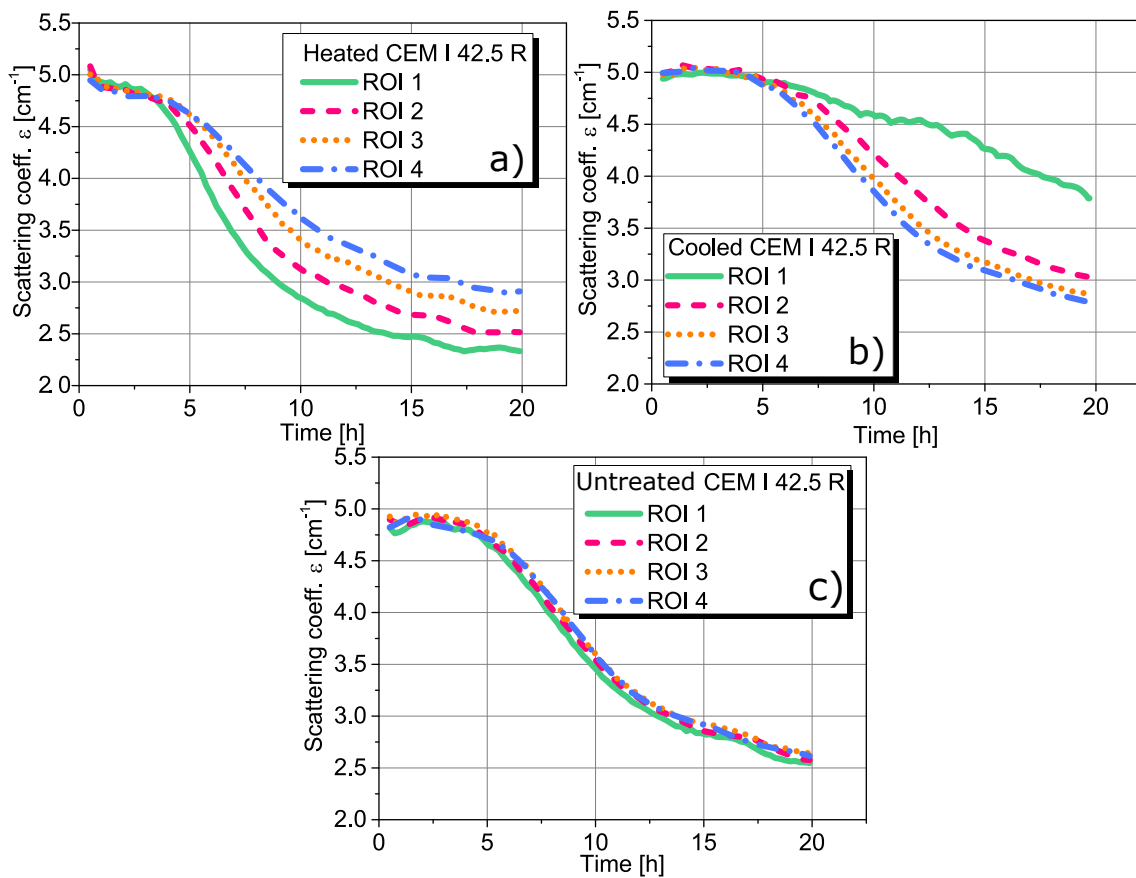


Figure 5.12.: The three graphs show the averaged scattering coefficient of the four ROIs marked in figure 5.11 for the cooled (a), untreated (b) and heated sample (c). All ROIs show a similar decrease of the scattering coefficient for the untreated sample. In contrast to that, the top ROI of the cooled sample (green solid curve) shows a much slower decrease as compared to the other ROIs. The heated sample shows the opposite behavior. The scattering coefficient of the ROI at the top (green solid curve) decreases faster as compared to the other three ROIs.

5.5. Influence of limestone grains on the dark-field signal of fresh cement paste

Cement-based building materials usually include additives such as mineral aggregates. The next experimental results illustrate the influence of such aggregates on the dark-field signal of fresh cement paste.

5.5.1. Materials and methods

Sample preparation

The samples were prepared according to the protocol used in the two previous experiments. Additionally, single limestone grains of three different types (labeled as $K1$, $K2$ and $K3$ in the following) were embedded in the fresh cement paste. One measurement was performed to compare the limestone types $K1$ and $K3$. Here, the samples were placed between the phase and analyzer grating at distance $d_{S,G_2} = 61$ cm to the analyzer grating. A second measurement was conducted to compare the limestone types $K1$ and $K2$. Here, the samples were placed between the phase and analyzer grating at distance $d_{S,G_2} = 75$ cm to the analyzer grating.

Experimental equipment and parameters

The experiments were carried out with the same equipment and parameters used in the previous two experiments.

Data acquisition, processing and analysis

Data was acquired, processed and analysis as described above. For each sample two ROIs were used for quantitative signal analysis. One ROI covered the cement paste, while the other ROI covered a limestone grain. Furthermore, we carried out a pixel wise analysis based on a logistic fit of the scattering signal's evolution. This procedure is described in more detail in the following text.

5.5.2. Experimental results

Figure 5.13 shows the results obtained when adding limestone grains of two different types ($K1$ and $K3$) to fresh cement paste. The two images show the dark-field signal of two cement samples 0.5 h and 33 h after sample preparation. The limestone grains are observed as dark regions within the cement paste 0.5 h after preparation indicating that scattering is reduced by the limestone grains. After 33 h, however, the limestone grain of type $K1$ displays a change in contrast as it appears brighter than the cement paste. The contrast of limestone grains of type $K3$ and the cement paste remains unchanged

5. APPLICATION OF X-RAY DARK-FIELD IMAGING IN CEMENT AND CONCRETE RESEARCH

after 33 h. This finding is supported by the graphs at the bottom of figure 5.13. They were obtained by averaging the scattering coefficient over the ROIs marked by the colored rectangles in the dark-field images. The scattering coefficient of the cement paste follows a logistic decline in both samples (see dashed curves). The ROI covering the limestone grain of type *K3* shows a similar logistic decline as shown by the solid curve in graph b).

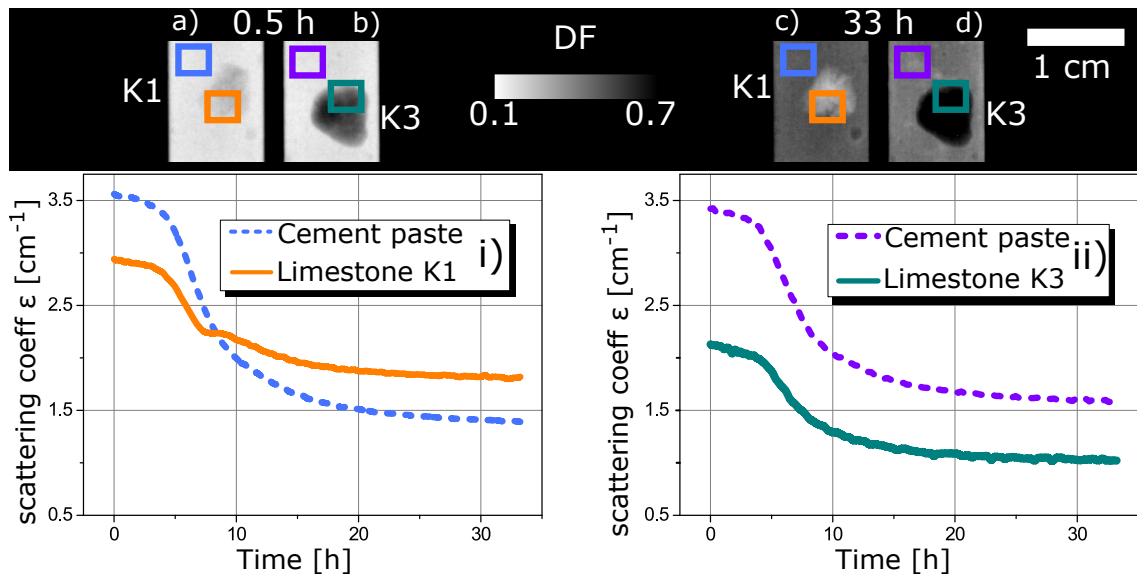


Figure 5.13.: This figure illustrates the influence of limestone grains on the scattering signal of fresh cement paste. The dark-field images at the top show two cement samples containing limestone grains of type *K1* in images a) and c), and of type *K3* in images b) and d). Images a) and b) were acquired 0.5 h while images c) and d) 33 h after sample preparation. The contrast between the limestone grain of type *K1* and the cement paste is inverted after 33 h. On the bottom, the scattering coefficients of the marked ROIs for the sample containing the limestone grain of type *K1* are shown in graph i) and type *K3* in graph ii). A step is observed at 7-9 h in the curve of the limestone grain of type *K1* (orange solid curve in graph i), while the curves of the cement paste and limestone grain of type *K3* follow a logistic shape.

However, the scattering coefficient is strongly reduced as compared to the pure cement paste. In contrast to that, the ROI covering the *K1* limestone grain shows a deformation in its logistic decline as shown by the solid curve in graph a). Here, a step is observed at 7–9 h before the curves of the cement paste and the grain intersect. This crossing agrees with the change in contrast observed in the dark-field images of the limestone grain of type *K1*.

5.5. INFLUENCE OF LIMESTONE GRAINS ON THE DARK-FIELD SIGNAL OF FRESH CEMENT PASTE

Pixel wise fitting of scattering curves

To further study this behavior in more detail, we developed a pixel-wise fitting procedure to improve the visualization of the observed effect. This procedure is illustrated in figure 5.14. The scattering coefficient is calculated in each pixel and each dark-field image acquired during the experiment. Thus, the scattering coefficient's time evolution is obtained for each pixel, and a logistic fit according to equation 5.1 can be performed on this data. As a result, four fitting parameters ε_0 , ε_∞ , $t_{1/2}$ and g are obtained in each pixel. Images are created based on the fitting parameters providing complementary information.

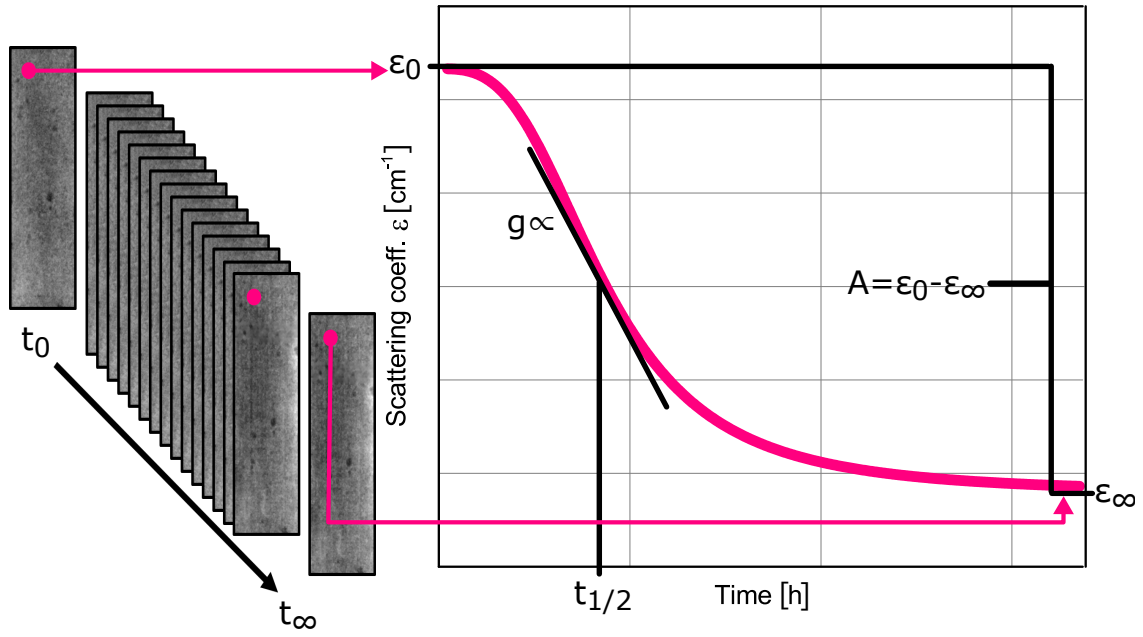


Figure 5.14.: This figure illustrates how each pixel of a time series of dark-field images is fitted by a logistic function. A time series of dark-field images of fresh cement paste is shown on the left side of this figure. The red dot indicates how the scattering coefficient's time evolution is evaluated in each pixel to obtain a logistic fit as shown on the right hand side of this figure. The fitting parameters ε_0 , ε_∞ , $t_{1/2}$ and g , which are obtained for each pixel are used to create further images.

Figure 5.15 shows the images obtained by the described pixel-wise fitting procedure based on the data presented in figure 5.13. In addition to the four fitting parameters we calculated images for the logistic curve's amplitude $A = \varepsilon_0 - \varepsilon_\infty$ and the normalized amplitude $A_{norm.} = A/\varepsilon_0$. The resulting images allow a clear distinction between the limestone grain of type *K1* and *K3*. The image representations of parameters ε_0 and ε_∞ resemble the dark-field images shown in figure 5.13 because they represent the initial and final scattering coefficient of the sample. The amplitude images show that scattering coefficients decrease less in the vicinity of the limestone grains. However, this corresponds to the

5. APPLICATION OF X-RAY DARK-FIELD IMAGING IN CEMENT AND CONCRETE RESEARCH

initial reduction of the scattering coefficient for grain of type *K3*. Therefore, this grain is not observed in the image representing the normalized amplitude. In contrast to that, the grain of type *K1* is observed in the normalized amplitude image. This means that for grains of type *K3* the decrease in scattering is proportional to the initial scattering coefficients. For grains of type *K1* this proportionality is broken. Furthermore, the grain of type *K1* is also observable in the image representation of parameters g and $t_{1/2}$, while the *K3* grain is not observed in both images.

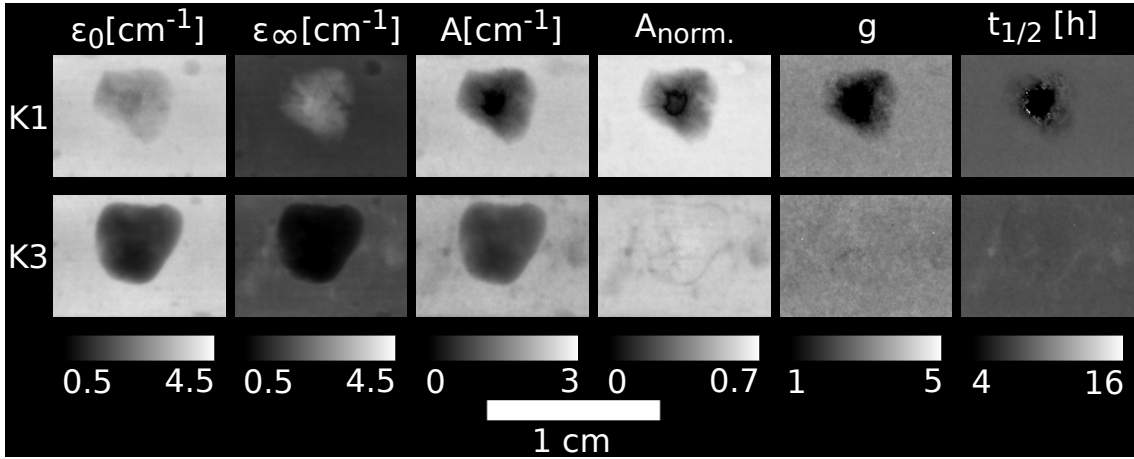


Figure 5.15.: This figure shows images obtained when fitting each pixel of a dark-field image series with a logistic curve as illustrated in figure 5.14. Each sample consisted of fresh cement paste and one limestone grain of type *K1* (upper image row) or *K3* (lower image row). While the grain of type *K3* vanishes in the images representing the normalized amplitude A_{norm} , the maximum gradient g and the half-life $t_{1/2}$, the limestone grain of type *K1* remains visible for all three fitting parameter images. This indicates a reaction induced by limestone grains of type *K1* which alters the logistic evolution of the scattering coefficient of fresh cement paste.

Figure 5.16 shows the images obtained by applying the described pixel-wise fitting procedure to a second measurement. Here, two grains of type *K1* were compared to another limestone grain of type *K2*. The fitting parameter images of the grains *K1*–1 and *K1*–2 show similar results as already observed for the grain of type *K1* in figure 5.15. The grains *K1*–1 and *K1*–2 are observed for each fitting parameter image. In contrast to that, the grain of type *K2* has similar characteristics as the *K3* grain shown in figure 5.15. While it is observed in the image representations of the parameters ϵ_0 , ϵ_∞ and A , it vanishes in the image representations of the parameters of A_{norm} , g and $t_{1/2}$.

5.5.3. Discussion

Our results show that limestone grains of different types have different impacts on the dark-field signal of fresh cement paste during setting and hardening. All grains decrease

5.5. INFLUENCE OF LIMESTONE GRAINS ON THE DARK-FIELD SIGNAL OF FRESH CEMENT PASTE

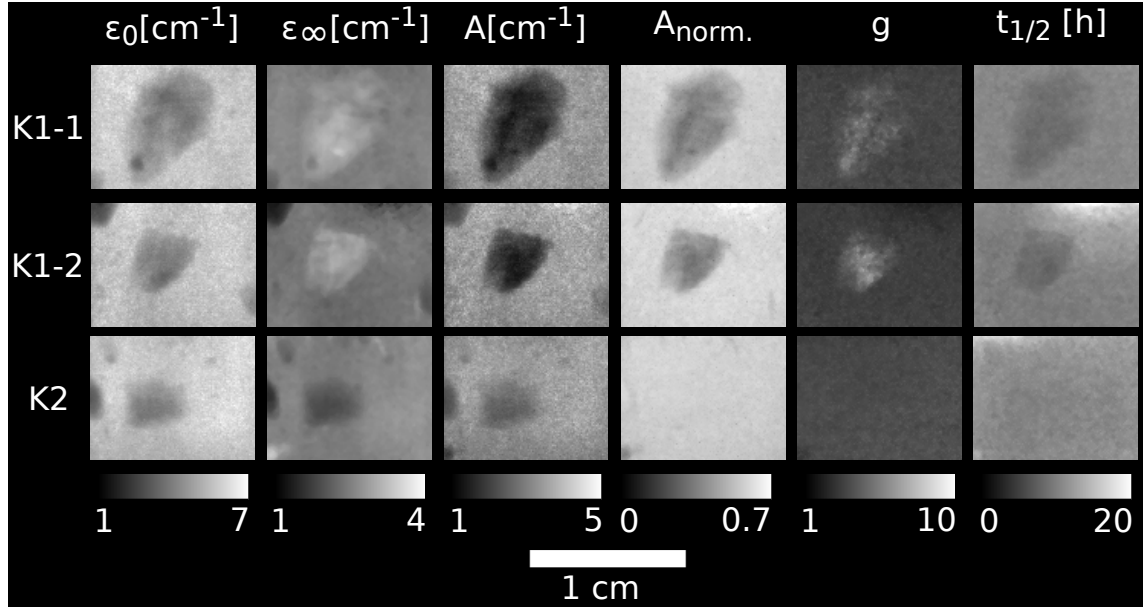


Figure 5.16.: This figure depicts fitting parameter images of three limestone grains embedded in fresh cement paste. While the grain of type $K2$ vanishes in the images representing the normalized amplitude $A_{\text{norm.}}$, the maximum gradient g and the half-life $t_{1/2}$, the two limestone grains of type $K1$ (i.e. $K1-1$ and $K1-2$) are visible in all fitting parameter images. This indicates a reaction induced by limestone grains of type $K1$ that alters the logistic evolution of the scattering coefficient of fresh cement paste. This is in good agreement with the findings of the experiment presented in figure 5.15.

the initial scattering strength of the sample in the vicinity of the grains. The grains replace cement paste, and less scattering occurs because they are more homogenous on the micrometer length scale as compared to cement paste. The experiments revealed that grains of type $K2$ and $K3$ disappear in the image representation of parameters $A_{\text{norm.}}$, g and $t_{1/2}$. These grains only replace cement paste and do not influence the hydration reactions. Therefore, they have no influence on the shape of the logistic curve. Except for an overall decrease in scattering. In contrast to that, we observed a deformation of the logistic curve for grains of type $K1$. This indicates that type $K1$ limestone grains influence the microstructural development in cement paste altering the shape of the logistic curve. As a result, grains of type $K1$ are visible in the image representation of parameters $A_{\text{norm.}}$, g and $t_{1/2}$. These grains reduce the normalized amplitude. Correspondingly, they reduce the half-time $t_{1/2}$. The data shown figure 5.16 also suggests that grains of type $K1$ speeds up the reactions in cement paste as the parameter g is increased around these grains. However, the data shown in figure 5.15 shows the opposite as the parameter g is lower around the $K1$ grain. These opposite observations are probably related to the fact that the two experiments were carried out with different distances d_{S,G_2} . To test the influence of sensitivity on the measurements the sample was placed further away from

5. APPLICATION OF X-RAY DARK-FIELD IMAGING IN CEMENT AND CONCRETE RESEARCH

the analyzer grating in the second measurement. Thus, these opposite observations for the maximum gradient g of type $K1$ grains might be related to microstructural effects varying on different length scales. Another possible reason are morphological or chemical differences between different grains of type $K1$. Nevertheless, the distinction between grains of type $K1$ and the other two types of limestone is unambiguous based on the data shown in figure 5.15 and 5.16. However, the question whether the observed effects originate from reactions within the cement paste or within the grains themselves remains. This is due to the two dimensionality of the presented dark-field images. To answer this question, we performed a time-resolved tomography experiment providing us with insight into the third dimension.

5.6. Time-resolved dark-field tomography on fresh cement paste containing limestone grains

5.6.1. Materials and methods

Sample preparation

The cement paste was prepared according to the same protocol mentioned for the previous experiments. The same type of cement (CEM I 42.5 R) was used, however, this time a water to cement ratio of $w/c = 0.4$ was used. Two grains of each type of limestone $K1$, $K2$ and $K3$ were chosen. These grains were separately mixed with the cement paste, and the two grains of each type were separately placed into two plastic tubes together with some fresh cement paste. The plastic tubes had an outer diameter of 1 cm and an inner diameter of 0.6 cm. After filling, each tube contained one limestone grain of each type embedded in fresh cement paste. The tubes were stacked on top of each other with their opening facing each other, and they were fixed together with a few windings of adhesive tape. The sample was mounted onto a tomographic stage and the measurement was started approximately 15 min. after mixing of cement powder with water. A schematic illustration of the experimental setup is shown in figure 5.17. After the tomography experiment, a thin section through the center of the sample was prepared for further polarized light and scanning electron microscopy (PLM and SEM, respectively) experiments. The thin section had a thickness of 20 μm and it was further vacuum impregnated in a fluorescent resin.

Experimental equipment and parameters

The tomographic study was performed with the set of gratings described in table 3.1 in chapter 3 and the experimental components described in chapter 3. The X-ray tube was operated at 60 kVp with a target power of 70 W resulting in a focal spot of smaller than 100 μm [58]. In the central region of the field of view, a mean visibility of 22.5% was

5.6. TIME-RESOLVED DARK-FIELD TOMOGRAPHY ON FRESH CEMENT PASTE CONTAINING LIMESTONE GRAINS

obtained before the measurement. The sample was placed between phase and analyzer grating at distance $d_{S,G_2} = 50.5$ cm from the analyzer grating. Hence, an effective pixel size of $93 \mu\text{m}$ was achieved.

The PLM images of the sample's thin section were acquired with an Olympus BX 61 light microscope using a crossed polarizer setup.

In order to reduce the surface charging of the sample's thin section during SEM measurements, it was sputtered with carbon prior to the experiment. We used a JEOL-JSM-6060LV scanning electron microscope from Jeol, Eching, Germany with an acceleration voltage of 10 kV. Several images of each grain were acquired with a back-scattered electron detector at different magnification factors ranging from $M = 200$ up to $M = 2000$.

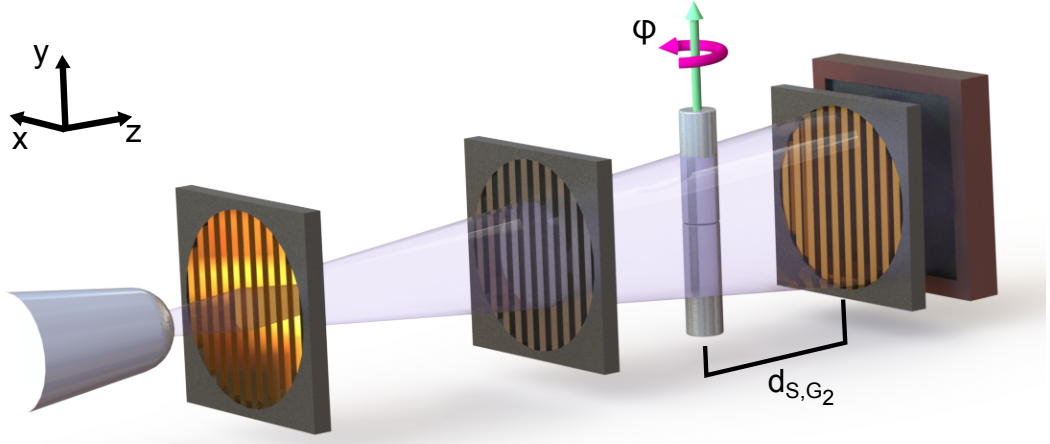


Figure 5.17.: This figure illustrates the experimental setup used for tomographic measurements. The sample was placed between G_1 and G_2 . Images were acquired, while the sample was rotated around the y -axis as indicated by the green and red arrows and angle φ . Based on images acquired from many angular views, a three dimensional distribution of the sample's attenuation and scattering coefficient was reconstructed.

Data acquisition, processing, reconstruction and analysis

Eight full sample rotations, each of them covering the angle φ from 0° to 360° , were performed over a time period of 37 h. Each of them consisted of $n = 441$ angular positions. The sample rotation by the angle φ around the tomographic axis is indicated in figure 5.17 by the green and red arrows. In total, $N = 3528$ angular projections were acquired. Each full rotation was divided into 21 blocks. Each block consisted of 5 reference scans (without sample) and 21 sample scans acquired with increasing angle φ . For each reference and sample scan, 7 phase steps were acquired with an exposure time of 2 s per step. In addition, the sample was shifted by a random but logged number of pixels in x -direction

5.6. TIME-RESOLVED DARK-FIELD TOMOGRAPHY ON FRESH CEMENT PASTE CONTAINING LIMESTONE GRAINS

For data analysis, the first reconstruction R_1 of the scattering coefficient ε was used to segment each limestone grain from the cement paste. The commercially available software VGStudio MAX 2.1 from Volume Graphics GmbH, Germany was used for this purpose. Based on this segmentation, binary three dimensional pixel masks were extracted. Pixels corresponding to cement were labeled with 0, while pixels corresponding to the limestone grains were labeled with 1. The corresponding volumes resulting from this segmentation are shown in figure B.3 in appendix B. Using this mask, the time evolution of the mean scattering coefficient ε and of the mean attenuation coefficient μ were calculated for each limestone grain and the cement paste surrounding each grain. The data of each reconstruction was assigned to the point in time after which half of the corresponding image subset was acquired. Hence, the first and last data set was assigned to a time of $t = 2.3$ and $t = 34.8$ h, respectively.

5.6.2. Experimental results

Dark-field CT results

Figure 5.18 shows transmittance and dark-field images acquired at 0 h, 9.2 h and 18.5 h after sample preparation. Every image shows the sample at the same viewing angle $\varphi = 0^\circ$. The plastic tube and the cement paste filling are clearly observable in the transmittance images. However, the six limestone grains are not visible.

The sample's transmittance signal does not change in time as shown by the transmittance images. In contrast to that, the six limestone grains $K1T$, $K2T$, $K3T$, $K1B$, $K2B$ and $K3B$ are shown by dark regions in the dark-field images in figure 5.18. The letters T and B indicate the position of each grain in the top or the bottom part of the plastic tube, while $K1$, $K2$ and $K3$ indicate the type of limestone corresponding to the previous experiment. The cement paste's dark-field signal decreases with time as it was expected based on the previous experiments.

Furthermore, the two limestone grains $K1T$ and $K1B$ loose contrast during the measurement. Both grains are barely visible in image f). In contrast to that, grains $K2T$, $K3T$, $K2B$ and $K3B$ are still clearly visible after 18.5 h.

Figure 5.19 shows slices through the sample's center reconstructed for different points in time. Grains $K2T$, $K3T$, $K2B$ and $K3B$ appear brighter than the cement paste in images a-c) indicating higher attenuation coefficients as compared to cement paste. Grains $K1T$ and $K1B$ appear with lower contrast to the surrounding cement paste indicating similar attenuation coefficients for these two materials.

5. APPLICATION OF X-RAY DARK-FIELD IMAGING IN CEMENT AND CONCRETE RESEARCH

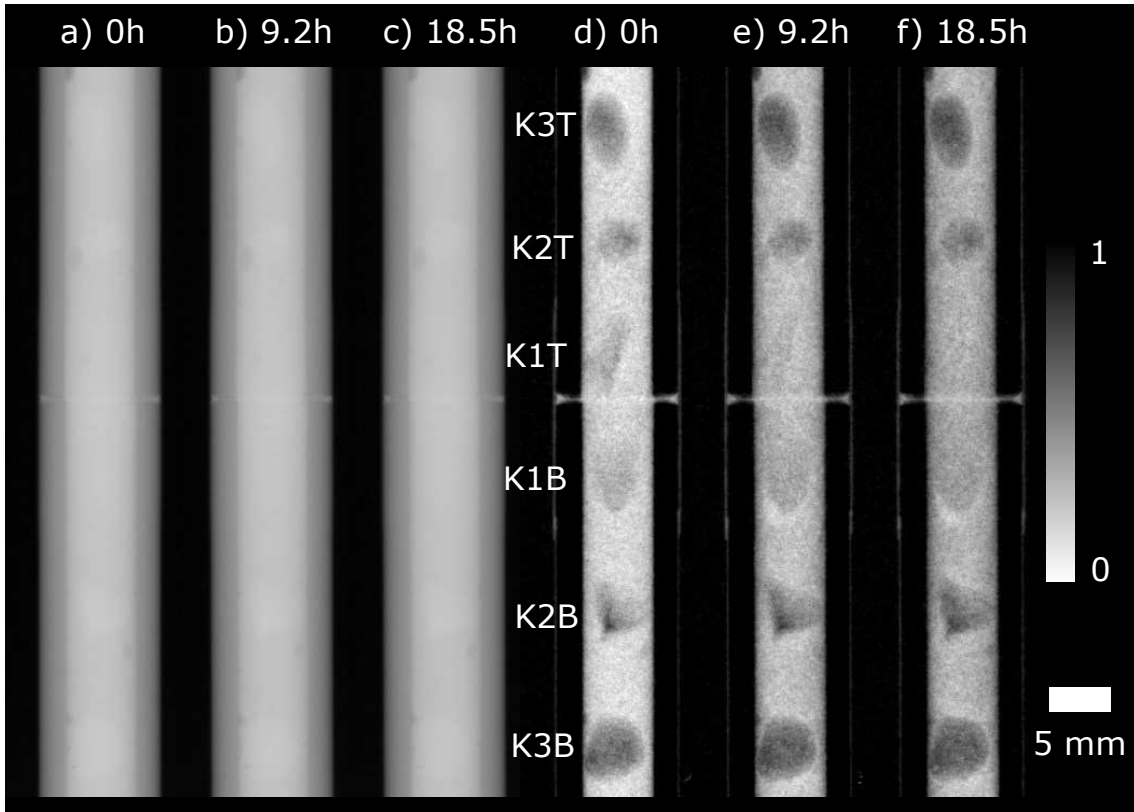


Figure 5.18.: Images a-c) show transmittance images, while images d-f) show dark-field images of a cylindrical cement sample acquired at 0 h, 9.2 h and 18.5 h after sample preparation at an angle of $\varphi = 0$. The six limestone grain's vertical positions are marked by the labels $K1T$, $K2T$, $K3T$, $K1B$, $K2B$ and $K3B$ shown in the middle of this figure. The numbering corresponds to the type of limestone of each grain, while the letters T and B indicate their position in the top or bottom plastic tube. While the limestone grains are not visible in the transmittance images, they are clearly visible in the dark-field images. Grains of type $K1$ loose contrast when compared to the cement after 18.5 h as they have almost vanished in image f).

The corresponding reconstructions of the scattering coefficient are shown in images d)-f). Here, all grains initially appear as dark regions indicating reduced scattering coefficients when compared to the cement paste. The scattering signals of grains $K2T$, $K3T$, $K2B$ and $K3B$ remain unchanged in time. In contrast to that, the scattering signal of grains $K1T$ and $K1B$ increases with time. The cement paste's scattering signal decreases throughout the measurement in the whole sample.

These findings are further supported by figure 5.20 showing the time evolution of the attenuation (dashed curves) and scattering coefficient (solid curves) for each grain and its surrounding cement paste.

5.6. TIME-RESOLVED DARK-FIELD TOMOGRAPHY ON FRESH CEMENT PASTE CONTAINING LIMESTONE GRAINS

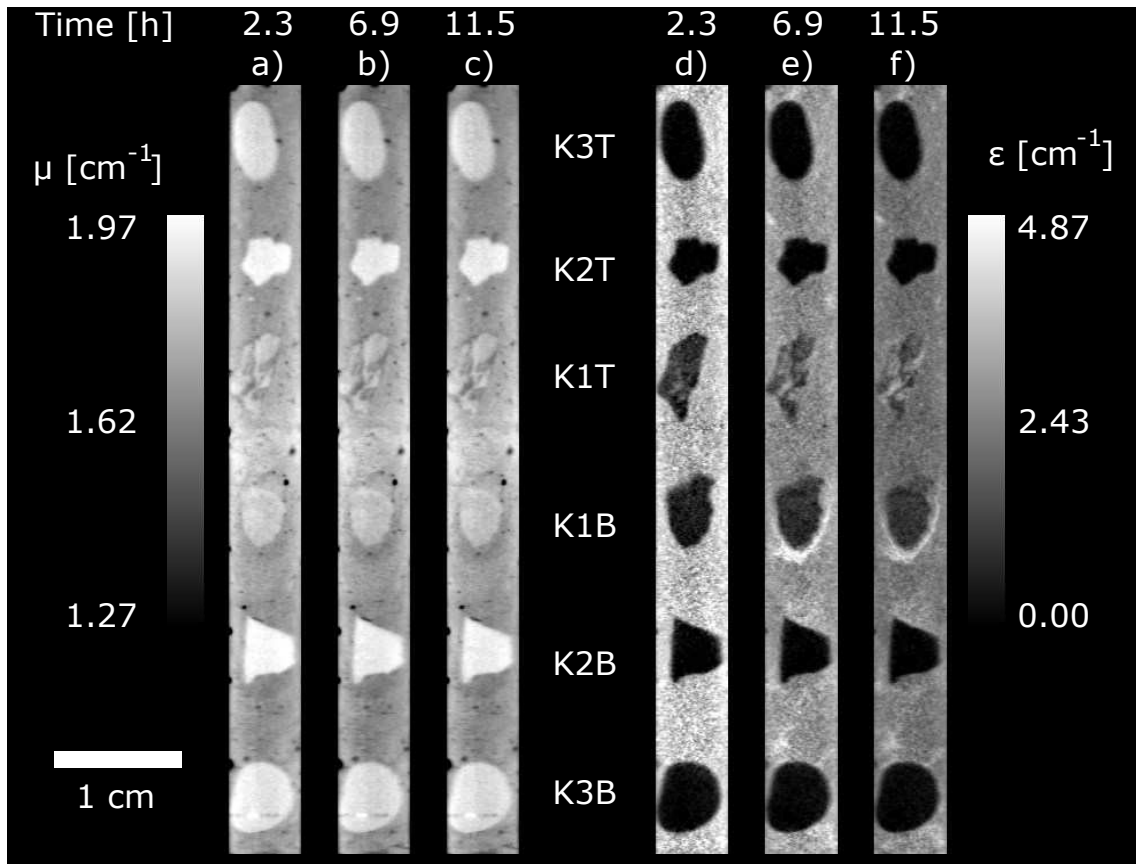


Figure 5.19.: This figure shows reconstructions of the attenuation coefficient (a-c) and the scattering coefficient (d-f) for a slice through the center of reconstruction R_1 (a), R_{21} (b) and R_{42} (c), i.e. at 2.3 h, 6.9 h and 11.5 h after sample preparation. While the grains of type $K2$ and $K3$ appear very bright in images a-c) as compared to the cement, the grains of type $K1$ have lower attenuation coefficients. Furthermore, the attenuation coefficients remain unchanged during the experiment. The corresponding reconstructions of the scattering coefficient are shown in images d-f). Here, the six limestone grains are clearly shown by the dark regions, however, the grains of type $K1$ initially display increased scattering signal as they are slightly brighter when compared to grains of type $K2$ and $K3$. Furthermore, the scattering signal of grains of type $K1$ increases with time, while scattering coefficients for grains of type $K2$ and $K3$ remain unchanged.

The curves were obtained by calculating the attenuation and scattering coefficient for each of the 147 reconstructions. The attenuation coefficient of limestone type $K1$ is similar to the attenuation coefficient of cement paste. This is shown by the dashed curves in graph a), which are very close to each other. The attenuation coefficient of limestone types $K2$ and $K3$ are higher when compared to the cement paste. Therefore, the brown and dark-blue dashed curves are at a higher level as compared to the purple and green dashed

5. APPLICATION OF X-RAY DARK-FIELD IMAGING IN CEMENT AND CONCRETE RESEARCH

curves in graph b) and c). The scattering coefficients time evolution in cement paste follows a logistic decline as shown by the green and pink solid curves in each of the three graphs. The limestone grains *K2* and *K3* have low but constant scattering coefficients as shown by the blue and orange solid curves in graph b) and c). In contrast to that, type *K1* limestone grains show a strong increase in scattering within the first 10 h of the experiment. This is shown by the orange and blue solid curves in graph a). After 10 h their scattering signal reaches constant levels.

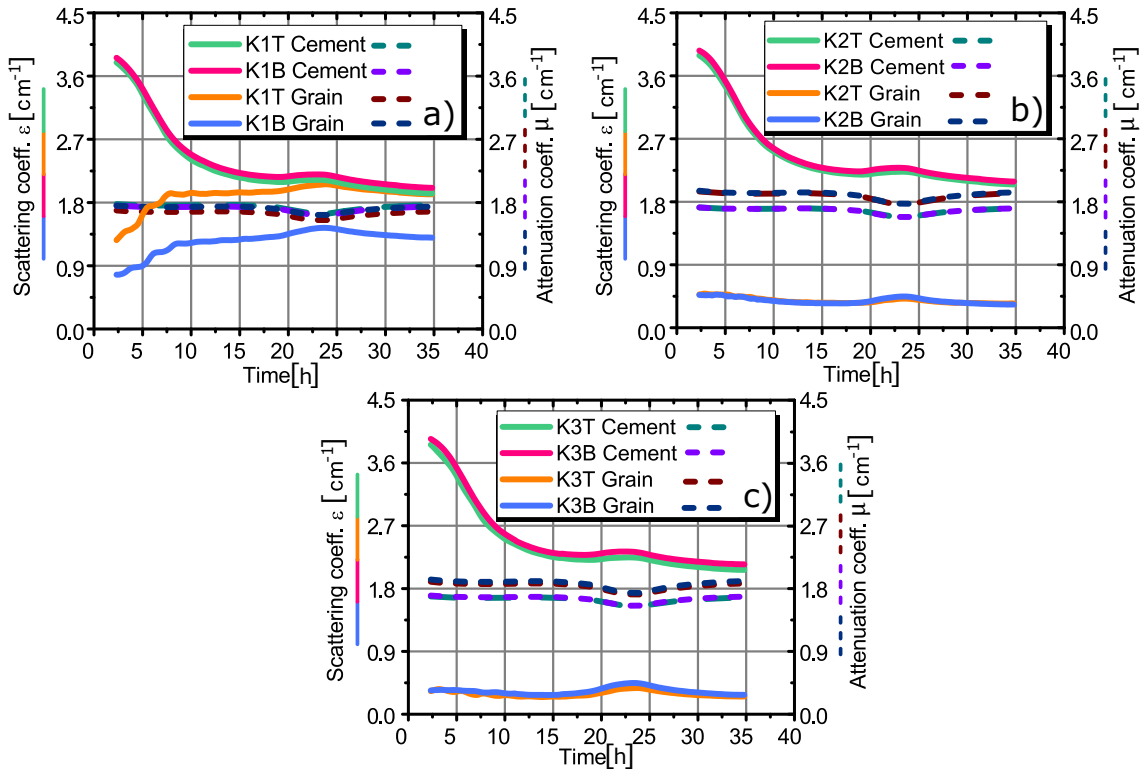


Figure 5.20.: Graphs a-c) show the attenuation (dashed curves) and scattering coefficients (solid curves) of each limestone grain (orange, brown, light blue and dark blue curves) and the cement surrounding each grain (pink, purple, light and dark green curves). The attenuation coefficients of cement and all limestone grains remain unchanged. While grains of type *K2* and *K3* show slightly higher attenuation coefficients than cement paste, the grains of type *K1* show attenuation coefficients similar to cement paste. This is shown by the dashed curves in graphs a) and c). The scattering coefficient of cement paste follows a logistic shape, while the scattering coefficients for limestone grains of type *K2* and *K3* remain constant and low. The scattering coefficients of limestone grains of type *K1* increase within the first 10 h after sample preparation. Instabilities of the X-ray tube resulted in a signal variation at 20 – 25 h after sample preparation.

5.6. TIME-RESOLVED DARK-FIELD TOMOGRAPHY ON FRESH CEMENT PASTE CONTAINING LIMESTONE GRAINS

Polarized light and scanning electron microscopy results

To understand the effects observed in the tomography data we acquired images of a thin section of the sample with polarized light and scanning electron microscopes. This thin section was produced after the tomography experiment by diamond sawing. The PLM images are shown in figure 5.21.

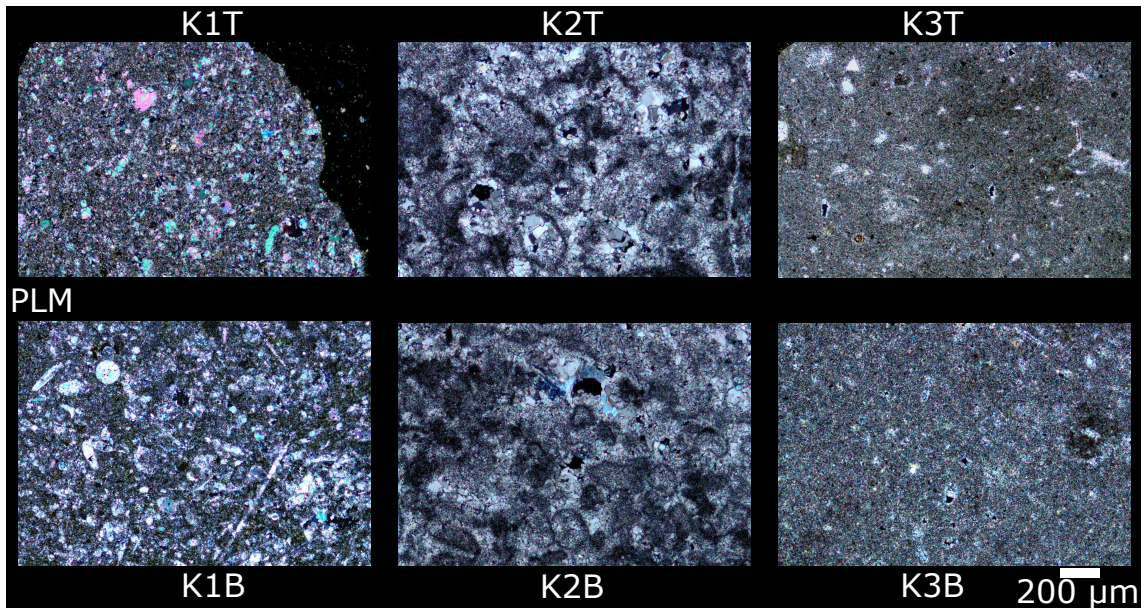


Figure 5.21.: This figure shows PLM images of a thin section of each limestone grain. PLM images provide information on the crystalline structure of minerals. While the crystalline structure varies for the different types of limestone, all grains have the same chemical composition and are made of pure calcite $CaCO_3$.

They provide information on the crystalline structure and the chemical composition of each grain. All grains are made of pure calcite, while the grains of type *K3* also contain some quartz particles. Grains of type *K1* contain many fossil fragments shown by round and ellipsoidal features. These fossil fragments are embedded in a micro-crystalline (micritic) carbonate matrix. Micro-crystalline means that mono-crystalline regions of the same crystal orientation are smaller than $63 \mu\text{m}$ in size. Micro-crystalline regions appear dark in the presented images. Therefore, cement paste is black as shown on the right side of the image of grain *K1T*. Grains of type *K2* are fine crystalline to micritic limestone with round features, called spherulites. Fine crystalline regions are large regions with a mono-crystalline phase. They are represented by bright colorful regions in the images. In grains of type *K3*, small areas of fine crystalline calcite are found in an otherwise majorly micritic matrix.

Figure 5.22 shows high resolution SEM images of the grain's thin sections. Limestone

5. APPLICATION OF X-RAY DARK-FIELD IMAGING IN CEMENT AND CONCRETE RESEARCH

grains of type $K1$ show a distinct pore system, while the grains of type $K2$ and $K3$ have no significant level of porosity. The bright spots observed especially for grain $K2B$ correspond to surface charging of insulated regions. The porosity found in grains of type $K1$ is not localized to certain regions within the grains. It affects the whole grain. This is emphasized in figure 5.23, which shows SEM images of each grain at less magnification. Hence, they show a larger ROI within each grain as compared to the SEM in figure 5.22. Limestone grains of type $K2$ and $K3$ show almost no porosity even within this enlarged ROI.

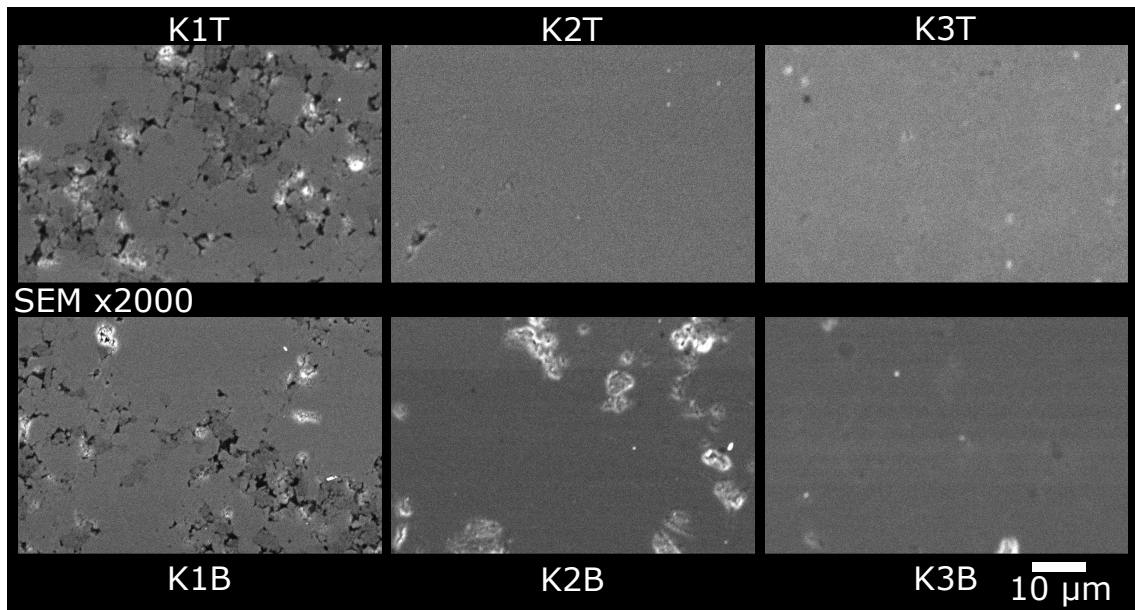


Figure 5.22.: This figure shows SEM images of a thin section of each limestone grain acquired with a magnification of $M = 2000$. The limestone grains of type $K1$ have a distinct pore system (dark spots), while the grains of type $K2$ and $K3$ show almost no porosity.

5.6.3. Discussion

The results presented in this section show that the observations of the previous experiment are related to an effect within limestone grains of type $K1$. While the cement particles hydrate and form a hydration phase around each particle, the scattering coefficient of cement paste decreases. Simultaneously, we observed an increase of the scattering coefficient within limestone grains of type $K1$. Such a behavior is not observed for grains of type $K2$ and $K3$, which have a constant and low scattering signal throughout the whole experiment. The microscopy experiments revealed that the three different types of limestone only differ by means of their porosity. Chemically they are the same as they are all

5.6. TIME-RESOLVED DARK-FIELD TOMOGRAPHY ON FRESH CEMENT PASTE CONTAINING LIMESTONE GRAINS

made up of pure calcite. This finding excludes chemical reactions within the particles as a possible reason for the observed increase in scattering strength. The increase in scattering strength is therefore related to the high porosity found in the grains of type *K1*.

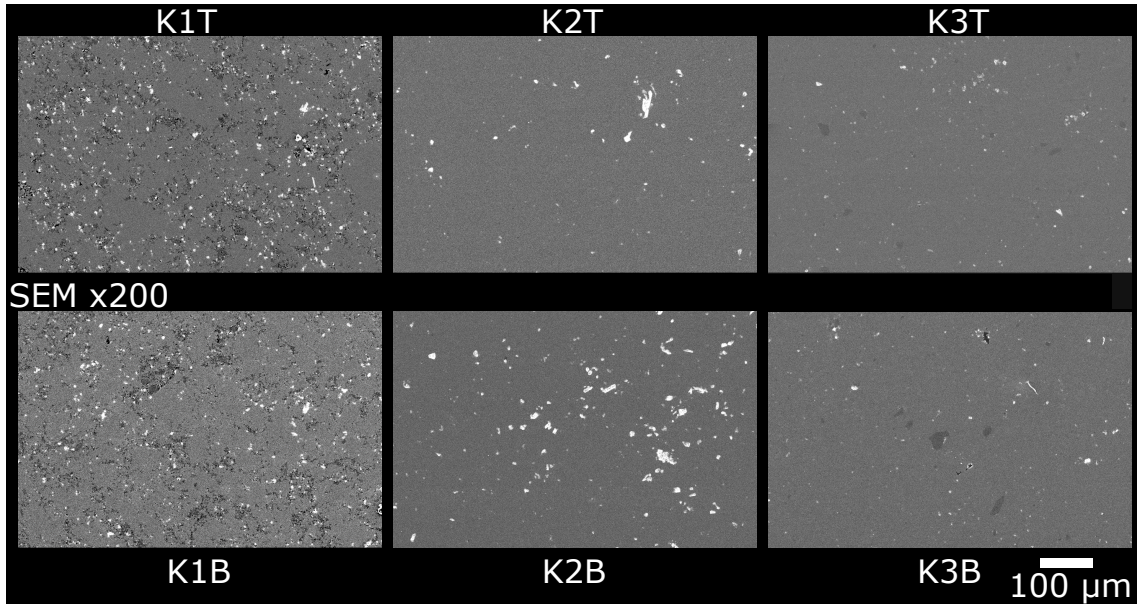


Figure 5.23.: This figure shows SEM images of a thin section of each limestone grain acquired at a lower magnification as compared to figure 5.22(compare scale bar). The porosity in grains of type *K1* spreads over the full image emphasizing that the whole grain is affected and that this porosity is not a localized phenomenon. In contrast to that, grains of type *K2* and *K3* do not show a significant porosity even within this enlarged ROI.

The experiments presented at the very beginning of this chapter have shown that water intrusion into the pore system of a porous materials results in a decrease in scattering strength. Consequently, water that drains out of the pore system results in an increase in scattering strength. The grains were added to the cement during mixing. Due to capillary suction, the pore system of the grains of type *K1* saturated with water during mixing. As the hydration of the cement particles consumes water, an empty pore system is created within cement paste during hydration. This pore system results in capillary forces, which drain the water out of the limestone grain's pore system into the cement paste [106]. This mechanism is a very likely explanation of the observed increase in scattering strength.

Internal supply of water to cement during setting and hardening is often referred to as internal curing [107]. In contrast to that, external curing is referred to a method where additional water is supplied from the outside. Since this water supply affects the mechanical properties as well as the long term durability of cement, internal curing is a

5. APPLICATION OF X-RAY DARK-FIELD IMAGING IN CEMENT AND CONCRETE RESEARCH

very active field in cement research. Materials such as porous light weight aggregates or super-absorbent polymers have the potential to serve as internal curing agents.

5.7. Summary and discussion

The results presented in this chapter point out the potential of grating-based X-ray dark-field imaging to serve as a valuable tool for studying building materials such as mortars or cement. We showed how water intrusion in porous materials affects X-ray dark-field images as wet regions scatter less when compared to dry regions. The contrast between wet and dry regions is higher for the dark-field signal when compared to conventional attenuation-based X-ray imaging. Furthermore, we studied changes in water sorptivity when modifying mortars by adding hydrophobic biofilm to the material. The hydrophobic biofilm prevents water intrusion into the mortars pore system. Besides these time-resolved radiography measurements, a method for time-resolved tomography was developed. It allows to study water transport and cement hydration in in three dimensions over time.

Studies on the hydration of cement paste are another important aspect of this chapter. Our results show that hydration kinetics of cement paste can be studied with the advantage of spatially resolving variations of this process within our samples. Here, we could also study the effect of temperature on cement paste's hydration. While reactions slowed down in the cooled sample decelerating the scattering signal's decrease, a speed up in reaction rate was observed for a heated cement sample. The change in scattering during hydration of cement paste was studied by two-dimensional dark-field radiography as well as in a time-resolved tomography experiment. Compared to conventional testing methods, grating-based X-ray dark-field imaging represents a new approach in studying cement-based materials due to the spatial resolution of the obtained data.

6. Fiber orientation characterization in fiber reinforced materials with X-ray dark-field imaging

This chapter outlines the potential of X-ray dark-field imaging to study fiber orientation in fiber reinforced materials.

The presented results are published in the following article and parts of the following text are adapted from this article:

F. Prade et al. "**Nondestructive characterization of fiber orientation in short fiber reinforced polymer composites with X-ray vector radiography**". In: *NDT & E International* 86 (2016), pp. 65–72. DOI: 10.1016/j.ndteint.2016.11.013

6.1. Introduction to fiber reinforced materials

Microstructural properties determine the macroscopic mechanical characteristics of any material. Composite materials therefore use different materials, which are combined to manufacture components with properties adjusted to their use. Fiber reinforced composite materials are a famous example. Many industrial fields such as automotive and consumers industry use short glass and carbon fiber reinforced polymer (SFRP) composites for manufacturing. Their physical and mechanical properties are often superior when compared to the pure polymer material. Fiber orientation is a very important characteristic especially for SFRP components as it is not known prior to the manufacturing process. During manufacturing, for example by injection molding, fibers align according to the flow of the molten matrix polymer [109]. Anisotropic fiber orientations are the result and lead to the formation of features such as weld-lines. This strongly influences the mechanical properties of SFRP components. Especially weld-lines decrease the mechanical strength compared to the rest of the injection-molded part [110]. Thus, experimental methods for microstructure characterization have to be consistently improved along with the development of new materials and the advancements of already established materials.

Carbon or glass fiber reinforced polymer (CFRP or GFRP) components are currently tested by materialographic specimen preparation, visual examination, and tap testing.

6. FIBER ORIENTATION CHARACTERIZATION IN FIBER REINFORCED MATERIALS WITH X-RAY DARK-FIELD IMAGING

For example, porosity and fiber content are destructively tested by wet chemical analysis. Besides these visual methods, ultrasonic testing and active thermography are other established NDT methods [111, 112]. In automotive and aerospace industries, ultrasonic testing [113] and acid digestion [112] are state of the art testing methods. However, they only deliver two-dimensional spatial information of the components structure.

X-rays are the tool of choice to probe a materials internal structure and geometry as they penetrate matter without being fully attenuated. X-ray radiography and CT are the most common techniques applied to obtain information on the internal structure of a material in two or three dimensions, respectively [36]. For example, CT is extensively applied for the analysis of fiber orientation and fiber length distribution in fiber reinforced materials such as CFRPs or GFRPs [37, 38, 114]. Fiber orientation is extracted after a CT measurement by processing algorithms. These algorithms require high resolution data which resolves single fibers at high contrast to the surrounding matrix. Fiber diameters are approximately in the range of $5 - 10 \mu\text{m}$ for CFRPs and $10 - 20 \mu\text{m}$ for GFRPs. This limits the measurable sample size because the sample's physical dimensions limit the spatial resolution of CT scans. Single fibers can simply not be resolved in large samples. Thus, a sample of several centimeters in size has to be divided into several pieces with smaller dimensions, usually below 5 mm. Furthermore, the attenuation contrast between fibers and matrix material has to be strong in order to ensure robustness of the applied processing algorithm. This is not always the case for carbon fibers (1.8 g/cm^3) embedded in a polymer matrix, e.g. polyamide (1.15 g/cm^3). Even though contrast is higher for carbon fibers and a polypropylene matrix (0.94 g/cm^3) it is still not as high as between glass fibers (2.5 g/cm^3) and a polymer matrix. Hence, for large samples and materials suffering from weak attenuation contrast, CT based fiber extraction techniques are prone to errors. In addition, high resolution CT measurements are time consuming as they usually last for several hours.

In the following, we present results that point out the potential of grating-based X-ray dark-field imaging to relax some of these limitations. Due to the interferometer's unidirectional sensitivity for scattered X-rays, the relative orientation between the gratings and the scattering structures influences the detected dark-field signal [115–117]. This property has recently been used to obtain information on fiber orientation in CFRPs and GFRPs [35, 118]. In the present study, we measure fiber orientation of various SFRP components made of different size, geometry and fiber material. Our results show that X-ray vector radiography (XVR), which is an extension to grating-based X-ray dark-field imaging, does not suffer from the mentioned limitations of CT measurements [32, 76, 119]. It is much faster but still provides results which are qualitatively comparable to CT data. Furthermore, the fiber orientation comes as a physical measure and is not extracted via data processing algorithms. We show that weld-lines are easily studied in flat components with this technique, while neither the fiber material nor the component's

6.2. MEASUREMENTS ON SHORT FIBER REINFORCED POLYMER COMPONENTS WITH X-RAY VECTOR RADIOGRAPHY

size complicates the measurements.

6.2. Measurements on short fiber reinforced polymer components with X-ray vector radiography

6.2.1. Materials and methods

Sample specifications

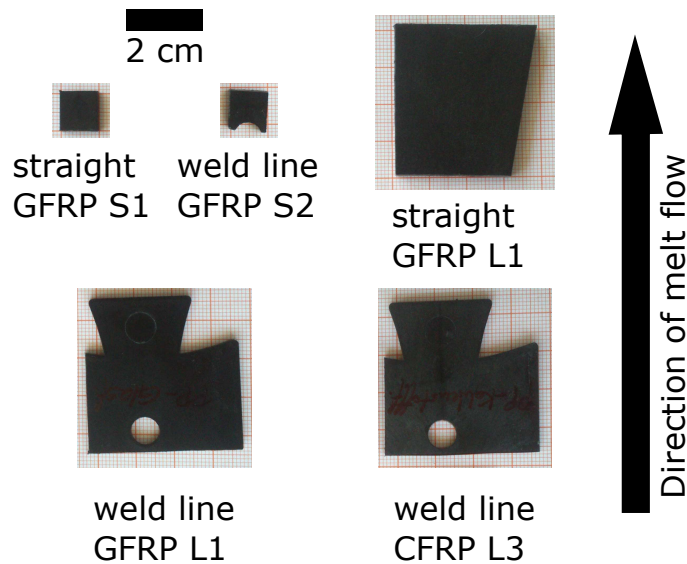


Figure 6.1.: This figure shows photographs of the SFRP samples studied with XVR in this work. The direction of injection, i.e. the flow direction of the molten polymer, is given by the black arrow.

Photographs of the samples used in this study are shown in figure 6.1. All samples have a fiber content (glass or carbon fibers, respectively) of about 30 weight percent. Fiber diameters are about $18 \mu\text{m}$ for glass and $7 \mu\text{m}$ for carbon fibers. Samples *S1* and *S2* are GFRPs produced by injection molding with a thickness of 2 mm. Density of glass was about 2.52 g/cm^3 . The mean granulate fiber length is assumed to be around $400 \mu\text{m}$. Polypropylene was used as the matrix material with a density of 0.9 g/cm^3 . Samples *S1* and *S2* were cut from longer parts in which the molten polymer flowed along the long axis. Fibers are therefore expected to be aligned with the injection direction in *S1*, which is given by the arrow in figure 6.1. *S2* was cut from a region of a larger sample which contained a hole. The melt front splits in front of such a hole and flows together behind the hole creating a weld-line. The large samples are a straight segment *L1*, with

6. FIBER ORIENTATION CHARACTERIZATION IN FIBER REINFORCED MATERIALS WITH X-RAY DARK-FIELD IMAGING

a thickness of 4 mm, containing glass fibers and two samples with a hole containing glass ($L2$) fibers and carbon fibers ($L3$) and a thickness of 2 mm. The samples $S1$ and $S2$ have already been studied by CT and dark-field CT in a previous study [118].

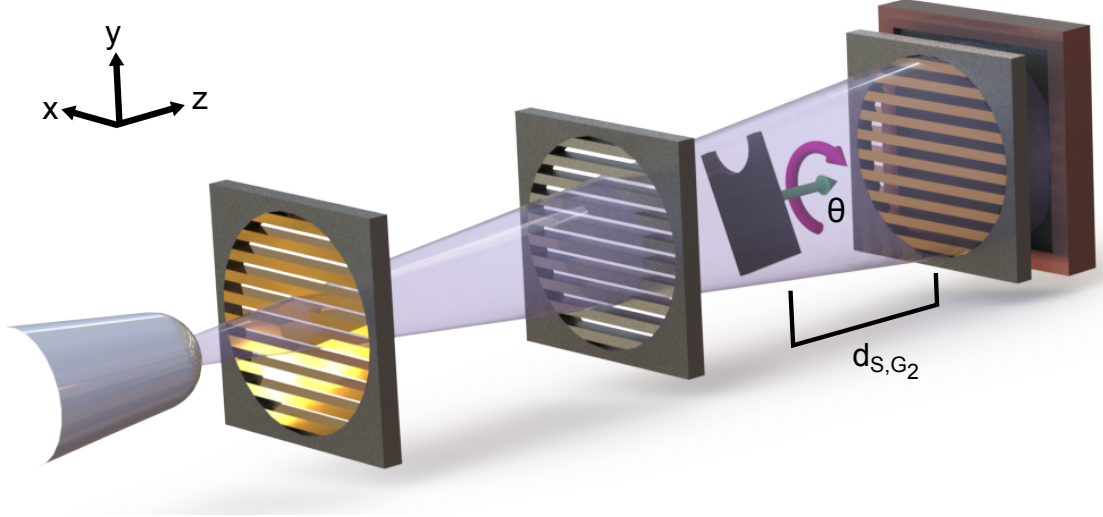


Figure 6.2.: This figure shows a schematic illustration of an XVR measurement. Images are acquired for different angles Θ , while the sample is rotated around the optical axis as indicated by the green and pink arrows.

Experimental equipment and parameters

The XVR experiments were carried out with the set of gratings described in table 3.2 in chapter 3 and the experimental equipment as described in chapter 3. The tube was operated at 60 kVp, while the tube power was set to 100 W. In a first experiment, all samples shown in figure 6.1 were placed between the phase and analyzer grating, G_1 and G_2 , at a distance of 33 cm to the phase grating. This resulted in an image pixel size of 86 μm . Additionally, samples $S1$ and $S2$ were placed between the source and phase grating, G_0 and G_1 , in second experiment. The tube power was set to 20 W and the distance to the phase grating was 55 cm, in this case resulting in an image pixel size of 29 μm . A schematic representation of an XVR measurement is shown in figure 6.2. For comparison, high resolution CT measurements were carried out for samples $S1$ and $S2$, while for samples $L1$, $L2$ and $L3$ high resolution radiography images were acquired. The radio- and tomography experiments were performed at the University of Upper Austria. The specimens were scanned with a Nanotom 180NF (GE phoenix|X-ray). This system consists of a nanofocus tube and a 2304x2304 pixel Hamamatsu detector (Hamamatsu City, Japan). Molybdenum was used as the target material. The scanning parameters for investigating the samples $S1$ and $S2$ were 80 kV tube voltage, 180 μA tube current, 1800 total projections and a voxel size of 6.5³ μm^3 . Six single images were averaged resulting in

6.2. MEASUREMENTS ON SHORT FIBER REINFORCED POLYMER COMPONENTS WITH X-RAY VECTOR RADIOGRAPHY

one projection. The integration time for each single image was 750 ms. `Datos|x` was used as the reconstruction software. It works with a FBP, and a beam-hardening correction was applied as well.

Data acquisition and processing

For XVR measurements, the samples were rotated around the optical axis by an angle $\Theta = 0^\circ \dots 360^\circ$, as indicated by the green and pink arrow in figure 6.2. Prior to each experiment, one reference scan was acquired. We acquired attenuation and dark-field images for 31 positions of Θ , each consisting of 7 phase steps with an exposure time of 2 s per step. Here, we emphasize that the attenuation and dark-field images are acquired just by one measurement at the same time for each angle Θ . The visibility of the reference scan was around 30 % prior to the experiments.

After acquisition, all acquired dark-field images are rotated and registered to match the dark-field image acquired for $\Theta = 0^\circ$. This is done by a processing algorithm operating on the attenuation images because they are unaffected by the rotation of the sample. After registration, a data set for each XVR measurement consists of the 31 dark-field images, which were initially obtained at different angles Θ , but are now perfectly registered to the image acquired at $\Theta = 0^\circ$. The dark-field signal depends on the relative orientation between the grating lamellae and the scattering features of the sample [119]. Thus, a changing dark-field signal is expected when analyzing the same pixel in all 31 registered dark-field images. It has been shown that, for fibrous materials such as wood, leaves, teeth and polypropylene fibers, the detected dark-field signal is strongest when fibers are aligned parallel to the grating lamellae [76, 115, 116, 119]. If fibers are aligned perpendicular to the grating lamellae, the scattering signal decreases to a minimum. The dependence of the dark-field signal and the sample orientation defined by angle Θ is given by the following equation [116, 119]:

$$DF(\Theta) = \exp - [a_0 + a_1 \cos(2(\Theta + \varphi))] \quad . \quad (6.1)$$

$DF(\Theta)$ denotes the measured dark-field signal in one pixel as a function of Θ . a_0 represents the average scattering strength of the sample in each pixel, while a_1 describes the anisotropic part of this scattering strength. The ratio a_1/a_0 gives the degree of anisotropy indicating the fraction of scattering structures oriented with the preferred orientation φ [120]. If this ratio is one all structures that contribute to the scattering signal are aligned with this preferred orientation. On the opposite, if this ratio is zero, the scattering features are randomly distributed and no preferred orientation can be determined. The contribution of the anisotropic scattering to the detected signal depends on the relative orientation between scattering structures and the grating lamellae, which is denoted by

6. FIBER ORIENTATION CHARACTERIZATION IN FIBER REINFORCED MATERIALS WITH X-RAY DARK-FIELD IMAGING

φ [76]. Plotting the dark-field signal of the same pixel in all 31 dark-field images against its original acquisition angle Θ results in an oscillating curve which can be fitted by equation 6.1. Performing such a fit on every pixel provides three parameters a_0 , a_1 and φ for each pixel. This procedure is illustrated in figure 6.3.

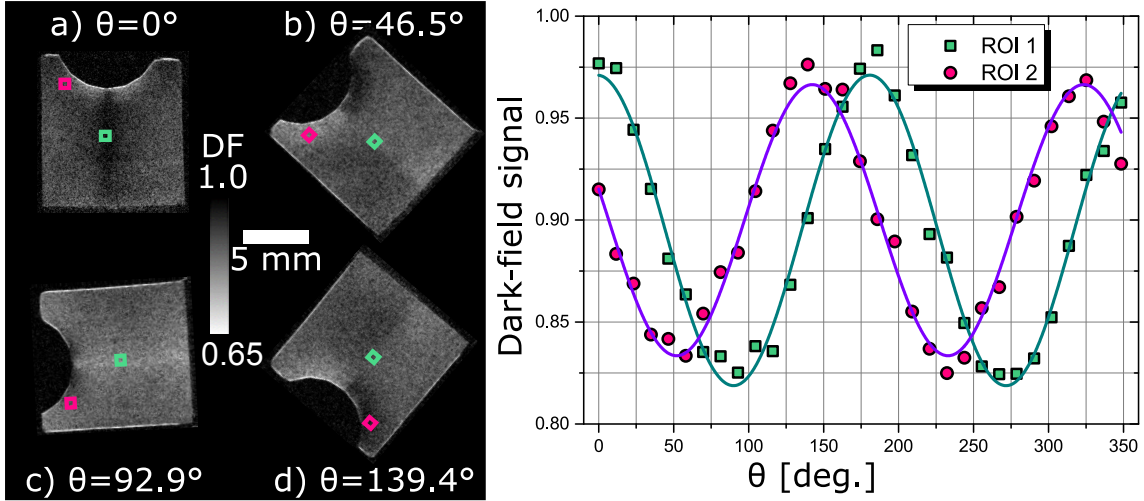


Figure 6.3.: This figure illustrates the work-flow of XVR measurements. Images a-d) show unregistered dark-field radiographs of sample *S2* for 4 of the 31 angles Θ . A change in the dark-field signal is observed for different regions. This is emphasized by plots of the dark-field signal from the two marked regions (green and pink rectangles) over the angle Θ . Clearly, the signal oscillates as the sample is rotated around the optical axis. The shift between the two curves indicates a difference in fiber orientation in the two marked regions.

Unregistered dark-field images of sample *S2* are shown for 4 of the 31 different acquisition angles Θ . Clearly, the dark-field signal of the sample depends on the orientation around the optical axis as the dark-field signal in different regions changes throughout the four images. For example, the black line running from top to bottom in the center of the sample in image a) appears brighter in image c). This rotational dependence is emphasized by the plot on the right hand side of figure 6.3. Here, the dark-field signal in the green and pink regions marked in the images is plotted against the acquisition angle for all 31 images of the XVR measurement. The two curves obviously oscillate with twice the rotation frequency of the sample, thus, being in accordance with equation 6.1. Furthermore, the curves are slightly shifted to each other indicating a difference in fiber orientation between the green and pink region. By fitting these curves according to equation 6.1, the fiber orientation is given by φ . This parameter is represented by vectors in the following indicating the preferred orientation of the fibers in the corresponding pixel. For a better visualization all vectors are shown with the same length. The ratio a_1/a_0 is represented as a color coding of these vectors, and it represents the fiber amount which is oriented in

6.2. MEASUREMENTS ON SHORT FIBER REINFORCED POLYMER COMPONENTS WITH X-RAY VECTOR RADIOGRAPHY

the preferred direction. The average scattering parameter a_0 represents the total amount of fibers in each pixel. This parameter was found to be quite homogenous within each of the measured samples. Therefore it was used as a threshold to assign the vectors obtained for image regions containing air with a vector length of zero. The following results do not show the fiber orientation and degree of orientation for each single pixel to assure good visualization. For images acquired with a pixel size of $29 \mu\text{m}$, the orientation is shown only for every 25th pixel, while the orientation vectors are shown in every 8th pixel for measurements acquired with a pixel size of $86 \mu\text{m}$.

6.2.2. Experimental results

XVR results

Figure 6.4 shows results of XVR measurements on samples $S1$ and $S2$. The preferred fiber orientation is shown for both samples by colored vectors as an overlay onto an attenuation projection of each sample. Furthermore, results are compared for two measurements obtained with different pixels size. The results emphasize that the pixel size does not influence the extraction of fiber orientation in XVR measurements.

While the fibers homogeneously run from top to bottom in sample $S1$ they are aligned around the hole in sample $S2$ and form a so-called weld-line. This weld-line is represented by a region in the middle of sample $S2$ where all vectors point along the vertical axis of the image. On the left and right hand side of the weld-line, fibers fan out. The coloring of the vectors illustrates the degree of anisotropy a_1/a_0 . It shows that a large amount of fibers is aligned along the preferred direction for sample $S1$ as well as around the hole and along the weld-line in sample $S2$. In contrast to that, only a small fiber amount is aligned along the preferred direction in other regions of $S2$. The parameter φ is shown for the three regions (see figure 6.1) in table 6.1 to quantitatively compare the fiber orientation obtained with XVR measurements acquired with different pixel sizes.

Table 6.1.: This table emphasizes that the effective pixel size does not influence the measured fiber orientation in XVR. The parameter φ is shown in radians for three regions marked in figure 6.4.

	$S1 \ 29 \ \mu\text{m}$	$S1 \ 86 \ \mu\text{m}$	$S2 \ 29 \ \mu\text{m}$	$S2 \ 86 \ \mu\text{m}$
ROI1	1.515	1.542	2.111	2.107
ROI2	1.578	1.595	1.731	1.677
ROI3	1.547	1.572	0.767	0.781

6. FIBER ORIENTATION CHARACTERIZATION IN FIBER REINFORCED MATERIALS WITH X-RAY DARK-FIELD IMAGING

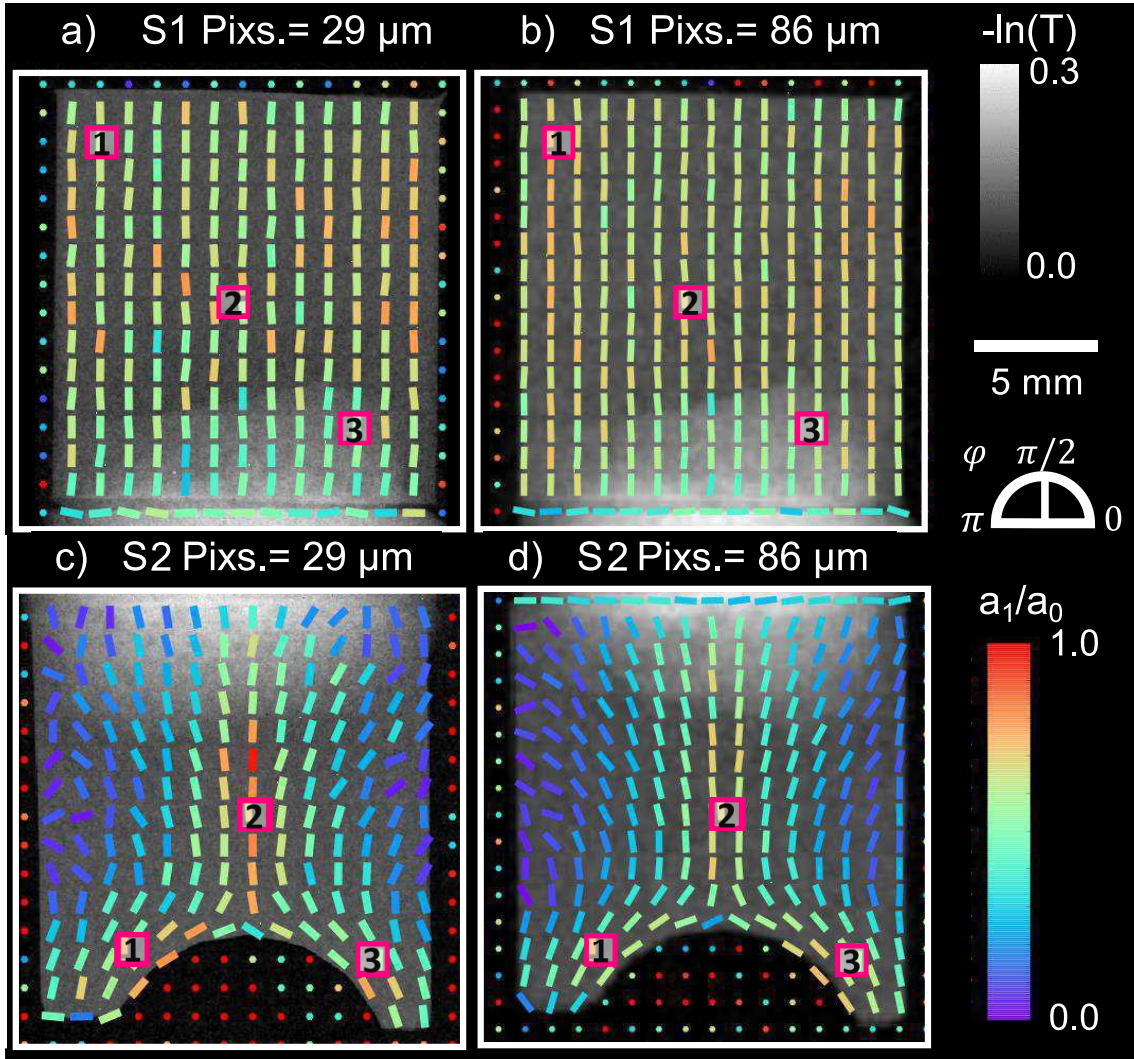


Figure 6.4.: This figure illustrates results of XVR measurements on samples $S1$ and $S2$. Images a-d) show an overlay of the sample's attenuation image (gray scale images) and the preferred fiber orientation (colored vectors) for samples $S1$ in images a) and b) and $S2$ in images c) and d) for two different pixel sizes. Injection direction was from bottom to top for both samples. The vector coloring corresponds to the anisotropy parameter $a_1/a_0 = 0$ (color bar on the right). Red vectors ($a_1/a_0 = 1$) correspond to regions where a large amount of fibers is oriented in the preferred direction, while purple vectors ($a_1/a_0 = 0$) correspond to regions where the amount of fibers oriented in the preferred direction is small. The half circle between the two color-bars illustrates how the parameter φ of equation 6.1 is translated into fiber orientation. The measurements acquired at different resolution emphasize that image resolution does not influence the determination of fiber orientation in XVR measurements.

6.2. MEASUREMENTS ON SHORT FIBER REINFORCED POLYMER COMPONENTS WITH X-RAY VECTOR RADIOGRAPHY

The preferred orientation φ is given in radians. The deviation of φ between the small and large pixel size is small in all the three regions for both samples. The fact that the resolution does not impact the orientation characterization is advantageous for the measurement of large samples. To emphasize this advantage, large SFRP samples were studied, and figure 6.5 shows results of XVR measurements on samples *L1*, *L2* and *L3*. These samples are considerably larger when compared to samples *S1* and *S2*. The glass fibers of sample *L1*, shown in figure 6.5 a), run preferably from top to bottom with a slight tilting along the sample's skewed edge. The other samples shown in figure 6.5 b) and c) have a more complex geometry and also contain a hole. As for sample *S2*, the melt had to flow around this hole during the molding process. In both cases, the fiber orientation appears to be very similar due to the same geometry of samples *L2* and *L3*. A weld-line is clearly extending vertically from the holes. While sample *L2* in image b) contained glass fibers, sample *L3* in image c) contained carbon fibers. Thus, our results show that fiber orientation can be studied with XVR even for fiber materials which are prone to weak attenuation contrast. Sample *L3* is barely visible in the underlying attenuation image in figure 6.5 c) indicating the weak attenuation properties of carbon fibers.

Table 6.2.: This table shows how the number of projections used for XVR influences the measurements. φ is given in radians for two random regions in the XVR data of sample *S2* acquired with a pixel size of $86 \mu\text{m}$.

Number of used images	Region 1	Region 2
31	2.213	0.662
16	2.210	0.676
7	2.185	0.694
4	1.328	0.951

A further advantage of XVR is its comparatively fast measurement time. For each of the presented measurements, 31 dark-field projections were acquired with a total measurement time of approximately 20 minutes. However, the time for one measurement can be reduced further when acquiring projections at fewer angles. To illustrate the feasibility of reducing the number of projections, we repeated the XVR analysis by constantly reducing the number of projections used for the orientation analysis. Table 6.2 shows the parameter φ in radians obtained for two random regions in sample *S2*, while using only 16, 7 and finally 4 of the originally 31 acquired projections. The parameter φ is relatively stable when the number of images is reduced. When using only 7 images, the value for φ varies only slightly from the initial value obtained with 31 images, while the variation increases strongly when less projections are used. Thus, the measurement time can even be reduced by a factor of 2 – 3 without losing accuracy in the orientation analysis.

6. FIBER ORIENTATION CHARACTERIZATION IN FIBER REINFORCED MATERIALS WITH X-RAY DARK-FIELD IMAGING

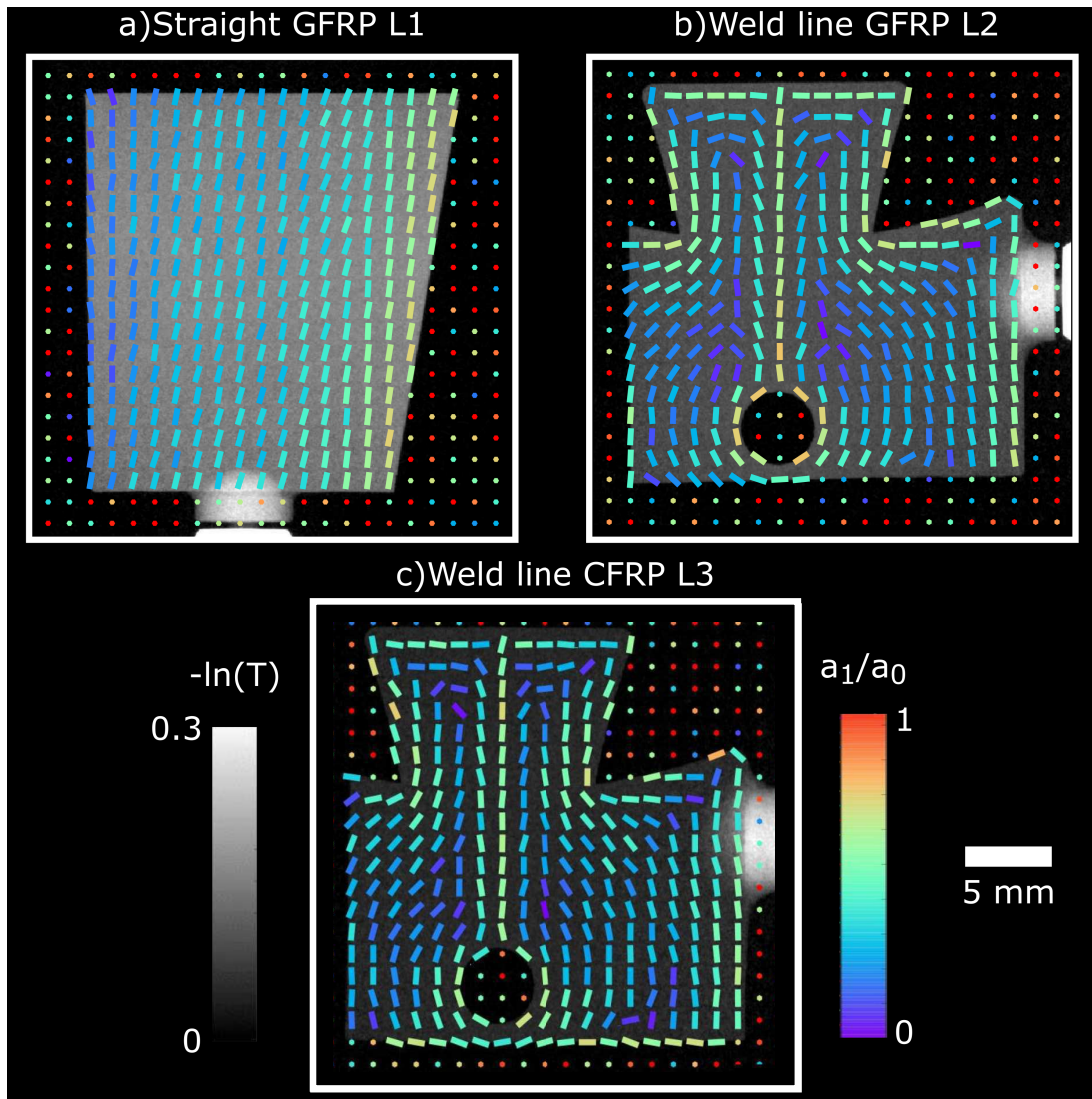


Figure 6.5.: This figure illustrates results of XVR measurements on samples $L1$, $L2$ and $L3$. The melt flow direction for all samples was from bottom to top. The images show an overlay of the attenuation images (shown in gray scale) and the preferred fiber orientation represented by colored vectors. The coloring of the vectors corresponds to the anisotropy parameters a_1/a_0 . While the fibers are running from top to bottom for $L1$ in image a), the fiber orientation has a complex appearance for the glass and carbon fiber samples $L2$ and $L3$ shown in images b) and c). Clearly, the fiber orientation in images b) and c) are very similar owing to the same sample geometry. It is important to note that the orientation measurement performs well also for the carbon fiber sample.

6.2. MEASUREMENTS ON SHORT FIBER REINFORCED POLYMER COMPONENTS WITH X-RAY VECTOR RADIOGRAPHY

Results from high-resolution attenuation-based imaging

In order to assure that the fiber orientation is recovered correctly by the XVR measurements, we qualitatively compare the results to μ CT measurements. High resolution radiographs of samples *S1* and *S2* are depicted in figure 6.6. For sample *S1*, the fiber orientation can be guessed from the high resolution images owing to the fact that most of the fibers are aligned in the same direction. For *S2*, only the weld-line and the region around the hole shows the preferred fiber orientation, while in other regions a preferred orientation is not observed. Figure 6.7 shows reconstructed slices from a μ CT measurement of samples *S1* in images a) and b) and *S2* in images c) and d). The slices of each sample were taken from close to the sample's surface in images a) and c) and from the sample's center in images b) and d).

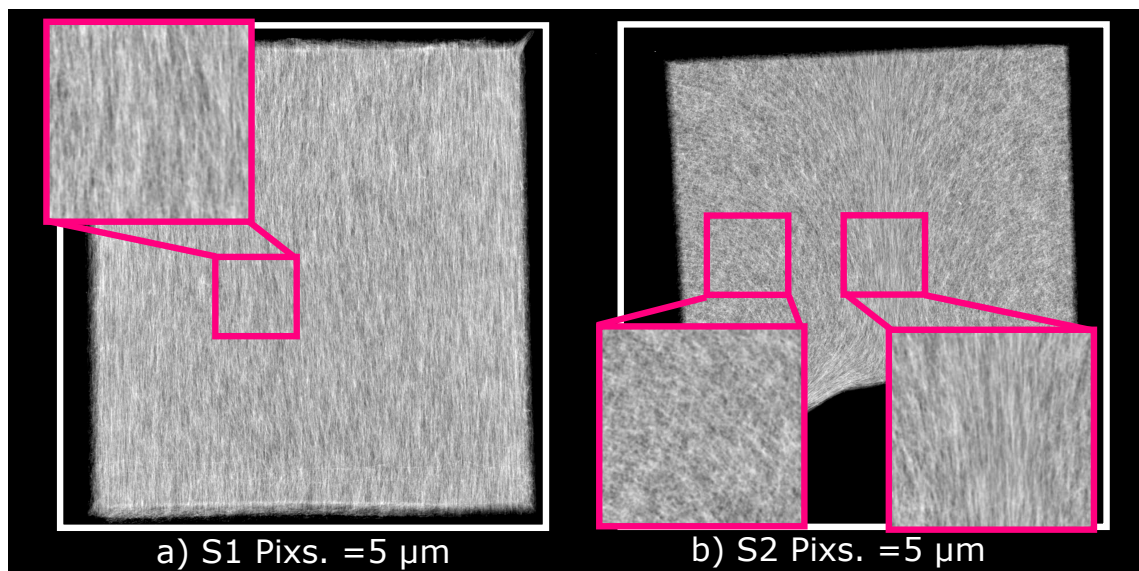


Figure 6.6.: This figure depicts high resolution attenuation projections of samples *S1* and *S2*. The fiber orientation is barely detectable in these high resolution projections of sample *S1* in image a) and *S2* in image b). This indicates that simple attenuation-based imaging is insufficient for fiber orientation studies.

Fibers are spatially resolved in the μ CT measurements due to the small pixel size of $6.5 \mu\text{m}$. Fibers appear to be rather randomly oriented close to the surface of both samples shown in images a) and c). However, the weld-line in sample *S2* is already observable as indicated by the dashed rectangle in figure 6.7 c). The central slice through the sample in figure 6.7 b) reveals a fiber orientation from top to bottom for sample *S1*. This is in good qualitative agreement with observations made with XVR scans shown in figure 6.4. The central slice through sample *S2* in figure 6.7 d) also reveals a similar orientation distribution as shown in figure 6.4. While fibers are aligned around the hole, they also form a weld-line shown by the dashed rectangle. Fibers fan out on the left and right hand

6. FIBER ORIENTATION CHARACTERIZATION IN FIBER REINFORCED MATERIALS WITH X-RAY DARK-FIELD IMAGING

side of this weld-line.

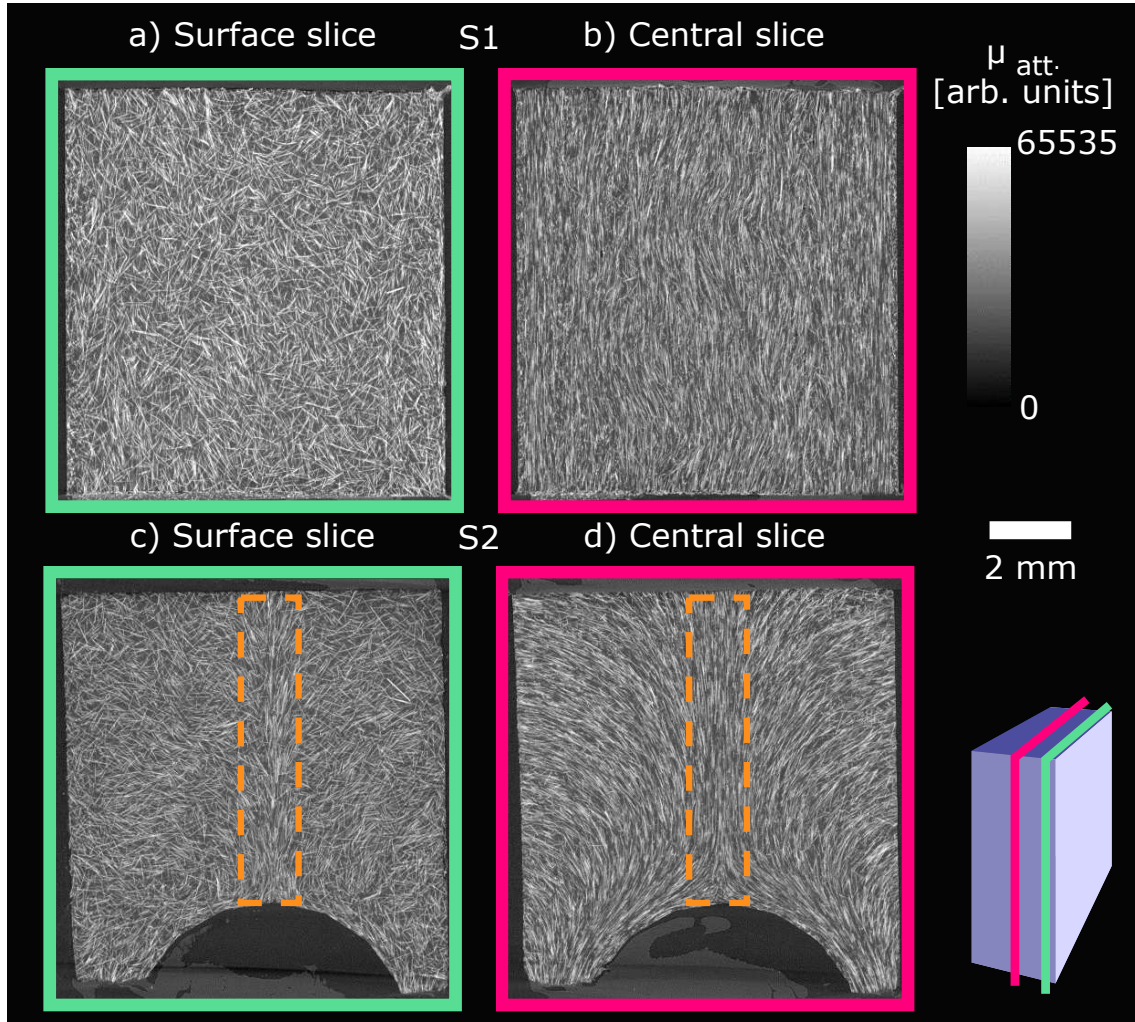


Figure 6.7.: This figure depicts slices from high resolution CT measurements of samples *S1* and *S2*. Images a) and c) represent slices through the center of the samples, while images b) and d) represent slices close to the samples surface. The location of the slices is also indicated by the colored frames and the small cube at the bottom right of this figure. While fibers appear to be oriented randomly close to the surface of sample *S1*, they are very strongly aligned from top to bottom in the central slice. The fiber orientation in *S2* is strongly influenced by the hole. The so-called weld-line indicated by the orange dashed rectangles can be observed in both slices.

Thus, we can qualitatively assure that the orientation obtained from the XVR measurement corresponds to the sample's preferred fiber orientation. It is important to mention that XVR measurements provide the preferred fiber orientation as an average throughout

6.2. MEASUREMENTS ON SHORT FIBER REINFORCED POLYMER COMPONENTS WITH X-RAY VECTOR RADIOGRAPHY

the sample's thickness. Not all fibers are oriented in this direction. This is emphasized by the parameter a_1/a_0 giving the degree of anisotropy.

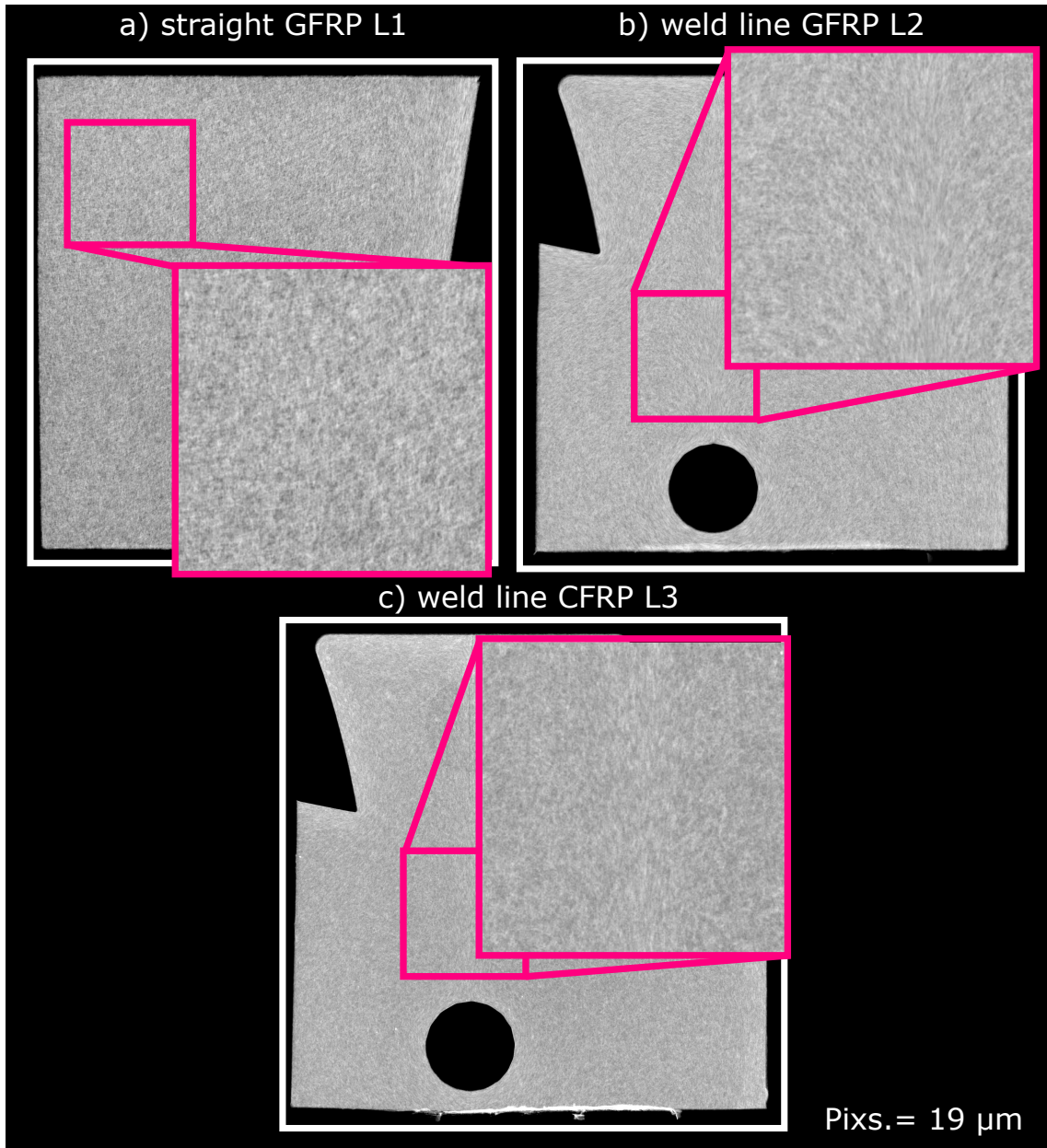


Figure 6.8.: This figure depicts high resolution attenuation projections of samples $L1$, $L2$ and $L3$. Fiber orientation cannot be determined from these attenuation based images. A high resolution μ CT measurement was not feasible in this case due to the size of the samples.

The colored representation of this parameter is also in good agreement with the μ CT

6. FIBER ORIENTATION CHARACTERIZATION IN FIBER REINFORCED MATERIALS WITH X-RAY DARK-FIELD IMAGING

data. Fibers are aligned along the weld-line throughout the whole sample $S2$ resulting in large values for a_1/a_0 as shown in images c) and d) in figure 6.4. On the left and right hand side of the weld-line, fibers are aligned along the extracted orientation only within the central slice. Close to the surface they are more randomly orientated, thus, resulting in small values for a_1/a_0 on the left and right hand side of the weld-line (see figure 6.4).

Figure 6.8 shows high resolution radiographs of the large samples $L1$, $L2$ and $L3$. The fiber orientation cannot be determined based on these simple projections. In this case, the sample's size only allowed for a pixel size of $19 \mu\text{m}$. Therefore, a μCT measurement was not feasible as it would not have been possible to resolve single fibers.

6.3. Summary and discussion

The advantages of XVR over μCT measurements are pointed out by the presented results. While XVR measurements and their analysis can be conducted much faster than μCT measurements, they also do not suffer from the sample's physical dimension as a limiting factor, which is the case for μCT measurements. For μCT , sample sizes are limited to a few millimeters to achieve a spatial resolution sufficient for resolving single fibers. In contrast, samples can be of a size of several centimeters for XVR measurements. As already mentioned, this stems from the origin of the dark-field signal as it is based on X-ray scattering caused by the sample's microstructure. To detect this scattering signal, high resolution is not required. One limiting factor concerning the sample size in XVR is the maximum area of the gratings that currently can be produced.

The comparison of μCT to XVR data is only addressed on a qualitative level in this work. However, a quantitative correlation of both techniques has been shown before by several other studies [32, 120]. One drawback of XVR certainly is the two-dimensionality of the obtained data. Thus, samples studied by XVR should ideally be flat objects. The fiber orientation distribution of such samples lies within the two dimensions probable by XVR. However, also flat objects might already show varying fiber orientation distributions in different layers as revealed by the μCT data on samples $S1$ and $S2$. XVR cannot differentiate such variations as it probes the averaged orientation from all overlaying layers of the sample. Therefore, samples should be chosen carefully when applying XVR to characterize them. A possible solution for this is the extension of XVR into three dimensions, which is referred to as X-ray tensor tomography (XTT) [42, 121]. This experimental method has been developed recently and provides information on the fiber orientation in three dimensions. Of course it is important to mention, that XTT measurements take several hours, which is a similar amount of time as for μCT measurements. But fiber orientation distributions can be readily studied in relatively large objects (several centimeters) with arbitrary geometries on a reasonable time scale with XTT.

Besides the fiber orientation, we pointed out, that parameters a_0 and a_1 are related to

the total amount of fibers in each pixel and the amount of fibers aligned in the preferred direction φ , respectively. However, the fiber length distribution, which is a very important parameter especially for SFRP components, cannot be addressed by neither XVR nor XTT. Further work has to be carried out to obtain a quantitative relation of parameters a_0 , a_1 , and a_1/a_0 to the actual physical quantities characterizing the sample such as fiber content for example.

7. Summary and outlook

This final chapter summarizes the presented results, states open questions and gives an outlook to future developments of X-ray dark-field imaging.

7.1. Summary

The potential of grating-based X-ray dark-field imaging as a new imaging modality in materials research and NDT was demonstrated by means of specific application examples. Besides providing strong imaging contrast for microstructural features, the dark-field signal also provides quantitative information about structural parameters. We pointed out this capability by deriving a theoretical framework for the dark-field signal, which is based on well-known mathematical formalism of SAXS. Our theoretical considerations provide a direct relation of the dark-field signal to the auto-correlation function of the sample's microstructure. By using model functions, quantitative information on the sample's microstructure is extracted based on the dark-field signal. We further developed an experimental method which allows to measure such auto-correlation functions with laboratory-based X-ray equipment and a Talbot-Lau interferometer setup. Experiments with SiO_2 microspheres were carried out to validate our theoretical dark-field framework as well as to demonstrate the feasibility of our experimental approach. Here, the microsphere's diameter was determined with good accuracy when compared to the manufacturer's specifications. In addition to that, short-range ordering in dense sphere suspensions was observed, and the next neighbor distance of spheres was qualitatively determined.

We further utilized the dark-field signal's sensitivity to microstructural features to study different materials. At first, building materials such as mortar and cement were studied. Here, we presented methods for time-resolved radiography and tomography experiments and applied these techniques to study water transport in porous materials. Our results showed that temperature treatment of mortar samples influences the material's water sorptivity. Mortar that was treated at higher temperatures takes up water faster than untreated mortar due to an increased amount of microcracks in the heated samples. Further results revealed that water adsorption in mortar can be prevented by adding hydrophobic substances such as biofilm to the mortar during mixing. Water transport is observed with strong contrast by X-ray dark-field imaging because the intrusion of water strongly changes the scattering properties of a porous material such as mortar. Besides two-dimensional dark-field radiography, we used time-resolved dark-field CT to study water

7. SUMMARY AND OUTLOOK

transport in three dimensions. Here, water supply to cement by porous water-saturated limestone grains during cement hardening was presented.

Grating-based X-ray dark-field imaging was further demonstrated to be a valuable tool for studies on cement during setting and hardening. The microstructural changes in cement paste affects the material's scattering properties. Thus, grating-based dark-field imaging was used to study kinetics of cement hydration spatially resolved in two as well as three dimensions. The change in dark-field signal of pure cement paste was found to follow a logistic behavior similar to ultrasound measurements[78]. Temperature variations were shown to have a strong effect on the dark-field measurements because the chemical reactions causing cement hardening are temperature sensitive. While a heated cement sample shows increased reaction speed, a cooled sample displays reduced reaction speed, which is correspondingly reflected in the measured dark-field signal.

Another material class, which was studied in this work, are short fiber reinforced polymer components. Here, the orientation sensitivity of a Talbot-Lau interferometer for scattered X-rays was exploited to study fiber orientation in flat SFRP samples. Fiber orientation was analyzed by XVR measurements for samples with different geometry and fiber materials. A qualitative comparison revealed good correlation of the average structure orientation measured by XVR in each pixel and the real fiber orientation provided by μ CT. XVR was furthermore shown to be much faster than conventional CT measurements, and it also provides sufficient contrast between carbon fibers and a carbon-based matrix to allow for orientation characterization.

7.2. Outlook

The presented application examples have illustrated the potential of grating-based X-ray dark-field imaging as a valuable tool for materials research and NDT. Grating-based X-ray dark-field imaging complements standard X-ray imaging, as it reduces the accessible structure size towards the nanometer length scale also for large objects. grating-based X-ray dark-field imaging may therefore be beneficial for studies in particular on slow dynamical processes related to microstructural changes. Often, the probed sample volume sets boundary conditions which influence these microstructural processes. Small sample volumes often need dedicated preparation protocols, for example in electron and X-ray microscopy. As dark-field imaging allows to study relatively large sample volumes, while being sensitive to microstructural changes, the sample size is less restricted making in-situ experiments feasible. Research areas where such a method is potentially of great interest may include: Geological sciences, where water transport in geological materials is of interest, energy sciences, where structural processes in battery materials come more into focus with the rise of electrical mobility, and for example civil engineering,

where the need for sustainable and durable materials shifts the research focus towards the micrometer length scale. Besides qualitative studies, which benefit from the dark-field signals improved contrast for microstructures, even quantitative studies are feasible. While quantitative studies are straight forward for simple structures such as microspheres, much more research is needed in order to extract quantitative information from dark-field measurements on complex materials such as cement. Furthermore, some technological barriers limit the application of quantitative dark-field imaging nowadays. The probable object size is currently limited because large area gratings are not available in great numbers. This limits the field of view of most grating-based imaging systems to a few centimeters. High energy applications further demand gratings with high aspect ratios of material height to grating period to provide sufficient X-ray attenuation by the source and analyzer gratings. Interferometers working at mean X-ray spectrum energies of around 50 keV are easily realizable at the time, while interferometers working at energies towards and beyond 100 keV remain rare systems for now. A crucial aspect for quantitative measurements is also the period of the grating structures. Currently available grating periods limit the maximum structure size that can be quantified to $2.5 - 5 \mu\text{m}$ [60]. To substantially increase this length scale, smaller grating periods are necessary. Gratings of small period are more sensitive to small scattering angles which originate from structural features with a size of a few micrometers. Due to the emergence of micro-manufacturing and additive manufacturing, structures on a length scale of 100 nm up to 100 μm in large objects of several centimeters in size become more and more interesting to the research and engineering community [122–126]. Here, quantitative grating-based X-ray dark-field imaging has a lot potential to assist in characterization of materials and manufacturing processes.

Appendix A.

Detailed derivation of equations from chapter 4

A.1. Calculations for equation 4.24

In order to derive equation 4.24, we start with the third term of equation 4.22 using equation 4.25 and split the integration over Q_x into a negative and positive part.

$$\begin{aligned}
 T_3 &= \int_{-\infty}^{\infty} \frac{d\sigma}{d\Omega} (Q_x) \cos \left[\frac{2\pi}{p_2} \left(x_D + \frac{\lambda Q_x d_{S,G_2}}{2\pi} \right) \right] dQ_x \\
 &= - \int_0^{-\infty} \frac{d\sigma}{d\Omega} (Q_x) \cos \left[\frac{2\pi}{p_2} \left(x_D + \frac{\lambda Q_x d_{S,G_2}}{2\pi} \right) \right] dQ_x \\
 &\quad + \int_0^{\infty} \frac{d\sigma}{d\Omega} (Q_x) \cos \left[\frac{2\pi}{p_2} \left(x_D + \frac{\lambda Q_x d_{S,G_2}}{2\pi} \right) \right] dQ_x \tag{A.1}
 \end{aligned}$$

Assuming the differential scattering cross section to be a real and even function, i.e. $\frac{d\sigma}{d\Omega} (Q_x) = \frac{d\sigma}{d\Omega} (-Q_x)$, we get rid of the minus before the first term of equation A.1 and its integration limits by writing $Q_x = -Q_x$. By further using the identity of equation 4.23 we end up with the following representation for the third term of equation 4.22.

$$\begin{aligned}
 T_3 &= \int_0^{\infty} \frac{d\sigma}{d\Omega} (-Q_x) \cos \left[\frac{2\pi}{p_2} \left(x_D - \frac{\lambda Q_x d_{S,G_2}}{2\pi} \right) \right] dQ_x \\
 &\quad + \int_0^{\infty} \frac{d\sigma}{d\Omega} (Q_x) \cos \left[\frac{2\pi}{p_2} \left(x_D + \frac{\lambda Q_x d_{S,G_2}}{2\pi} \right) \right] dQ_x \\
 &= 2 \cos \left[\frac{2\pi}{p_2} x_D \right] \int_0^{\infty} \frac{d\sigma}{d\Omega} (Q_x) \cos \left[\frac{\lambda d_{S,G_2}}{p_2} Q_x \right] dQ_x \tag{A.2}
 \end{aligned}$$

The final integration can be written as a sum of two identical integrals and we can reintroduce the integration over the negative Q_x -space again by setting $Q_x = -Q_x$ in one of

the two identical integrations. This is feasible because $\cos\left[\frac{\lambda d_{S,G_2}}{p_2}Q_x\right] = \cos\left[\frac{-\lambda d_{S,G_2}}{p_2}Q_x\right]$ and because we assume the same to be true for the differential scattering cross section, i.e. $\frac{d\sigma}{d\Omega}(Q_x) = \frac{d\sigma}{d\Omega}(-Q_x)$.

$$\begin{aligned}
T_3 &= 2 \cos\left[\frac{2\pi}{p_2}x_D\right] \int_0^\infty \frac{d\sigma}{d\Omega}(Q_x) \cos\left[\frac{\lambda d_{S,G_2}}{p_2}Q_x\right] dQ_x \\
&= \cos\left[\frac{2\pi}{p_2}x_D\right] \left[\int_0^\infty \frac{d\sigma}{d\Omega}(Q_x) \cos\left[\frac{\lambda d_{S,G_2}}{p_2}Q_x\right] dQ_x \right. \\
&\quad \left. + \int_0^\infty \frac{d\sigma}{d\Omega}(Q_x) \cos\left[\frac{\lambda d_{S,G_2}}{p_2}Q_x\right] dQ_x \right] \\
&= \cos\left[\frac{2\pi}{p_2}x_D\right] \left[\int_0^\infty \frac{d\sigma}{d\Omega}(Q_x) \cos\left[\frac{\lambda d_{S,G_2}}{p_2}Q_x\right] dQ_x \right. \\
&\quad \left. + \int_{-\infty}^0 \frac{d\sigma}{d\Omega}(Q_x) \cos\left[\frac{\lambda d_{S,G_2}}{p_2}Q_x\right] dQ_x \right] \\
&= \cos\left[\frac{2\pi}{p_2}x_D\right] \int_{-\infty}^\infty \frac{d\sigma}{d\Omega}(Q_x) \cos\left[\frac{\lambda d_{S,G_2}}{p_2}Q_x\right] dQ_x \tag{A.3}
\end{aligned}$$

A.2. Impact of a polychromatic X-ray spectrum on equation 4.27

First we rewrite the term of the reference intensity pattern I_r from equation 4.19 in chapter 4 for a polychromatic X-ray spectrum:

$$I_r(\lambda, x_D) = I_0(\lambda)a_0(\lambda) + I_0(\lambda)a_1(\lambda) \cos \left[\frac{2\pi}{p_2} x_D \right] \quad (\text{A.4})$$

Here, $I_0(\lambda)$ is the incoming intensity at a certain energy λ and the parameters $a_0(\lambda)$ and $a_1(\lambda)$ describe the mean and amplitude of the periodic reference pattern generated by this incoming intensity. Integration of equation A.4 over the full energy range of the spectrum yields the total observed reference pattern:

$$I_r(x_D) = \int_0^\infty I_0(\lambda)a_0(\lambda)d\lambda + \int_0^\infty I_0(\lambda)a_1(\lambda) \cos \left[\frac{2\pi}{p_2} x_D \right] d\lambda \quad (\text{A.5})$$

Same considerations are true for the reference pattern observed with a sample interacting with the X-rays. In this case, we integrate the energy dependent superposition of scattered and un-scattered intensity patterns over the full energy range which yields following equation:

$$\begin{aligned} I_{tot}(\lambda, x_D) &= \int_0^\infty (I_0(\lambda) - \sigma(\lambda)I_0(\lambda)t) \left(a_0(\lambda) + a_1(\lambda) \cos \left[\frac{2\pi}{p_2} x_D \right] \right) d\lambda \\ &\quad + t \int_0^\infty I_0(\lambda)a_0(\lambda)\sigma(\lambda)d\lambda \\ &\quad + t \cos \left[\frac{2\pi}{p_2} x_D \right] \int_0^\infty I_0(\lambda)a_1(\lambda)G(\xi(\lambda))d\lambda \end{aligned} \quad (\text{A.6})$$

With equation A.5 and A.6 we can write the dark-field signal obtained for a polychromatic X-ray beam as follows:

$$\begin{aligned} DF &= \frac{\int_0^\infty I_0(\lambda)a_1(\lambda) [1 - \sigma(\lambda)t + \sigma(\lambda)tG(\xi(\lambda))] d\lambda \int_0^\infty I_0(\lambda)a_0(\lambda)d\lambda}{\int_0^\infty I_0(\lambda)a_0(\lambda)d\lambda \int_0^\infty I_0(\lambda)a_1d\lambda} \\ &= \frac{\int_0^\infty I_0(\lambda)a_1(\lambda) [1 - \sigma(\lambda)t + \sigma(\lambda)tG(\xi(\lambda))] d\lambda}{\int_0^\infty I_0(\lambda)a_1d\lambda} \\ &= 1 - t \frac{\int_0^\infty I_0(\lambda)a_1(\lambda)\sigma(\lambda)d\lambda}{\int_0^\infty I_0(\lambda)a_1(\lambda)d\lambda} + t \frac{\int_0^\infty I_0(\lambda)a_1(\lambda)\sigma(\lambda)G(\xi(\lambda))d\lambda}{\int_0^\infty I_0(\lambda)a_1(\lambda)d\lambda} \end{aligned} \quad (\text{A.7})$$

Equation A.7 resembles the first line of equation 4.27 in chapter 4 for a polychromatic spectrum. It therefore maintains the relation of the dark-field signal and the correlation function $G(\xi)$ but includes energy weighting terms that account for a polychromatic X-ray spectrum. Our experimental results have shown that it is feasible to account for this energy weighting by assuming that the Talbot-Lau interferometer operates at the mean energy for spectra of conventional X-ray tubes.

Appendix B.

Additional figures for chapters 4 and 5

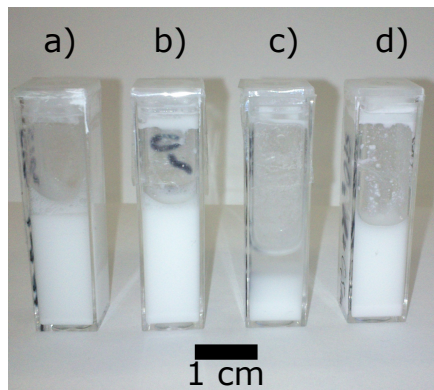


Figure B.1.: This photograph shows the suspension samples of monodisperse microspheres with diameters of $D = 0.513$ (a), $D = 0.966$ (b), $D = 7.38$ (c) and $2.79 \mu\text{m}$ (d), which are used in chapter 4. The spheres with the largest diameter in image c) already settle on the bottom of the cuvettes.

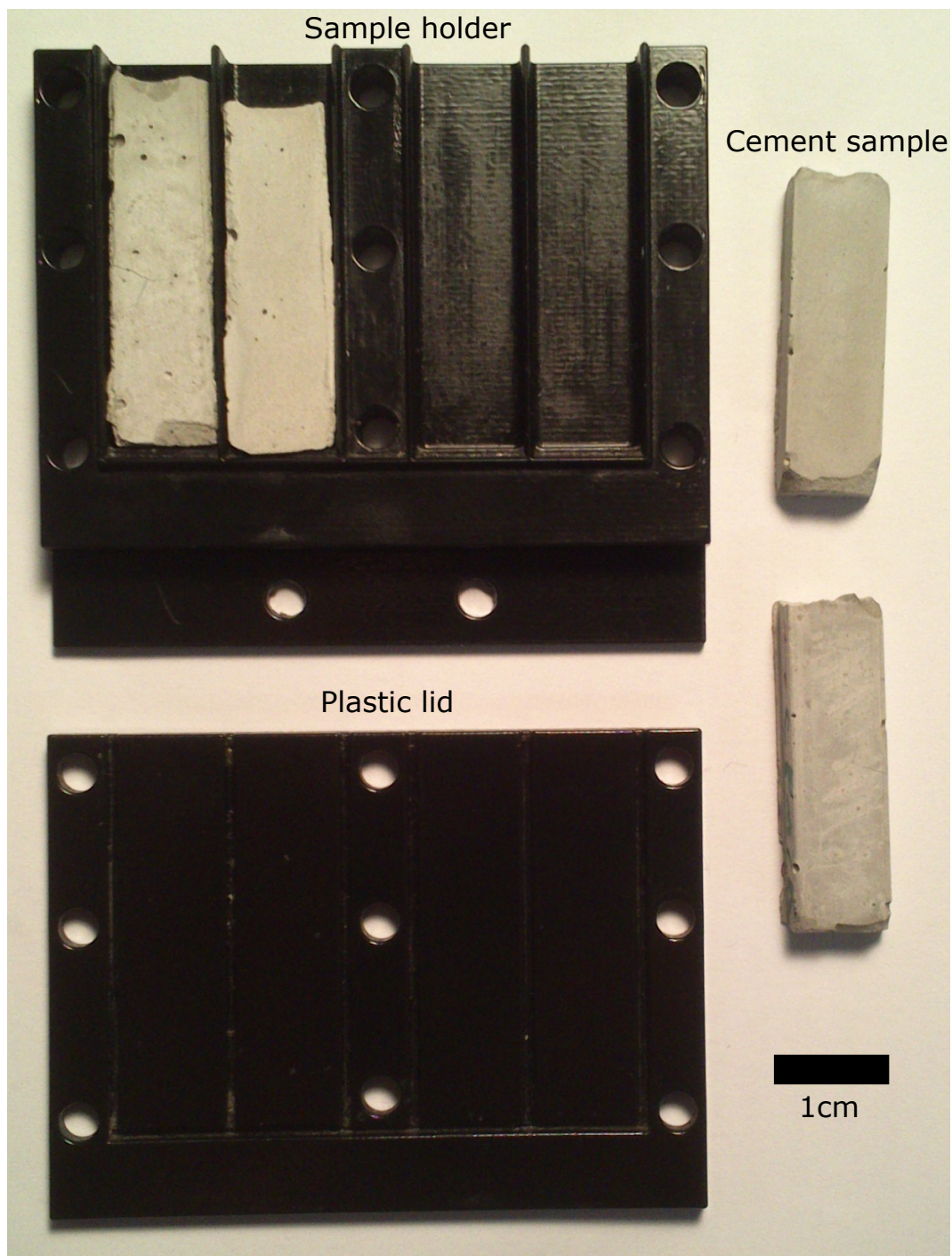


Figure B.2.: This photograph shows the the cement sample holder and some cement samples used for dark-field radiography studies presented in chapter 5.

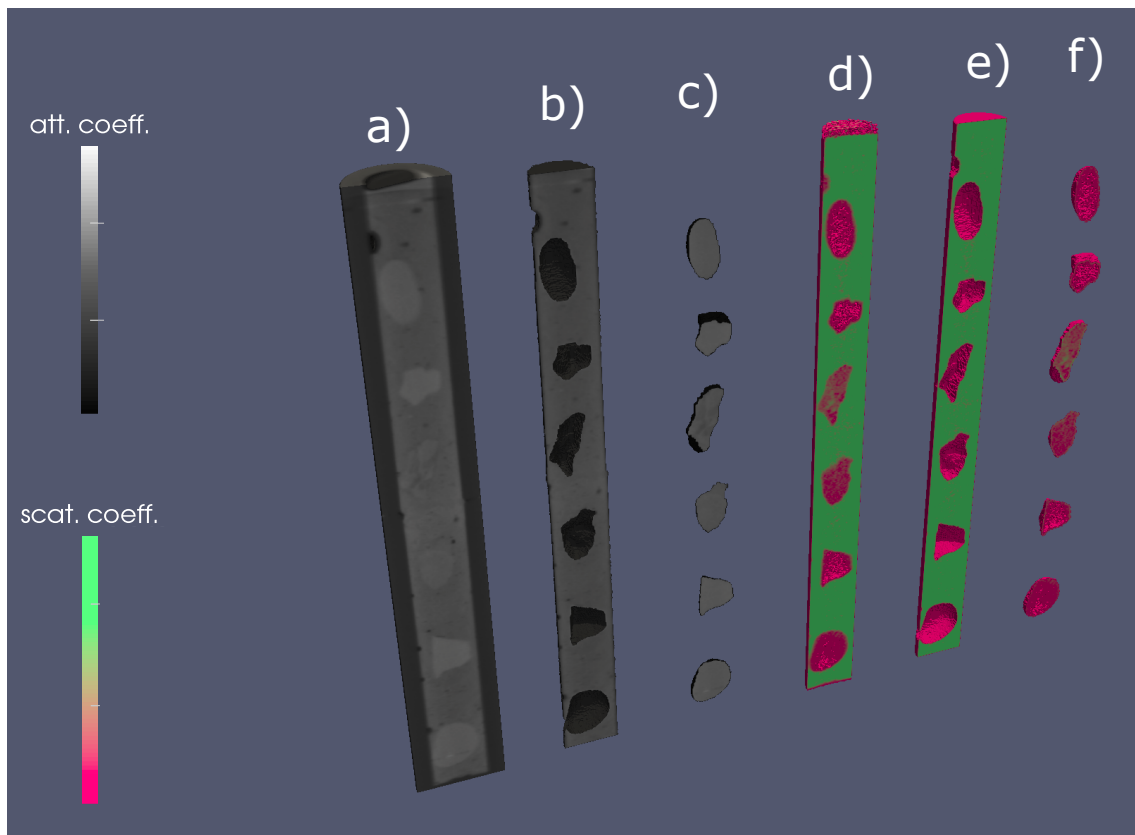


Figure B.3.: This figure illustrates the result of the segmentation performed on the time-resolved tomography data of fresh cement paste and limestone grains presented in chapter 5, section 5.6. Volumes a) and d) show half of the reconstructed volume for the attenuation and scattering coefficient, respectively. The volumes b) and e) show the segmented cement volume of the attenuation and scattering coefficient, respectively. The segmentation of the six tested limestone grains is shown by volumes c) and f) for the attenuation and scattering coefficient, respectively. The segmentation is based on a simple threshold segmentation performed on the volume of the scattering coefficient reconstructed at time 0 h.

List of Tables

3.1. Specifications of the three gratings used in this study	34
3.2. Specifications of the new phase and source gratings used in this work.	35
5.1. Chemical composition of the Portland cement used in this work	74
6.1. Influence of the effective pixel size on the fiber orientation characterization with XVR	107
6.2. Reducing the number of projections in XVR measurements and the influ- ence on orientation characterization	109

List of Figures

1.1. Suitable sample size compared to accessible length scale of structural information for several X-ray techniques	3
2.1. Schematic representation of the longitudinal coherence length	10
2.2. Schematic representations of the transverse coherence length	11
2.3. Illustration of elastic X-ray scattering and X-ray refraction	13
2.4. Schematic illustration of Compton scattering and X-ray absorption	15
2.5. Geometrical sample magnification in X-ray imaging	18
2.6. Talbot-carpet generated by a phase grating	20
2.7. Schematic illustration of the source grating's purpose	21
2.8. Analyzing intensity profiles by phase-stepping	23
2.9. Transmittance image of a cup of cappuccino	25
2.10. DPC image of a cup of cappuccino	26
2.11. Dark-field image of a cup of cappuccino	28
3.1. 3D rendering of the experimental setup	32
3.2. Visibility maps of the optimized experimental setup	36
4.1. Schematic illustration of the differential scattering cross-section	39
4.2. Scattering by two electrons and a geometrical representation of the scattering vector \vec{Q}	40
4.3. Schematic representation of scattering by a continuous electron distribution	41
4.4. Experimental setup for spin-echo small-angle neutron scattering experiments	45
4.5. Layout of a Talbot-Lau interferometer with its reference pattern and the pattern of scattered X-rays	47
4.6. Split beam of a grating interferometer scanning the sample	51
4.7. Experimental approach for measurements of correlation functions with a laboratory-based X-ray grating interferometer	52
4.8. Transmittance images of SiO_2 microsphere suspensions at different sample positions	53
4.9. Dark-field images of SiO_2 microsphere suspensions at different sample positions	54
4.10. Mean dark-field signal of a microsphere suspension plotted against the correlation length and fitted by a corresponding correlation function	55
4.11. Graphical interpretation of a sphere's correlation function	56

4.12. Mean dark-field signal of monodisperse microsphere suspensions	57
4.13. Mean dark-field signal of dense suspensions of monodisperse microspheres with different diameters	58
4.14. Graphical description of the correlation function of a dense sphere suspension	59
4.15. Registered dark-field images of a microsphere suspension used for quanti- tative imaging	60
4.16. Overlay of a quantitative dark-field image and the corresponding transmit- tance image	61
5.1. Schematic illustration of the experimental setup for water sorptivity studies of porous materials	69
5.2. Transmittance and difference images of three temperature treated mortar samples submerged in water	70
5.3. Dark-field and difference images of three temperature treated mortar samp- les submerged in water	71
5.4. Dark-field and difference images of two unmodified mortar and two biofilm- modified mortar samples	73
5.5. Particle size distribution of the cement powder used in this work	75
5.6. Experimental setup for time-resolved dark-field radiography on fresh ce- ment paste	76
5.7. Transmittance images of an exemplary fresh cement paste sample	77
5.8. Dark-field images of an exemplary experiment on fresh cement paste	77
5.9. Evolution of the attenuation and scattering coefficient of fresh cement paste	78
5.10. Schematic illustration of the microstructural processes in cement paste . . .	80
5.11. Dark-field images of fresh cement paste treated at different temperatures during the experiment	83
5.12. Evolution of the scattering coefficient of fresh cement paste under different temperature conditions	84
5.13. Influence of limestone grains on the scattering signal of fresh cement paste	86
5.14. Schematic illustration of a pixel-wise logistic fit to a time series of dark-field images of fresh cement paste	87
5.15. Image representation of the scattering coefficient's fitting parameters of fresh cement paste containing limestone grains	88
5.16. Image representation of the scattering coefficients fitting parameters of fresh cement paste containing limestone grains from a second experiment . . .	89
5.17. Experimental setup for tomographic measurements of a cement sample . . .	91
5.18. Transmittance and dark-field images of the tomography experiment	94
5.19. Reconstruction of the attenuation and scattering coefficient for a cement sample containing six limestone grains	95
5.20. Scattering and attenuation coefficients of limestone grains and cement paste calculated from the tomographic data	96
5.21. PLM images of a thin section of each limestone grain	97

5.22. SEM images of a thin section of each limestone grain acquired with high magnification	98
5.23. SEM images of each limestone grain acquired with low magnification	99
6.1. Photograph of the SFRP samples studied by XVR	103
6.2. Schematic illustration of an XVR measurement	104
6.3. Dark-field images of sample <i>S2</i> acquired at different orientations	106
6.4. XVR measurements on small SFRP samples	108
6.5. XVR measurements on large SFRP samples	110
6.6. High resolution attenuation projections of small SFRP samples	111
6.7. High resolution CT data of small SFRP samples	112
6.8. High resolution attenuation projections on large SFRP samples	113
B.1. Photograph of the monodisperse microsphere suspension samples	124
B.2. Photograph of the cement sample holder and some cement samples	125
B.3. Segmentation of a tomography of fresh cement containing limestone grains	126

Abbreviations

- CFRP** Carbon fiber reinforced polymer
- CT** Computed tomography
- DPC** Differential phase contrast
- FBP** Filtered backprojection
- GFRP** Glass fiber reinforced polymer
- μ CT** Micro-tomography
- NDT** Non-destructive testing
- PLM** Polarized light microscopy
- PSF** Point spread function
- ROI** Region of interest
- SAXS** Small-angle X-ray scattering
- SEM** Scanning electron microscopy
- SESANS** Spin-echo small-angle neutron scattering

SFRP Short fiber reinforced polymer

w/c-ratio Water to cement ratio of a cement paste in terms of mass

XTT X-ray tensor tomography

XVR X-ray vector radiography

Bibliography

- [1] W. C. Röntgen. "Ueber eine neue Art von Strahlen". In: *Annalen der Physik* 300 (1898). DOI: 10.1002/andp.18983000102.
- [2] A. M. Cormack. "Representation of a function by its line integrals, with some radiological applications". In: *Journal of Applied Physics* 34 (1963). DOI: 10.1063/1.1729798.
- [3] G. N. Hounsfield. "Computerized transverse axial scanning (tomography): Part 1. Description of system". In: *British Journal of Radiology* 46 (1973). DOI: 10.1259/0007-1285-46-552-1016.
- [4] B. P. Flannery, H. W. Deckman, W. G. Roberge, and K. L. D'amico. "Three-dimensional X-ray microtomography". In: *Science* 237 (1987). DOI: 10.1126/science.237.4821.1439.
- [5] A. Sasov and D. Van Dyck. "Desktop X-ray microscopy and microtomography". In: *Journal of Microscopy* 191 (1998). DOI: 10.1046/j.1365-2818.1998.00367.x.
- [6] J. Hsieh. *Computed tomography principles, design, artifacts, and recent advances*. John Wiley & Sons, Inc., 2009. DOI: 10.1117/3.2197756.
- [7] P. J. Withers. "X-ray nanotomography". In: *Materials Today* 10 (2007). DOI: 10.1016/S1369-7021(07)70305-X.
- [8] J. Miao, P. Charalambous, J. Kirz, and D. Sayre. "Extending the methodology of X-ray crystallography to allow imaging of micrometre-sized non-crystalline specimens". In: *Nature* 400 (1999). DOI: 10.1038/22498.
- [9] P. Thibault et al. "High-resolution scanning X-ray diffraction microscopy". In: *Science* 321 (2008). DOI: 10.1126/science.1158573.
- [10] W. Friedrich, P. Knipping, and M. Laue. "Interferenzerscheinungen bei Röntgenstrahlen". In: *Annalen der Physik* 346 (1913). DOI: 10.1002/andp.19133461004.
- [11] J. C. Kendrew et al. "A three-dimensional model of the myoglobin molecule obtained by X-Ray analysis". In: *Nature* 181 (1958). DOI: 10.1038/181662a0.
- [12] O. Glatter and O. Kratky. *Small-angle X-ray scattering*. Academic Press, 1982. ISBN: 9780122862809.
- [13] M. N. Wernick et al. "Multiple-image radiography". In: *Physics in Medicine and Biology* 48 (2003). DOI: 10.1088/0031-9155/48/23/006.

- [14] U. Bonse and M. Hart. "**An X-Ray Interferometer**". In: *Applied Physics Letters* 6 (1965). DOI: 10.1063/1.1754212.
- [15] D. Chapman et al. "**Diffraction enhanced x-ray imaging**". In: *Physics in Medicine and Biology* 42 (1997). DOI: 10.1088/0031-9155/42/11/001.
- [16] T. J. Davis et al. "**Phase-contrast imaging of weakly absorbing materials using hard X-rays**". In: *Nature* 373 (1995). DOI: 10.1038/373595a0.
- [17] A. Snigirev et al. "**On the possibilities of x-ray phase contrast microimaging by coherent high-energy synchrotron radiation**". In: *Review of Scientific Instruments* 66 (1995). DOI: 10.1063/1.1146073.
- [18] A. Momose. "**Phase-sensitive imaging and phase tomography using X-ray interferometers**". In: *Optics Express* 11 (2003). DOI: 10.1364/oe.11.002303.
- [19] C. David, B. Nöhammer, H. H. Solak, and E. Ziegler. "**Differential x-ray phase contrast imaging using a shearing interferometer**". In: *Applied Physics Letters* 81 (2002). DOI: 10.1063/1.1516611.
- [20] T. Weitkamp et al. "**X-ray phase imaging with a grating interferometer**". In: *Optics Express* 13 (2005). DOI: 10.1364/opex.13.006296.
- [21] H.F.Talbot. "**LXXVI. Facts relating to optical science. No. IV**". In: *Philosophical Magazine Series 3* 9 (1836). DOI: 10.1080/14786443608649032.
- [22] P. Cloetens et al. "**Observation of microstructure and damage in materials by phase sensitive radiography and tomography**". In: *Journal of Applied Physics* 81 (1997). DOI: 10.1063/1.364374.
- [23] F. Pfeiffer, O. Bunk, and C. David. "**Phase retrieval and differential phase-contrast imaging with low-brilliance X-ray sources**". In: *Nature Physics* 2 (2006). DOI: 10.1038/nphys265.
- [24] F. Pfeiffer et al. "**Hard-X-ray dark-field imaging using a grating interferometer**". In: *Nature Materials* 7 (2008). DOI: 10.1038/nmat2096.
- [25] W. Yashiro, Y. Terui, K. Kawabata, and A. Momose. "**On the origin of visibility contrast in x-ray Talbot interferometry**". In: *Optics Express* 18 (2010). DOI: 10.1364/oe.18.016890.
- [26] S. K. Lynch et al. "**Interpretation of dark-field contrast and particle-size selectivity in grating interferometers**". In: *Applied Optics* 50 (2011). DOI: 10.1364/AO.50.004310.
- [27] M. Strobl. "**General solution for quantitative dark-field contrast imaging with grating interferometers**". In: *Scientific Reports* 4 (2014). DOI: 10.1038/srep07243.

- [28] H. Miao et al. "**A universal moire effect and application in X-ray phase-contrast imaging**". In: *Nature Physics* Advance online publication (2016). DOI: 10.1038/nphys3734.
- [29] H. Wen et al. "**Subnanoradian X-ray phase-contrast imaging using a far-field interferometer of nanometric phase gratings**". In: *Nature Communications* 4 (2013). DOI: 10.1038/ncomms3659.
- [30] T. Thüring et al. "**X-ray phase-contrast imaging at 100 keV on a conventional source**". In: *Scientific Reports* 4 (2014). DOI: 10.1038/srep05198.
- [31] M. Bech et al. "**In-vivo dark-field and phase-contrast x-ray imaging**". In: *Scientific Reports* 3 (2013). DOI: 10.1038/srep03209.
- [32] G. Potdevin et al. "**X-ray vector radiography for bone micro-architecture diagnostics**". In: *Physics in Medicine and Biology* 57 (2012). DOI: 10.1088/0031-9155/57/11/3451.
- [33] F. Yang et al. "**Dark-field X-ray imaging of unsaturated water transport in porous materials**". In: *Applied Physics Letters* 105, 154105 (2014). DOI: 10.1063/1.4898783.
- [34] A. Sarapata et al. "**Multi-contrast 3D X-ray imaging of porous and composite materials**". In: *Applied Physics Letters* 106 (2015). DOI: 10.1063/1.4918617.
- [35] V. Revol et al. "**Laminate fibre structure characterisation of carbon fibre-reinforced polymers by X-ray scatter dark field imaging with a grating interferometer**". In: *NDT & Evaluation International* 58 (2013). DOI: 10.1016/j.ndteint.2013.04.012.
- [36] S. R. Stock. "Characterization of Materials". In: John Wiley & Sons, Inc., 2002. Chap. X-Ray Computed Tomography. DOI: 10.1002/0471266965.com131.
- [37] J. Martín-Herrero and C. Germain. "**Microstructure reconstruction of fibrous C/C composites from X-ray microtomography**". In: *Carbon* 45 (2007). DOI: 10.1016/j.carbon.2007.01.021.
- [38] G. Requena et al. "**3D-Quantification of the distribution of continuous fibres in unidirectionally reinforced composites**". In: *Composites Part A: Applied Sciences and Manufacturing* 40 (2009). DOI: 10.1016/j.compositesa.2008.10.014.
- [39] M. Juenger, P. Monteiro, E. Gartner, and G. Denbeaux. "**A soft X-ray microscope investigation into the effects of calcium chloride on tricalcium silicate hydration**". In: *Cement and Concrete Research* 35 (2005). DOI: 10.1016/j.cemconres.2004.05.016.

- [40] E. Gartner, K. Kurtis, and P. Monteiro. "**Proposed mechanism of C-S-H growth tested by soft X-ray microscopy**". In: *Cement and Concrete Research* 30 (2000). DOI: 10.1016/s0008-8846(00)00235-0.
- [41] T. Lauridsen et al. "**Detection of sub-pixel fractures in X-ray dark-field tomography**". In: *Applied Physics A* 121 (2015). DOI: 10.1007/s00339-015-9496-2.
- [42] A. Malecki et al. "**X-ray tensor tomography**". In: *EPL (Europhysics Letters)* 105 (2014). DOI: 10.1209/0295-5075/105/38002.
- [43] J. Als-Nielsen and D. McMorrow. *Elements of Modern X-ray Physics*. John Wiley & Sons, Ltd, 2011. DOI: 10.1002/9781119998365.
- [44] P. Willmott. *An Introduction to Synchrotron Radiation*. John Wiley & Sons, Ltd, 2011. DOI: 10.1002/9781119970958.
- [45] M. Bech. "X-ray imaging with a grating interferometer". PhD thesis. University of Copenhagen, 2007.
- [46] A. H. Compton. "**Secondary Radiations produced by X-rays and some of their applications to physical problems**". In: *Bulletin of the National Research Council* 4 (1922).
- [47] J. Felber, R. Gähler, R. Golub, and K. Prechtel. "**Coherence volumes and neutron scattering**". In: *Physica B: Condensed Matter* 252 (1998). DOI: 10.1016/S0921-4526(97)00999-X.
- [48] A. S. Marathay. *Elements of optical coherence theory*. John Wiley & Sons, Ltd, 1982. ISBN: 9780471567899.
- [49] O. Hemberg, M. Otendal, and H. M. Hertz. "**Liquid-metal-jet anode electron-impact x-ray source**". In: *Applied Physics Letters* 83 (2003). DOI: <http://dx.doi.org/10.1063/1.1602157>.
- [50] O. Klein and Y. Nishina. "**Über die Streuung von Strahlung durch freie Elektronen nach der neuen relativistischen Quantendynamik von Dirac**". In: *Zeitschrift für Physik* 52 (1929). DOI: 10.1007/BF01366453.
- [51] M. Bech et al. "**X-ray imaging with the PILATUS 100k detector**". In: *Applied Radiation and Isotopes* 66 (2008). DOI: <http://dx.doi.org/10.1016/j.apradiso.2007.10.003>.
- [52] S. Deans. *The Radon Transform and Some of Its Applications*. Dover Publications, 2007. ISBN: 9780486462417.
- [53] J. Mohr et al. "**High aspect ratio gratings for X-ray phase contrast imaging**". In: *AIP Conference Proceedings* 1466 (2012). DOI: 10.1063/1.4742267.

- [54] M. Engelhardt et al. "**The fractional Talbot effect in differential x-ray phase-contrast imaging for extended and polychromatic x-ray sources**". In: *Journal of Microscopy* 232 (2008). DOI: 10.1111/j.1365-2818.2008.02072.x.
- [55] Y. Takeda et al. "**X-Ray Phase Imaging with Single Phase Grating**". In: *Japanese Journal of Applied Physics* 46 (2007). DOI: 10.1143/jjap.46.189.
- [56] A. Momose et al. "**Demonstration of X-Ray Talbot Interferometry**". In: *Japanese Journal of Applied Physics* 42 (2003). DOI: 10.1143/jjap.42.1866.
- [57] M. Bech et al. "**Quantitative x-ray dark-field computed tomography**". In: *Physics in Medicine and Biology* 55 (2010). DOI: 10.1088/0031-9155/55/18/017.
- [58] M. Baier. "Experimental Characterization and Optimization of a High-Resolution X-Ray Grating Interferometer Setup with Respect to Material Research". PhD thesis. Technical University of Munich, 2015.
- [59] M. Ruiz-Yaniz et al. "**X-ray grating interferometry at photon energies over 180 keV**". In: *Applied Physics Letters* 106 (2015). DOI: 10.1063/1.4917293.
- [60] F. Prade, A. Yaroshenko, J. Herzen, and F. Pfeiffer. "**Short-range order in mesoscale systems probed by X-ray grating interferometry**". In: *EPL* 112 (2015). DOI: 10.1209/0295-5075/112/68002.
- [61] W. Yashiro et al. "**Distribution of unresolvable anisotropic microstructures revealed in visibility-contrast images using x-ray Talbot interferometry**". In: *Physical Review B* 84 (9 2011). DOI: 10.1103/PhysRevB.84.094106.
- [62] M. Rekveldt. "**Novel SANS instrument using Neutron Spin Echo**". In: *Nuclear Instruments and Methods in Physics Research Section B: Beam Interactions with Materials and Atoms* 114 (1996). DOI: 10.1016/0168-583X(96)00213-3.
- [63] W. G. Bouwman, W. Kraan, and M. Rekveldt. "**Spin echo small angle neutron scattering experiment**". In: *Physica B: Condensed Matter* 267-268 (1999). DOI: 10.1016/S0921-4526(99)00031-9.
- [64] W. G. Bouwman and M. T. Rekveldt. "**Spin-echo small-angle neutron scattering calculations**". In: *Physica B: Condensed Matter* 276-278 (2000). DOI: 10.1016/S0921-4526(99)01252-1.
- [65] H. Friedrich. *Scattering Theory*. Springer-Verlag Berlin Heidelberg, 2013. DOI: 10.1007/978-3-642-38282-6.
- [66] D. S. Sivia. *Elementary Scattering Theory*. Oxford University Press, 2011. DOI: 10.1093/acprof:oso/9780199228676.001.0001.
- [67] R. Andersson, L. F. Van Heijkamp, I. M. De Schepper, and W. G. Bouwman. "**Analysis of spin-echo small-angle neutron scattering measurements**". In: *Journal of Applied Crystallography* 41 (2008). DOI: 10.1107/S0021889808026770.

- [68] T. Krouglov, I. M. de Schepper, W. G. Bouwman, and M. T. Rekveldt. "**Real-space interpretation of spin-echo small-angle neutron scattering**". In: *Journal of Applied Crystallography* 36 (2003). DOI: 10.1107/S0021889802020368.
- [69] R. Andersson et al. "**Structure, anisotropy and fractals in compressed cohesive powders**". In: *Powder Technology* 189 (2009). DOI: 10.1016/j.powtec.2008.05.010.
- [70] W. G. Bouwman et al. "**SESANS studies of colloid phase transitions, dairy products and polymer fibres**". In: *Physica B: Condensed Matter* 350 (2004). DOI: 10.1016/j.physb.2004.04.013.
- [71] F. Pfeiffer et al. "**Shearing Interferometer for Quantifying the Coherence of Hard X-Ray Beams**". In: *Phys. Rev. Lett.* 94 (16 2005). DOI: 10.1103/PhysRevLett.94.164801.
- [72] R. Gähler et al. "**Space-time description of neutron spin echo spectrometry**". In: *Physica B: Condensed Matter* 229 (1996). DOI: 10.1016/S0921-4526(96)00509-1.
- [73] T. Donath et al. "**Inverse geometry for grating-based x-ray phase-contrast imaging**". In: *Journal of Applied Physics* 106 (2009). DOI: 10.1063/1.3208052.
- [74] O. Uca, W. G. Bouwman, and M. T. Rekveldt. "**Model calculations for the spin-echo small-angle neutron-scattering correlation function**". In: *J. Appl. Crystallogr.* 36 (2003). DOI: 10.1107/S0021889802020356.
- [75] M. T. Rekveldt et al. "Elastic Neutron Scattering Measurements Using Larmor Precession of Polarized Neutrons". In: *Neutron Spin Echo Spectroscopy, Lecture Notes in Physics*. Ed. by F. Mezei, C. Pappas, and T. Gutberlet. Wiesbaden: Heidelberg: Springer-Verlag, 2002. DOI: 10.1007/3-540-45823-9.
- [76] T. H. Jensen et al. "**Directional x-ray dark-field imaging of strongly ordered systems**". In: *Physical Review B* 82 (21 2010). DOI: 10.1103/physrevb.82.214103.
- [77] W. G. Bouwman, T. V. Kruglov, J. Plomp, and M. T. Rekveldt. "**Spin-echo methods for SANS and neutron reflectometry**". In: *Physica B: Condensed Matter* 357 (2005). DOI: 10.1016/j.physb.2004.11.024.
- [78] F. Prade et al. "**Observing the setting and hardening of cementitious materials by X-ray dark-field radiography**". In: *Cement and Concrete Research* 74 (2015). DOI: 10.1016/j.cemconres.2015.04.003.
- [79] F. Prade et al. "**Time-resolved X-ray dark-field tomography revealing water transport in a fresh cement sample**". In: *Scientific Reports* 6 (2016). DOI: 10.1038/srep29108.

- [80] F. Yang et al. "**X-ray dark-field contrast imaging of water transport during hydration and drying of early age cement-based materials**". In: *In preparation* (2016).
- [81] S. Grumbein et al. "**Hydrophobic Properties of Biofilm-Enriched Hybrid Mortar**". In: *Advanced Materials* 28 (2016). DOI: 10.1002/adma.201602123.
- [82] P. C. Hewlett. *Lea's Chemistry of Cement and Concrete*. Elsevier Ltd., 2003. DOI: 10.1016/b978-0-7506-6256-7.x5007-3.
- [83] V. M. Malhotra and P. K. Mehta. *Pozzolanic and Cementitious Materials*. Taylor & Francis, 1996. ISBN: 9782884492355.
- [84] V. D. Z. e.V. *Zement Taschenbuch 2002*. Verlag Bau und Technik, 2002. ISBN: 9783764004279.
- [85] G. Sant, M. Dehadrai, and D. Bentz. "**Detecting the fluid-to-solid transition in cement pastes**". In: *Concrete International* 31 (2009).
- [86] H. W. Reinhardt and C. U. Grosse. "**Continuous monitoring of setting and hardening of mortar and concrete**". In: *Construction and Building Materials* 18 (2004). DOI: 10.1016/j.conbuildmat.2003.10.002.
- [87] C. U. Grosse. "Ultrasound testing for early age quality control of concrete". In: *Proceedings of the 13th International Conference on Structural Faults & Repair*. Ed. by M. Forde. Edinburgh, 2010.
- [88] N. Robeyst, C. U. Grosse, and N. De Belie. "**Measuring the change in ultrasonic p-wave energy transmitted in fresh mortar with additives to monitor the setting**". In: *Cement and Concrete Research* 39 (2009). DOI: 10.1016/j.cemconres.2009.06.016.
- [89] H. W. Reinhardt and C. U. Grosse. "Mechanical Wave Propagation - Basics". In: *Advanced testing of cement-based materials during setting and hardening. RILEM Report 31*. Ed. by H. W. Reinhardt and C. U. Grosse. RILEM Publ. S.A.R.L., 2005. DOI: 10.1617/2912143705.004.
- [90] J. L. Granja, M. Azenha, C. Sousa, and C. Ferreira. "**Comparison Between Different Experimental Techniques for Stiffness Monitoring of Cement Pastes**". In: *Journal of Advanced Concrete Technology* 12 (2014). DOI: 10.3151/jact.12.47.
- [91] P. Lura, J. Couch, O. M. Jensen, and J. Weiss. "**Early-age acoustic emission measurements in hydrating cement paste: Evidence for cavitation during solidification due to self-desiccation**". In: *Cement and Concrete Research* 39 (2009). DOI: 10.1016/j.cemconres.2009.06.015.
- [92] D. Derome, M. Griffa, M. Koebel, and J. Carmeliet. "**Hysteretic swelling of wood at cellular scale probed by phase-contrast X-ray tomography**". In: *Journal of Structural Biology* 173 (2011). DOI: 10.1016/j.jsb.2010.08.011.

- [93] W. Li, M. Pour-Ghaz, J. Castro, and J. Weiss. "**Water Absorption and Critical Degree of Saturation Relating to Freeze-Thaw Damage in Concrete Pavement Joints**". In: *Journal of Materials in Civil Engineering* 24 (2012). DOI: 10.1061/(ASCE)MT.1943-5533.0000383.
- [94] N. Tsui, R. J. Flatt, and G. W. Scherer. "**Crystallization damage by sodium sulfate**". In: *Journal of Cultural Heritage* 4 (2003). DOI: 10.1016/S1296-2074(03)00022-0.
- [95] H. Derluyn et al. "**Characterizing saline uptake and salt distributions in porous limestone with neutron radiography and X-ray micro-tomography**". In: *Journal of Building Physics* 36 (2013). DOI: 10.1177/1744259112473947.
- [96] A. Michel, P. Nygaard, and M. Geiker. "**Experimental investigation on the short-term impact of temperature and moisture on reinforcement corrosion**". In: *Corrosion Science* 72 (2013). DOI: 10.1016/j.corsci.2013.02.006.
- [97] C. Hall. "**Water sorptivity of mortars and concretes: a review**". In: *Magazine of Concrete Research* 41 (1989). DOI: 10.1680/macr.1989.41.147.51.
- [98] D. Lockington, J.-Y. Parlange, and P. Dux. "**Sorptivity and the estimation of water penetration into unsaturated concrete**". In: *Materials and Structures* 32 (1999). DOI: 10.1007/BF02479625.
- [99] T. A. Carpenter et al. "**Capillary water migration in rock: process and material properties examined by NMR imaging**". In: *Materials and Structures* 26 (1993). DOI: 10.1007/bf02472950.
- [100] H. Justnes, K. Bryhn-Ingebrigtsen, and G. O. Rosvold. "**Neutron radiography: an excellent method of measuring water penetration and moisture distribution in cementitious materials**". In: *Advances in Cement Research* 6 (1994). DOI: 10.1680/adcr.1994.6.22.67.
- [101] G. Sant, A. Eberhardt, D. Bentz, and J. Weiss. "**Influence of Shrinkage-Reducing Admixtures on Moisture Absorption in Cementitious Materials at Early Ages**". In: *Journal of Materials in Civil Engineering* 22 (2010). DOI: 10.1061/(asce)0899-1561(2010)22:3(277).
- [102] A. Pourasee, A. Peled, and J. Weiss. "**Fluid Transport in Cracked Fabric-Reinforced-Cement-Based Composites**". In: *Journal of Materials in Civil Engineering* 23 (2011). DOI: 10.1061/(asce)mt.1943-5533.0000289.
- [103] E. Franzoni et al. "**Solvent-based ethyl silicate for stone consolidation: influence of the application technique on penetration depth, efficacy and pore occlusion**". In: *Materials and Structures* 48 (2015). DOI: 10.1617/s11527-014-0417-1.

- [104] M. Göbel, L. Urbonas, H. Hilbig, and D. Heinz. "Wirkung von organischen Additiven auf die puzzolanische Aktivität von Flugaschegläsern". In: *18. Internationale Baustofftagung, ibausil*. Vol. 1. 2012.
- [105] Y. Zhu, M. Zhao, H. Li, and P. Zhang. "**Micro-CT artifacts reduction based on detector random shifting and fast data inpainting**". In: *Medical Physics* 40 (2013). DOI: 10.1118/1.4790697.
- [106] D. Cusson and T. Hoogeveen. "**Internal curing of high-performance concrete with pre-soaked fine lightweight aggregate for prevention of autogenous shrinkage cracking**". In: *Cement and Concrete Research* 38 (2008). DOI: 10.1016/j.cemconres.2008.02.001.
- [107] A. Bentur, S. Igarashi, and K. Kovler. "**Prevention of autogenous shrinkage in high-strength concrete by internal curing using wet lightweight aggregates**". In: *Cement and Concrete Research* 31 (2001). DOI: 10.1016/S0008-8846(01)00608-1.
- [108] F. Prade et al. "**Nondestructive characterization of fiber orientation in short fiber reinforced polymer composites with X-ray vector radiography**". In: *NDT & E International* 86 (2016). DOI: 10.1016/j.ndteint.2016.11.013.
- [109] S.-Y. Fu, B. Lauke, and Y.-W. Mai. "1 - Introduction to short fibre reinforced polymer composites". In: *Science and Engineering of Short Fibre Reinforced Polymer Composites*. Ed. by S.-Y. Fu, B. Lauke, and Y.-W. Mai. Woodhead Publishing, 2009. DOI: 10.1533/9781845696498.1.
- [110] B. Fisa and M. Rahmani. "**Weldline strength in injection molded glass fiber-reinforced polypropylene**". In: *Polymer Engineering & Science* 31 (1991). DOI: 10.1002/pen.760311807.
- [111] G. Mayr, B. Plank, J. Sekelja, and G. Hendorfer. "**Active thermography as a quantitative method for non-destructive evaluation of porous carbon fiber reinforced polymers**". In: *NDT & E International* 44 (2011). DOI: 10.1016/j.ndteint.2011.05.012.
- [112] G. Mook, R. Lange, and O. Koeser. "**Non-destructive characterisation of carbon-fibre-reinforced plastics by means of eddy-currents**". In: *Composites Science and Technology* 61 (2001). DOI: 10.1016/S0266-3538(00)00164-0.
- [113] E. Birt and R. Smith. "**A review of NDE methods for porosity measurement in fibre-reinforced polymer composites**". In: *Insight* 46 (2004). DOI: 10.1784/insi.46.11.681.52280.
- [114] D. Salaberger et al. "**Evaluation of computed tomography data from fibre reinforced polymers to determine fibre length distribution**". In: *International Polymer Processing* 26 (2011). DOI: 10.3139/217.2441.

- [115] V. Revol et al. "**Orientation-selective X-ray dark field imaging of ordered systems**". In: *Journal of Applied Physics* 112 (2012). DOI: 10.1063/1.4768525.
- [116] A. Malecki et al. "**Coherent Superposition in Grating-Based Directional Dark-Field Imaging**". In: *PLoS One* 8 (2013). DOI: 10.1371/journal.pone.0061268.
- [117] F. Bayer et al. "**Projection angle dependence in grating-based X-ray dark-field imaging of ordered structures.**" In: *Optics Express* 21 (2013). DOI: 10.1364/OE.21.019922.
- [118] C. Hanneschläger et al. "**Fibre structure characterisation of injection moulded short fibre-reinforced polymers by X-ray scatter dark field tomography**". In: *Case Studies in Nondestructive Testing and Evaluation* 3 (2015). DOI: 10.1016/j.csnadt.2015.04.001.
- [119] T. H. Jensen et al. "**Directional x-ray dark-field imaging.**" In: *Physics in Medicine and Biology* 55 (2010). DOI: 10.1088/0031-9155/55/12/004.
- [120] F. Schaff et al. "**Correlation of X-ray vector radiography to bone micro-architecture.**" In: *Scientific Reports* 4 (2014). DOI: 10.1038/srep03695.
- [121] C. Jud et al. "**Dentinal tubules revealed with X-ray tensor tomography**". In: *Dental Materials* 32 (2016). DOI: <http://dx.doi.org/10.1016/j.dental.2016.06.021>.
- [122] Y. Qin et al. "**Micro-manufacturing: research, technology outcomes and development issues**". In: *The International Journal of Advanced Manufacturing Technology* 47 (2010). DOI: 10.1007/s00170-009-2411-2.
- [123] N. P. Mahalik. *Micromanufacturing and Nanotechnology*. Springer-Verlag Berlin Heidelberg, 2006. DOI: 10.1007/3-540-29339-6.
- [124] I. Gibson, D. Rosen, and B. Stucker. *Additive Manufacturing Technologies*. Springer New York, 2015. DOI: 10.1007/978-1-4939-2113-3.
- [125] A. R. Razali and Y. Qin. "**A Review on Micro-manufacturing, Micro-forming and their Key Issues**". In: *Procedia Engineering* 53 (2013). DOI: 10.1016/j.proeng.2013.02.086.
- [126] J.-P. Kruth, M. Leu, and T. Nakagawa. "**Progress in Additive Manufacturing and Rapid Prototyping**". In: *CIRP Annals - Manufacturing Technology* 47 (1998). DOI: 10.1016/S0007-8506(07)63240-5.

Publications and conference contributions

First author publications (peer-reviewed)

F. Prade et al. "**Observing the setting and hardening of cementitious materials by X-ray dark-field radiography**". In: *Cement and Concrete Research* 74 (2015), pp. 19–25. DOI: 10.1016/j.cemconres.2015.04.003

F. Prade et al. "**Short-range order in mesoscale systems probed by X-ray grating interferometry**". In: *EPL* 112.6 (2015), p. 68002. DOI: 10.1209/0295-5075/112/68002

F. Prade et al. "**Time-resolved X-ray dark-field tomography revealing water transport in a fresh cement sample**". In: *Scientific Reports* 6 (2016). DOI: 10.1038/srep29108

F. Prade et al. "**Nondestructive characterization of fiber orientation in short fiber reinforced polymer composites with X-ray vector radiography**". In: *NDT & E International* 86 (2016), pp. 65–72. DOI: 10.1016/j.ndteint.2016.11.013

Co-author publications (peer-reviewed)

F. Yang et al. "**Dark-field X-ray imaging of unsaturated water transport in porous materials**". In: *Applied Physics Letters* 105.15, 154105 (2014). DOI: 10.1063/1.4898783

S. Grumbein et al. "**Hydrophobic Properties of Biofilm-Enriched Hybrid Mortar**". In: *Advanced Materials* 28.37 (2016), pp. 8138–8143. DOI: 10.1002/adma.201602123

Y. Sharma et al. "**Six dimensional X-ray Tensor Tomography with a compact laboratory setup**". In: *Applied Physics Letters* 109.13, 134102 (2016). DOI: 10.1063/1.4963649

P. Bidola et al. "**Propagation-based phase retrieval: Enabling sensitive, high-resolution imaging at a commercial lab-based X-ray micro-CT system**". In: *Revision submitted to journal* (2016)

F. Schaff et al. "**Non-iterative Directional Dark-field Tomography**". In: *Accepted to be published in Scientific Reports* (2017)

F. Yang et al. "**X-ray dark-field contrast imaging of water transport during hydration and drying of early age cement-based materials**". In: *In preparation* (2016)

T. J. Schröter et al. "**Large field-of-view tiled grating structures for X-ray phase-contrast imaging**". In: *Review of Scientific Instruments* 88.1 (2017), p. 015104. DOI: 10.1063/1.4973632

Conference contributions

Title: "**Applications of grating-based X-ray imaging in cement research**", Poster presentation at the conference for X-ray and Neutron Phase Imaging with Gratings (XN-PIG), Best Poster Award Winner, Garmisch-Partenkirchen, Germany, 2014

Title: "**Applications of grating-based X-ray imaging in materials research**", Invited oral presentation at the APS Users Meeting, Argonne, USA, 2014

Title: "**A Study on the Hydration Processes in Cementitious Material based on X-ray Dark-Field Imaging**", Oral presentation at the International Conference on Computed tomography of materials and structures (ICTMS), Quebec City, Canada, 2015

Title: "**Measuring the real space correlation with x-ray dark-field imaging**", Oral presentation at the conference for X-ray and Neutron Phase Imaging with Gratings (XNPIG), Bethesda, USA, 2015

Title: "**Revealing water transport in microporous systems with grating based X-ray dark-field tomography**", Oral presentation at the X-Ray Microscopy Conference (XRM), Oxford, UK, 2016

Acknowledgments

I am really grateful for all the time that I spent working on my PhD project in such a remarkable and cheerful group. First of all, I would therefore like to thank my scientific supervisor Franz Pfeiffer for directing my interest to X-ray physics during my master's studies and giving me the opportunity to pursue my research interests at his chair. I benefited a great deal from your experience. You were always open to my ideas and gave me the freedom and all the financial support to pursue them. I appreciate that you always trusted me with my participation in many collaborations, in managing them according to my ideas, and I surely learned a lot from that.

My gratitude goes to all my friends and colleagues from the Chair of Biomedical Physics, who made the last years so special to me and helped me during this time. I would like to thank Klaus Achterhold, Nelly de Leiris and Brunhilde Vogt for their help with administrative questions. They never got tired of answering the same questions over and over again. Martin Dierolf puts a lot of effort into maintaining the IT infrastructure of the chair, and he is always helpful when it comes to experimental questions. Especially in the beginning of my project, he certainly made life easier for me. Of course, there are more people involved when it comes to IT infrastructure, and I want to thank Andreas Fehringer and the reconstruction group for the nice and easy-to-use tools. Also in the early days of my project, Rudi from the workshop was a great help. You manufactured mechanical parts quickly and precise, and I thank you for the uncomplicated collaboration. Florian Schaff and Yash Sherma spent countless hours with me discussing the daily problems in a physicist's life. They were always willing to help, interested in new ideas and eager to improve our methods. I benefited a lot from your easygoing attitude and all the input you gave me for my work. Julia Herzen and Andre Yaroshenko put a lot of effort into proof-reading of publications or parts of this work, and I appreciate their helpful input. I share a lot of nice memories with many more friends and colleagues from the chair. We experienced hilarious and exciting moments when on travel for conferences or meetings, during our yearly gathering in Sudelfeld, during social evenings, crashing bars in Munich, but also on a daily basis in the IMETUM or at the Physics Department. Here are just some of the names that come to my mind in random order at this late hour: Pidassa, Marian, Michael, Mark, Johannes, Markus B., Markus S., Zeeshan, Christoph, Konstantin, Regine, Lorenz, Benedikt, Simone. The nice and easy atmosphere cannot be taken for granted, and I always enjoyed being part of this remarkable group.

I worked closely with Prof. Christian Grosse and Prof. Detlef Heinz from the Centre for Building Materials of the Technical University of Munich. I would like to thank especially Fabian Malm and Kai Fischer for helping me understand our results from an engineering point of view. Our collaboration helped me a lot to proceed with my project and to accomplish my goals. It also resulted in a nice collaboration with Prof. Oliver Lieleg's group working on similar topics. I would like to thank Marwa Tallawi and Stefan Grumbein for their persistent interest in our experimental methods.

I went on a lot of trips to attend the meetings of the Virtual Institute for New X-ray analytic methods in material science. The presentations on different topics were always interesting, and the discussions were very helpful for my work. I like to acknowledge especially Jürgen Mohr, Pascal Meyer and all the other colleagues and PhD students from the Institute of Microstructure Technology of the Karlsruhe Institute of Technology as well as Joachim Schulz from microworks GmbH. They provide us with the best and newest grating technology, and I really appreciated the social evenings after our frequent meetings, the yearly PhD meetings and the conferences where we frequently met.

During my PhD, I worked in a very nice and productive collaboration with Fei Yang, Michele Griffa and Rolf Kaufmann from the X-ray center and the Concrete/Construction Chemistry Laboratory of EMPA, Switzerland. I enjoyed all the visits for measurements, the many hours I spent with Fei in the lab, and of course not to mention the ration of Swiss chocolate that Fei always carried in heaps in her baggage. I am really grateful for this collaboration and happy about the interesting results we achieved.

I further like to thank Prof. Johann Kastner, Sascha Senck and all the colleagues from the Computed Tomography research group of the Upper University of Austria in Wels. Our collaboration was very effective and we obtained some nice results. I also enjoyed the Conference on Industrial Computed Tomography 2016 in Wels, Austria, which was organized very nicely by Prof. Kastner and his group.

Özgür Inan, Richard and Thomas, I draw a lot of strength from our loyal friendship, and I am grateful to have you by my side at all times.

Ingrid, Regina and Klaus, your limitless support and guidance in every aspect of my life always encouraged me, kept me motivated, and it will continue to do so.